4D Microstructural Characterization of Electromigration and Thermal Aging Damage in Tin-Rich Solder Joints

by

Marion Branch Kelly

A Dissertation Presented in Partial Fulfilment
of the Requirements for the Degree
Doctor of Philosophy

Approved July 2019 by the
Graduate Supervisory Committee:

Nikhilesh Chawla, Chair
Kumar Ankit
Aravindha Antoniswamy

ARIZONA STATE UNIVERSITY
August 2019

ABSTRACT

As the microelectronics industry continues to decrease the size of solder joints, each joint will have to carry a greater current density, making atom diffusion due to current flow, electromigration (EM), a problem of ever-increasing severity. The rate of EM damage depends on current density, operating temperature, and the original microstructure of the solder joint, including void volume, grain orientation, and grain size. While numerous studies have investigated the post-mortem effects of EM and have tested a range of current densities and temperatures, none have been able to analyze how the same joint evolves from its initial to final microstructure. This thesis focuses on the study of EM, thermal aging, and thermal cycling in Sn-rich solder joints. Solder joints were either of controlled microstructure and orientation or had trace alloying element additions. Sn grain orientation has been linked to a solder joints' susceptibility to EM damage, but the precise relationship between orientation and intermetallic (IMC) and void growth has not been deduced. In this research x-ray microtomography was used to nondestructively scan samples and generate 3D reconstructions of both surface and internal features such as interfaces, IMC particles, and voids within a solder joint. Combined with controlled fabrication techniques to create comparable samples and electron backscatter diffraction (EBSD) and energy-dispersive spectroscopy (EDS) analysis for grain orientation and composition analysis, this work shows how grain structure plays a critical role in EM damage and how it differs from damage accrued from thermal effects that occur simultaneously. Unique IMC growth and voiding behaviors are characterized and explained in relation to the solder microstructures that cause their

formation and the possible IMC-suppression effects of trace alloying element addition are discussed.

DEDICATION

To my mom, Ana Maria Kelly, who believed in me first.

ACKNOWLEDGEMENTS

I would like to thank my advisor, Dr. Nikhilesh Chawla, for his support and guidance over the course of my time at Arizona State University. His drive to strive for excellence pushed me to think harder and deeper about the fundamentals of materials science, first as an undergraduate student and then as a graduate student. I would also like to thank my committee members, Dr. Kumar Ankit and Dr. Aravindha Antoniswamy, for their time and consideration. I gratefully acknowledge the use of the facilities within the Leroy Eyring Center for Solid State Science and Center for 4D Materials Science at Arizona State University. I would like to acknowledge support from the National Science Foundation (NSF) under contract number CMMI-1763128 (Alexis Lewis, Program Manager), from the Fulton Schools of Engineering at Arizona State University for a Dean's Graduate Fellowship, the Graduate College at Arizona State University for a Graduate Completion Fellowship, and the ARCS foundation for an ARCS Scholar Award.

Finally, I would like to thank Dr. Jason Williams and all the members of the Chawla Research Group, past and present, for their help and encouragement. I would like to extend my deepest gratitude to my family for their love and sacrifice and to my boyfriend for his constant support. I stand on the shoulders of giants in more ways than one.

TABLE OF CONTENTS

Page

LIST OF TABLES ... viii

LIST OF FIGURES ... ix

CHAPTER

1 INTRODUCTION ... 1

2 BACKGROUND LITERATURE ... 6

2.1 EM in Solders ... 6

2.2 Rate of EM ... 7

2.3 Effect of Specific Parameters on EM ... 9

2.3.1 Current Density ... 9

2.3.2. Temperature ... 9

2.3.3. Activation Energy for Diffusion ... 12

2.4 Effect of Diffusion Type ... 14

2.4.1 Sn Self Diffusion ... 14

2.4.2. Cu Diffusion in Sn ... 15

2.4.3. Grain Boundary Diffusion ... 24

2.5 Grain Orientation Effects ... 26

3 GRAIN ORIENTATION-ACCELERATED INTERMETALLIC GROWTH IN SINGLE AND BI-CRYSTAL SN SOLDER JOINTS, INVESTIGATED BY EBSD AND X-RAY MICROTOMOGRAPHY ... 32

3.1 Introduction ... 32

3.2 Materials and Experimental Procedure ... 34

CHAPTER Page

3.3 Results and Discussion 38

3.3.1 Surface and Grain Orientation Evolution 38

3.3.2 IMC Growth 44

3.3.3 IMC Characterization 48

3.3.3.1 Morphology and Growth 48

3.3.3.2 Relationship to Sn Matrix Recrystallization 52

3.4 Summary 57

4 ORIENTATION-DRIVEN VOID EVOLUTION DURING ELECTROMIGRATION, INVESTIGATED BY X-RAY MICROTOMOGRAPHY 59

4.1 Introduction 59

4.2 Materials and Experimental Procedure 60

4.3 Results and Discussion 61

4.3.1 Void Faceting 61

4.3.2 Void Burrowing 65

4.4 Summary 67

5. 3D EVOLUTION OF INTERMETALLIC AND VOID STRUCTURE UNDER INTERRUPTED ELECTROMIGRATION IN BI-CRYSTAL PURE SN SOLDER JOINT 70

5.1 Introduction 70

5.2 Materials and Experimental Procedure 73

5.3 Results and Discussion 76

CHAPTER Page

5.3.1 Surface Deformation ... 76

5.3.2 IMC Growth along High Angle and Twin Grain Boundaries ... 81

5.3.3 Void Evolution ... 89

5.4 Summary ... 93

6. THERMAL AGING AND ELECTROMIGRATION EFFECTS IN INDIUM-CONTAINING SN-RICH SOLDERS ... 97

6.1 Introduction ... 97

6.2 Materials and Experimental Procedure ... 99

6.3 Results and Discussion ... 100

6.4. Summary ... 113

7. CONCLUSIONS ... 115

7.1 Summary of Research Findings ... 115

7.2 Future Work ... 118

REFERENCES ... 120

LIST OF TABLES

Table Page

1. Diffusion-Related values for Sn, Cu, and Grain Boundary Diffusion for the Purpose of Determining which Types of Diffusion will Dominate at Specific Temperatures and Sample Morphologies. [1](Singh & Ohring 1984), [2](Meakin & Klokholm 1960), [3](Dyson, Anthony & Turnbull 1967) 12
2. Angles Between the c-axis and Electron Flow Direction for Samples to be used in Testing 37

LIST OF FIGURES

Figure Page

1. Schematic Diagram showing Momentum Transfer from Electrons to Sn and Cu Atoms, Creating an Atom Flux in One Direction and a Vacancy Flux in the Other, and the Electrostatic Force that Opposes the Electron Flow, adapted from (Chen & Liang 2007) 6
2. Temperature Gradient Resulting from an EM Simulation in 120 µm Sn-3.5Ag Solder Ball using 0.6 Amps (Chen & Liang 2007) 10
3. Increasing Temperature with Growing Void due to EM. (a) Ratio of Joint Resistance Change as a Function of Void Growth and (b) Increase in Temperature due to Increase in the Ratio of Joint Resistance Change (Yeh, Choi & Tu 2002) 10
4. Body-Centered Tetragonal Beta-Sn Unit Cell and Atomic Bonds shown in Tilted View, along the a-axis, and along the c-axis 13
5. SEM Images of Cross-Sectioned Sn-0.7Cu Solder Joints in the (a) Unstressed Condition and (b) After Current Stressing of 1.0×10^4 A/cm^2 at 180°C for 325 hours. A Void has Propagated Across the Solder-Cu Interface in (b), a Hallmark of Sn Diffusion (Ke et al. 2011) 15
6. Cu-Sn Phase Diagram (reproduced from NIST Material Measurement, Phase Diagrams and Computational Thermodynamics database, accessed at https://www.metallurgy.nist.gov/phase/solder/cusn.html) 18
7. (a) Schematic of Interstitial Diffusion Pathways (pink balls) in the β-Sn Lattice (cyan and green balls) along the c-axis and axis. (b and c) Diffusion Activation Energy Curves for Interstitial Diffusion along the c-axis and a-axis. Points

Figure Page

Marked M Represent Interstitial Sites at (x/4, y/4, and z/8) and Ts Represents a Transitional Site between Interstitial Sites (Liu et al. 2016) 20

8. SEM Images of Cross-Sectioned Sn-0.7Cu Solder Joints in the (a) Unstressed Condition and (b) After Current Stressing of 4.5×10^4 A/cm^2 at 60°C for 1630 hours. Large Amounts of IMC Compound have Formed and the Cu Trace at the Anode has been Degraded (Ke et al. 2011)...22

9. SEM Images of Cross-Sectioned SnAgCu Solder Joints after Tensile Testing and (a) no EM, (b) 3.3×10^3 A/cm^2 at 100°C and (c) 5.0×10^3 A/cm^2 at 100°C. Variation in EM Testing Resulted a Transition from Ductile to Brittle Fracture (Ren et al. 2006) 23

10. Effective Diffusivity of 95.5Sn-4.0Ag-0.5Cu, due to Vacancy Diffusion along Grain Boundaries, as a Function of Temperature at Varying Grain Sizes. Data Derived from a Monte Carlo Simulation-Based Algorithm. Diffusivity Decreases with Increasing Grain Size due to Decreasing Grain Boundary Area (Li & Basaran 2009)...25

11. Eight Sandwich Solder Joint Structures after Undergoing Current Stressing of 1.5×10^4 A/cm^2 at 90°C for 250 hours. The Top Set are SEM Images of Joints after EM and the Bottom Set are Sn Inverse Pole Figure Orientation Maps of the Same Joints (Chen et al. 2013)..27

12. Single and Bicrystal Solder Bar Fabrication Procedure (a), Expected Samples (b), and Preliminary EBSD for Sample Selection (c) 35

Figure Page

13. OIM Maps of Samples Selected for Testing. The Slower and Faster Diffusion Samples are Composed of a Single Grain with a Predominant Single Orientation, while the Bicrystal Samples Contain Two Grains with Different Orientations 36

14. SEM Images of Solder Bar Samples before and after EM Testing (a-f) and Thermal Aging (g-l): Pre-EM (a-c), Post-EM (d-f), Pre-aging (g-i), Post-aging (h-l). Slower Diffusion Samples (left column), Faster Diffusion Samples (center column) and Bicrystal Samples (right column) are shown. The Dashed White Arrow shows the Electron Flow Direction 39

15. SEM Images of Solder Joint Surfaces before (a) and after EM testing (b, c, d). Variations in IMC Growth between the Slower Diffusion Sample (b), Faster Diffusion Sample (c), and the Bicrystal Sample (d) Cause a Variety of Surface Deformations, in Particular the Growth of Hexagonal Cu_6Sn_5 IMC Needles (indicated with white arrows) Visible on the Surface of (d) 40

16. SEM Images and OIM Maps of Pre- and Post-Thermal Aging Samples showing the Change in Grain Structure after Aging: (a, b, c) Pre-Aging OIM Maps, (d, e, f) SEM Images of Repolished Sample Surfaces after Aging, (g, h, i) Post-Aging OIM Maps 41

17. SEM Images and OIM Maps of Pre- and Post-EM Tested Samples showing the Change in Grain Structure after Testing: (a, b, c) Pre-EM OIM Maps, (d, e, f) SEM Images of Repolished Sample Surfaces after Testing, (g, h, i) Post-EM OIM Maps 42

Figure Page

18. IMC Volume after EM for: (a) Slower Diffusion Sample, (b) Faster Diffusion Sample, and (c) Bicrystal Sample 45

19. IMC Growth Rates for Each Sample, showing Drastically Rapid IMC Growth in the Faster Diffusion Sample 46

20. IMC Volumes from Sample Centers after Thermal Aging for: (a) Slower Diffusion Sample, (b) Faster Diffusion Sample, and (c) Bicrystal Sample. Two Distinct IMC Distributions Visible in the Bicrystal Sample, (d) Elongated Particles with Vertical Alignment in the Slower Diffusion Grain and (e) Rounded Particles that Coarsened along the Horizontal Grain Boundary. Cu Diffusion Directions are shown by Red Arrows 47

21. Difference Cu_6Sn_5 IMC Growth in the Faster Diffusion Sample (a) and Bicrystal Sample (b) shown both by EBSD Maps, IPF's, and Plotting the Angle between the Basal Plane and the Cu Interface (c) 51

22. IMC PSN Recrystallization in the Slower Diffusion Sample (a,b) and Bicrystal Sample (d,e) with Recrystallization Schematic shown in (c). Magnified Regions (b) of the Post-EM EBSD Map (a) show Recrystallized Sn Grains (numbered 1-5) and Cu_6Sn_5 IMC Particles (outlined in black) along Subgrain Boundaries (lined in blue). The Orientation of the IMC Particles is shown using the Hexagonal Lattice Insets. Late-Stage Recrystallization of the Bicrystal Sample is shown in (d), where the EBSD Map is Recolored to show Maximum Feret Diameter, Smallest Grains in Blue, Largest in Red, and Grain Boundaries in White 54

Figure Page

23. Histograms showing Deviation of Sphericity in Anode and Cathode Voids before and after EM Testing. Deviation from Sphericity is Determined by the Following: $\Psi_{perfect\ sphere} - \Psi_{void}$. Reconstructions of a Representative Void before and after Testing are shown in the Insets. Void Faceting is Evident in the Slower Diffusion Sample and Cathode of the Bicrystal Sample, while Voids Remain Spherical in the Faster Diffusion Sample and Anode of the Bicrystal Sample 64

24. Void Burrowing shown by Void Reconstructions of the Faster Diffusion Sample before and after EM Testing (a and b), SEM Image of Polished Sample Cross-Section showing Burrowed Void (c), and Dimpled Bicrystal Anode Voids showing Rapid Cu Dissolution around Void Edge and Cu Peak beneath the Voids (d and e) 67

25. (a) Sample Fabrication Process from Solder Stack to Individual Solder Bars. (b) OIM Map of the Selected Bicrystal Sample. The Sample is Composed of a Fast Diffusion Grain (θ angle = 46°) and a Slow Diffusion Grain (θ angle = 71°) with a High Angle Grain Boundary between Them (dashed black line). (c) OIM Map Recolored to show the Angle between the c-axis and Electron flow (θ angle). Green and Yellow Indicate Small θ Angles and Fast Diffusion and Red and Orange Indicate Larger θ Angles and Slower Diffusion. The Slanted Orange Subgrains are Twins 75

26. SEM Images of Sample Surface at 0, 12, 25, 50, 75, and 100 hours of EM Testing. Compression from Thermal Expansion Caused the Sample to Bulge and Slant to the Right 77

Figure Page

27. (a) SEM Images of the Horizontal Grain Boundary between the Fast and Slow Diffusion Grains. (b) Higher Resolution SEM Images of a Section of the Grain Boundary, Indicated by the Yellow Box in (a), showing Grain Boundary Sliding, Surface Ledge Formation (white arrows), and Surface Evidence of IMC Particle Growth (black solid and dashed lines). (c) Evidence of Fatigue Crack (black arrow) Growth along Grain Boundary with the Slow Diffusion Sn Lattice shown in Green and the Fast Diffusion Sn Lattice shown in Pink 80

28. SEM Images of a Section of the Sn Solder/Cu Electron-Inflow Interface showing Irregular Consumption of the Cu Substrate and Solder Surface Bulging Over the Course of 100 hours of EM Testing 81

29. (a) X-Ray Microtomography Surface Reconstructions of Sample at 0, 12, 25, 50, 75, and 100-hour Timesteps, with Sn Solder in Transparent Green, Voids in Blue, and IMC in Pink. (b) Surface Reconstructions of IMC Not Associated with the Horizontal Boundary, showing Primary Formation of IMC along Slanted Twin Boundaries (pink), Followed by Secondary IMC Growth (purple) and Reduction of the Primary IMC. (c) IMC from (b) Viewed at a Diagonal Angle to show the Difference in Alignment between the Primary and Secondary IMC Growth 85

30. (left) Cu_6Sn_5 IMC Growth Over 100 hours of EM Testing, with Total IMC Growth in Green, IMC Associated with Horizontal Grain Boundary in Blue, and Twin/Bulk IMC in Red. The Majority of IMC Growth Occurred in the Twin/Bulk Region of the Sample. (right) Separation of Twin/Bulk IMC Growth into Primary and Secondary IMC Types, shown in Inset... 86

Figure Page

31. (a) Surface Reconstructions of 0-hour and 100-hour Timesteps with Sn (transparent green), Voids (blue) and IMC (pink and purple). Grey Rectangle on 100-hour Reconstruction shows the Location of Post-Testing Polished Sample Surface. (b) SEM Images of Sample at (left) 0 hours and (right) after 100 hours of Testing. 100-hour Sample was Repolished to show Internal Structure. (c) OIM Maps of Surfaces shown in (b) with {101) Twin Grain Boundaries (misorientation of 62.8° about a common <100] axis) Marked in Black and β-Sn Tetragonal Crystal Lattices of Major Orientations Overlaid. The 0-hour Map shows Twins Extending into Sample Depth while the 100-hour Map shows a Second Set of {101) Twin Grain Boundaries on a Different Orientation. (d) Inverse Pole Figures (IPFs) of OIM Maps in (c)... 88

32. (a) Surface Reconstructions of Voids at 0, 12, 25, 50, 75, and 100-hour Timesteps. (b) Void Growth and Void Number Change for Voids along the Electron-Outflow Interface, Excluding the Largest Void. (c) Void Growth and Void Number Change for Voids along the Electron-Inflow Interface. (d) Surface Reconstructions of the Largest Void at the Interface, showing Compression in the Vertical Dimension Over Time 92

33. Schematic Representation of Void Splitting Over Time as a Result of Uneven Consumption of the Electron Outflow Cu Interface and Solder Compression due to Thermal Expansion of Cu Substrate Bars. Electron Flow is Indicated with a Dashed Arrow and Thermal Compression along the Length of the Solder Joint is Indicated with Solid Black Arrows 93

Figure Page

34. Reflow Profile for SnCu and SnCuIn Solder Joint Pairs 99

35. SEM Images of SnCu Solder Joint Cross Sections, Polished after Testing 102

36. SEM Images of SnCuIn Solder Joint Cross Sections, Polished after Testing 103

37. Higher Magnification SEM Images of the 200-hour EM-Tested SnCuIn and SnCu Solder Joint Interfaces, with Phases and Current Flow Direction Marked 104

38. Electron-Inflow Interfacial IMC Growth Trends for Total IMC Thickness (solid lines), Cu_3Sn Thickness (large dashed lines), and Cu_6Sn_5 IMC Thickness (fine dashed lines). SnCu IMC Growth is in Light Green and SnCuIn IMC Growth is in Dark Green 105

39. Electron-Outflow Interfacial IMC Growth Trends for Total IMC Thickness (solid lines), Cu_3Sn IMC Thickness (large dashed lines), and Cu_6Sn_5 IMC Thickness (fine dashed lines). SnCu IMC Growth is in Light Green and SnCuIn IMC Growth is in Dark Green 106

40. (a) WDS Elemental Maps for Cu, Sn, and In, showing In Concentration in One Region in Sn Matrix. (b) SEM Image of 200-hour EM-Tested SnCuIn Sample with In-Containing Region Marked in Yellow. Area for TEM Lamella Extraction is Boxed in Red and Indicated 108

41. In-Containing Cluster Location within the SnCuIn Solder Joints, showing Cluster Concentration at the Electron Outflow Interface with Increasing EM-Testing Time 109

Figure Page

42. (a) SEM Image of TEM Lamella at Intermediate Thinning Stage, with a Hole that has formed along the Grain Boundary. (b) TEM Image of Lamella, with Grain Boundary Marked. (c-e) TEM Images of Large Spherical Particle in the Sn Matrix 111

43. (a) TEM Image of Spherical Particle in the Sn Matrix. (b-c) Higher Resolution TEM Images of Regions Indicated in (a). (d-e) FFT Analysis of Marked Regions the Particle to be Cu_7In_3 and the Matrix to be Pure Sn 112

44. (a) TEM Image of Spherical Cu_7In_3 Particle in the Sn Matrix, with Particle Boundary Indicated. (b) FFT's Taken along the Red Line Indicated in (a), Progressing from 1, Inside the Particle to 8, in the Sn Matrix. FTT's show Coherency between the (-122) Plane of Cu_7In_3 and the (001) Plane of Sn 112

CHAPTER 1

INTRODUCTION

Solder joints are present in all forms of electronics as the metal connections that allow for current flow through devices. As the microelectronics industry continues to decrease the size of solder joints, each joint will have to carry a greater current density, making atom diffusion due to current flow, electromigration (EM), a problem of ever-increasing severity (Chen & Liang 2007; Chen et al. 2012). EM has been identified as one of the most critical reliability problems in the microelectronics industry (Chen & Liang 2007; Tu 2003). Damage due to EM is twofold. Interstitial diffusion of Cu through Sn grains and along grain boundaries reacts with Sn to form the IMC compounds (IMCs) Cu_6Sn_5 and Cu_3Sn. Current flow drives Cu and Sn atoms away from the electron-inflow interface, creating a vacancy flux that results in the nucleation and growth of interfacial voids (Tu 2003; Chen & Liang 2007; Dyson, Anthony & Turnbull 1967; Lehman et al. 2010). EM is atomic diffusion driven by current flow and is therefore strongly affected by current density. As solder joints continue to decrease in size due to device miniaturization, each joint will be subject to increasing current densities and therefore experience rapid EM damage (Chen & Liang 2007; Tu 2003). In addition, joints with smaller volumes and pad-contact areas will form strength limiting flaws, such as a high density of IMCs or interfacial voids that cause open circuit failure, faster.

The Restriction of Hazardous Substances (RoHS) Directive issued by the European Union in 2006 curtailed the use of lead in many consumer electronics, driving the microelectronics industry to adopt lead-free solder alternatives which are often Sn-rich. EM is of particular concern in Sn-rich solders due the anisotropic diffusion

properties of the tetragonal β-Sn lattice. First described by Dyson and Turnbull in 1967, the interstitial diffusion of Cu along the c-axis of a Sn grain was found to be 500 times faster than diffusion along a- or b-axes at room temperature (Dyson, Anthony & Turnbull 1967). Subsequent researchers showed that Sn also exhibits anisotropic elastic modulus, thermal expansion, and resistivity (Khosa & Huntington 1975; Telang et al. 2003; Telang et al. 2002). Solder joints do not have controlled grain structures and have been shown to solidify in single crystals, six grained "beachball" type structures, fine-grained interlaced twin structures, and randomly oriented polycrystals (Lehman et al. 2010). This means that an individual joints' susceptibility to EM can vary dramatically due to differences in grain structure and prediction of joint lifetime becomes very difficult (Chen et al. 2013; Wilde 2014; Kerr & Chawla 2004). In order to study precisely how EM drives IMC and void formation, researchers have focused on the fastest diffusion pathways for Cu and Sn atoms: the c-axis of the Sn grains and grain boundaries (Tu 2003; Chen & Liang 2007; Dyson, Anthony & Turnbull 1967; Lehman et al. 2010).

Numerous studies have investigated the effect of grain orientation on EM lifetimes in various solder geometries and found that grains with the c-axis of the Sn grains aligned with the electron flow experience rapid IMC growth, while those with the c-axis perpendicular to the electron flow experienced void formation at the electron inflow interface (Lu et al. 2008; Chen et al. 2013; Tasooji, Lara & Lee 2014; Huang et al. 2015; Huang et al. 2016; Shen & Chen 2017; Tian et al. 2018). A parameter was created to quantify the degree of alignment between the c-axis and the electron flow, termed the θ angle (or α angle, less commonly) and represented the angle between the c-axis and the electron flow direction. In general, solder joints containing Sn grains with small θ angles

will experience severe EM damage while those containing large θ angles will experience little (Chen et al. 2015; Chen et al. 2013; Lu et al. 2008; Chen, Guo, et al 2015). There is additional interest in the effect of grain boundaries on EM damage. Grain boundary diffusion relies on the energy of the boundary and hence its atomic ordering. High angle grain boundaries have low order and support fast diffusion, while low angle and twin boundaries are highly ordered and support little to no diffusion (Wilde 2014). As such the Cu-driven IMC should vary with grain boundary character. IMC particles have been shown to form along high angle grain boundaries (Kerr & Chawla 2004; Deng et al. 2005; Jiang & Chawla 2010; Shen & Chen 2017; Ma et al. 2018; Maruyama 1960) with less attention given to low angle and twin boundaries, although they could present significant barriers to diffusion. Grain orientation can also affect surface deformation as IMC particles coarsening in the bulk of the solder joint can often be seen protruding from the sample surface in hillocks or mounds (Chen et al. 2013; Tian et al. 2018).

In addition to current-driven diffusion, EM is also inextricably linked with thermal effects. Current flow through more conductor will experience some measure of resistance, which causes resistive or Joule heating. This means that thermal effects like thermal expansion and thermal diffusion are always present in EM tests. The temperature of an EM test can be stabilized by providing a heat-sink environment like an oil bath or by raising the background temperature slightly above that typically experienced by the test set up. Current flow through an experimental set up or sample will also experience current crowding effects due to the various cross-sectional areas of conductive material through which the current will pass. Typically solder joints consist of a solder ball reflowed on a thin layer of Cu attached to a printed circuit board (PCB). The Cu layer is

called a pad and can be coated with one or a combination of metallization layers composed of a variety of materials including but not limited to Au, Al, Ni, and Ti. The metallization layers can serve as diffusion barriers to Cu diffusion. The solder ball may be connected on the opposite side by another Cu or Al pad. The solder joints used in this research do not have metallization layers, instead the solder is in direct contact with the Cu substrate and therefore will experience more rapid Cu diffusion than a joint with metallization. A critical issue is that the cross-sectional area of the metallization pads is very small compared to that of the solder ball, meaning a ball experiences significant current crowding where the ball meets the pad. Current crowding causes Joule heating and accelerated atomic diffusion, often causing voids to nucleate at the current crowded region (Zhang et al. 2006; Han et al. 2012). Distinguishing between current crowding effects and grain orientation effects on void formation is often difficult.

The wealth of research into EM and the parameters that affect it is extensive, however an in-depth study correlating solder structure to both IMC and void growth and morphology in a controlled manner is required. Studies have used solder joints in a host of geometries and orientations, averaging grain orientation and grain boundary effects with those induced by current flow or temperature. The aim of this work is to study the effects of grain structure on EM in a controlled, repeatable manner. Precise sample fabrication techniques created single and bicrystal samples so that the effects of a specific orientation could be isolated and compared to others. Samples were symmetrical and continuous in cross-section to avoid current crowding effects. Materials are characterized in 3D using x-ray microtomography, allowing for a comprehensive understanding of the initial structure of the sample, before it undergoes testing, so that any changes developed

during EM can be linked to a microstructural feature. Electron backscatter diffraction (EBDS), energy-dispersive spectroscopy (EDS), and scanning electron microscope (SEM) analysis were done to determine grain structure and composition. Cu_6Sn_5 IMC growth and morphology were linked with grain orientation and grain boundary structure, with implications for future solder joint reliability. Unusual void behaviors were discovered and connected to orientation effects. X-ray microtomography scans captured the evolution of IMC and void structures over time, showing how they relate to existing structures and informing on how structures seen post-testing evolved. An investigation into the effects of a trace addition of In on EM behavior of a SnCu solder demonstrates the potential benefits of alloying elements for reducing EM damage.

It was the goal of this research to further the understanding of EM damage in solder joints to better designs for EM-prevention in future electronic devices.

CHAPTER 2

LITERATURE REVIEW

2.1 EM in Sn Solder Joints

EM is a mass transport phenomenon that causes damage in current carrying components, leading to the decreased lifetime and open circuit failure of electronic systems (Chen & Liang 2007; Chen et al. 2012). Solder joints are metal connections that conduct electricity between layers of circuitry and are commonly affected by EM. Solder joints typically range in size from 50 μm to 500 μm. They can be formed by screen printing or depositing solder paste or by placing solder spheres on a substrate coated with flux. As microelectronics continue to shrink, solder joints will decrease in size and become increasingly susceptible to EM damage due to the higher current densities the joints will have to carry (Chen & Liang 2007; Chen et al. 2012).

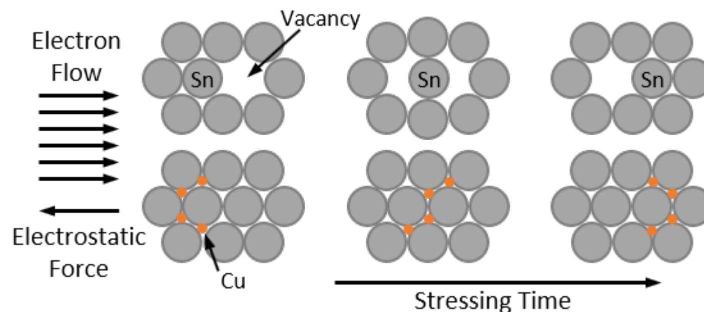

Figure 1. Schematic diagram showing momentum transfer from electrons to Sn and Cu atoms, creating an atom flux in one direction and a vacancy flux in the other, and the electrostatic force that opposes the electron flow, adapted from (Chen & Liang 2007).

The phenomenon of EM is driven by the presence of an electric field and moving charge carriers (Chen & Liang 2007). As electrons flow through the interconnects, they scatter inelastically with metal atoms and transfer momentum to them. This momentum transfer contributes to the atoms' overall energy, increasing its likelihood of overcoming the activation energy for diffusion, and is termed the "electron wind" force. The electric field produced by the moving atoms would cause positive metal ions to diffuse opposite to the current flow, but the electric field force is overcome by the electron wind.

In the case of self-diffusion, the atom will jump into a neighboring vacancy and in interstitial diffusion, the atom will jump into the closest empty interstitial site. The type of diffusion that occurs will determine the type of damage the joint will undergo. Self-diffusion of aluminum due to EM is illustrated in Figure 1 (Chen & Liang 2007). Over time, EM will create an atom flux along the direction of current flow and a vacancy flux in the opposing direction. The vacancy flux leads to the formation of voids at the anode and the atom flux accelerates build up of IMC layers and under bump metallization consumption at the cathode (Ke et al. 2011).

2.2 Rate of EM

Since EM is essentially diffusion enhanced by current flow, it is possible to combine a convential equation for diffusion with current flow considerations in order to estimate how rapidly EM damage will occur. This combination results in an atom flux equation of the form in Equation 1:

$$J = CeZ^{*}\rho j \left(\frac{D}{kT}\right) \qquad (1)$$

where C is the concentration of metal ions, eZ^* is the effective charge of the ions, ρ is the metal resistivity, j is the electrical current density, D is the diffusivity of the atom, k is Boltzmann's constant, and T is the absolute temperature (Ke et al. 2011). While this form of equation is sufficient to describe how EM will affect a solder joint, a more informative form of the equation is shown in Equation 2, that shows the average drift velocity of an atom, v (Huntington & Grone 1961). By dividing the flux equation by the concentration of metal ions and breaking up the diffusivity term, the parameters that affect EM are clearly shown.

$$v = \frac{J}{C} = BeZ^*\rho j = \left(\frac{D_0}{kT}\right) eZ^*\rho j e^{\left(-\frac{E_a}{kT}\right)} \qquad (2)$$

All constants are the same as described in Equation 1 with the addition of the activation energy of diffusion, E_a, and the prefactor for the diffusion constant, D_0.

By inspection of the above equation, three parameters lend themselves to investigation: current density, joint temperature, and activation energy. Current density refers to the number of electrons flowing through a particular cross-sectional area of the solder joint. Since electron-atom collisions are what provide the force that causes atoms to diffuse, an increase in current density would strongly affect the rate of EM. Temperature would not play a large role if it were assumed constant. However, large temperature gradients have been shown across solder joints, and therefore local temperatures must be taken into account (Chen & Liang 2007; Yamanaka & Ooyoshi 2010; Yang, Chen & Wu 2007). The activation energy for diffusion is of interest because it is the distinguishing feature between the various types of diffusion occurring during

EM. Sn self-diffusion, Cu interstitial diffusion, and grain boundary diffusion all play a role in the microstructural changes seen in solder joints after current stressing.

2.3 Effect of Specific Parameters on EM

2.3.1 Current Density

The threshold current density for inducing significant EM is commonly held to be around 1×10^4 A/cm^2, as this is where many papers have seen damage (Chen & Liang 2007; Chen et al. 2012; Tu 2003; Ren et al. 2006). Since current density depends on cross-sectional area, shrinking the dimensions of traces and solder balls is going to rapidly increase the importance of the current density. This is illustrated neatly by imaging two solder joints, one 500 μm in diameter and the other 50 μm. Both joints are subjected to current stressing of 0.2 Amps, the expected current a joint should be able to carry under the design rule of packaging in 2003 (Tu 2003). The 500 μm joint will experience a current density of 10^2A/cm^2 whereas the 50 μm joint would experience 10^4A/cm^2. Dropping the joint size to 1 μm, as is predicted for future integrated circuit designs, would increase the current density to 2.5×10^7 A/cm^2, resulting in a drift velocity increase of five orders of magnitude, other factors held constant (Chen & Liang 2007).

2.3.2. Temperature

The consideration of temperature follows from current density, as current crowding causes regions of local heating (Yeh, Choi & Tu 2002). Increasing current density increases the number of electron-atom collisions and scattering events. These collisions randomize the motion of particles, which generates thermal energy, increasing temperature. Random particle motion also corresponds to an increase in resistivity, which

also increases temperature. Figure 2 shows the temperature gradient formed due to the simulation of 0.6 Amp current stressing. As expected, the hot spot in the top left corner corresponds to the current crowded region. The temperature gradient across the joint is approximately 642°C/cm, significant enough to cause thermomigration which is atom diffusion due to a temperature gradient and can be investigated separately from EM.

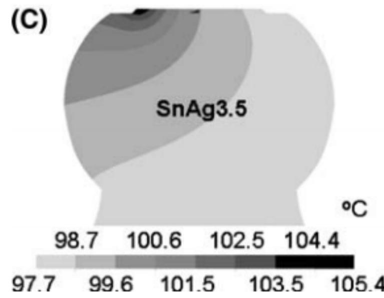

Figure 2. Temperature gradient resulting from an EM simulation in 120 μm Sn-3.5Ag solder ball using 0.6 Amps (Chen & Liang 2007)

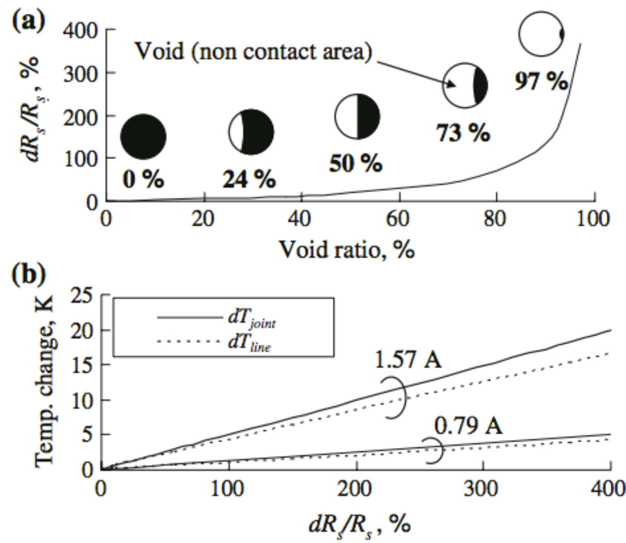

Figure 3. Increasing temperature with growing void due to EM. (a) Ratio of joint resistance change as a function of void growth and (b) increase in temperature due to increase in the ratio of joint resistance change (Yeh, Choi & Tu 2002).

Since the temperature increase is driven by current crowding, which results in void growth, temperature, resistivity and void area can be correlated as shown in Figure 3 (Basaran et al. 2002). EM results in the formation of voids. These voids decrease the contact area between the trace and solder ball, which increases the current density at the interface, driving further void growth (Yeh, Choi & Tu 2002). The presence of voids increases the overall resistivity of the joint in an exponential fashion. High resistivity and small contact areas lead to increasing temperature, both in the joint and associated traces as shown in Figure 3(b). Increasing temperature during operational life of the solder joint is not only a concern for the materials of the joint itself, but also for the surrounding components in the integrated circuit that could be damaged by thermal expansion or diffusion.

It is necessary to evaluate how joint geometry and design will affect current density distribution, as it is clear that current density is coupled to resistivity and temperature increases that could degrade both the solder joint and nearby electronic units. Temperature and EM degradation depend on diffusion of particles, so the various types of diffusion must be investigated in order to understand the type of damage a joint will undergo.

2.3.3. Activation Energy for Diffusion

The activation energy for diffusion differentiates the types of diffusion occurring in a solder joint, including the self-diffusion of Sn atoms, the interstitial diffusion of Cu atoms, and grain boundary diffusion. Table 1 shows that Sn self-diffusion has the highest activation energy, followed by grain boundary diffusion, and Cu diffusion along the a-axis and c-axis of the Sn matrix.

Table 1. Diffusion-related values for Sn, Cu, and grain boundary diffusion for the purpose of determining which types of diffusion will dominate at specific temperatures and sample morphologies. [1](Singh & Ohring 1984), [2](Meakin & Klokholm 1960), [3](Dyson, Anthony & Turnbull 1967)

Element	Type of Diffusion	Activation Energy (kJ/mol)	Diffusivity (cm^2/sec)	$D/D_{lattice, Sn}$
Sn	Bulk Self-Diffusion	108.5[1]	$1.6 x 10^{-18}$ (1)	1
	Self-Diffusion along a-axis	123.0[2]	$4.6 x 10^{-21}$ (1)	0.003
	Self-Diffusion along c-axis	107.1[2]	$2.8 x 10^{-18}$ (1)	1.75
Cu	Interstitial Diffusion along a-axis	33.1[3]	$4 x 10^{-9}$ (3)	$2.54 x 10^{9}$
	Interstitial Diffusion along c-axis	16.7[3]	$2.0 x 10^{-6}$ (3)	$1.25 x 10^{12}$ (3)
Sn, Cu, Ni, Ag	Grain Boundary Diffusion	48.9[1]	$1.3 x 10^{-8}$ (1)	$2.13 x 10^{9}$ (1)

The differences in activation energy result in wildly varying diffusivities, with Cu diffusion along the c-axis being 10^{12} times faster than Sn self-diffusion and grain boundary diffusion being 10^{9} times faster. These values can be explained in part by looking at the tetragonal crystal structure of beta tin, shown in Figure 4. Sn self-diffusion relies on a vacancy hopping mechanism, whereas Cu diffusion relies on empty interstitial

sites that common in pure Sn. By looking at Figure 4(b) and (c), it is evident that diffusion along the open structure of the c-axis is preferable to the less spacious a-axis. Cu diffusivity along the c-axis is radically greater than Sn self-diffusion by virtue of having empty Sn interstitial sites and an open structure along the c-axis (Dyson, Anthony & Turnbull 1967). The high grain boundary diffusivity relative to Sn diffusivity can be explained similarly. Grain boundaries are areas of imperfect bonding, resulting in a higher energy than the aligned lattice. Atoms at a high-energy boundary will more easily break their bonds to neighboring atoms, allowing them to migrate (Li & Basaran 2009).

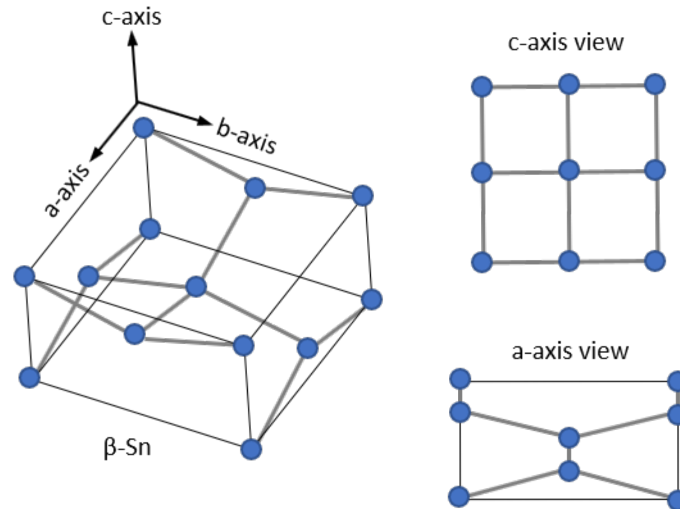

Figure 4. Body-centered tetragonal beta-Sn unit cell and atomic bonds shown in tilted view, along the a-axis, and along the c-axis.

By looking at which types of diffusion should be active in different joint geometries and testing conditions, EM damage can be linked to the diffusion of specific species.

2.4. Effect of Diffusion Type

2.4.1. Sn Self-Diffusion

Sn self-diffusion requires the highest activation energy and therefore should only dominate at high temperatures. Sn atoms move by hopping from vacancy to vacancy, and as a result, create a vacancy flux in the opposite direction of atom migration (Chen & Liang 2007; Ke et al. 2011). Since Cu diffusion is interstitial in nature, to be discussed in the following section, only Sn diffusion contributes to vacancy accumulation at the anode of the joint. Figure 8 shows a comparison between an as-manufactured solder joint with thin Cu traces on either side and a joint that has undergone EM testing at 180°C, well above half of the melting temperature of the solder. At this temperature, Sn self-diffusion should be active, creating a vacancy concentration at the anode. Due to the current crowding effect discussed earlier, the most rapid EM occurs at the corner of the anode closest to the electron flow. The white dashed line and arrow in Figure 5(b) indicate the electron flow coming into the joint, meaning that the void, also indicated by a white arrow, indeed nucleated in that area (Ke et al. 2011). While there doesn't appear to be a significant amount of damage to either of the Cu traces and minimal IMC formation, suggesting little Cu diffusion, perpendicular sectioning of the joint revealed large IMC particles. Void formation would protect the Cu trace or other under bump metallization from consumption, as it would no longer be in contact with the solder. High temperatures will enhance tin, copper, and grain boundary diffusion, but the joint will fail due to the void formation driven by Sn atom migration instead of excessive under bump metallization consumption and IMC formation (Ke et al. 2011). In a joint of roughly 145 μm and few alloying elements, the Sn grains should be large and grain boundary area correspondingly small, meaning the grain boundary diffusion would not play a large role in the degradation of this joint.

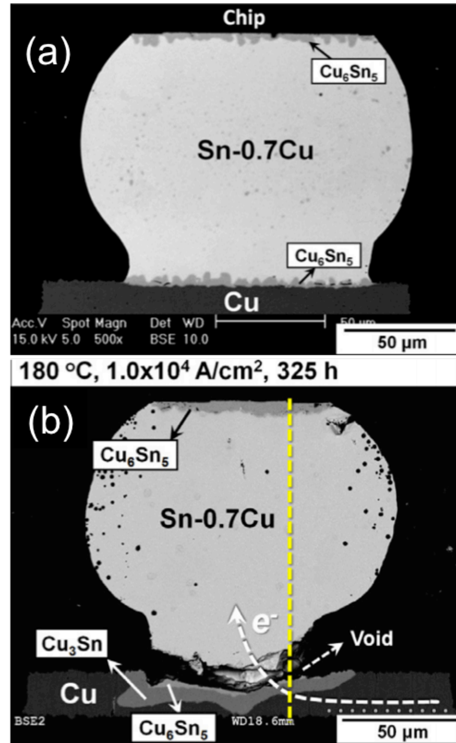

Figure 5. SEM images of cross-sectioned Sn-0.7Cu solder joints in the (a) unstressed condition and (b) after current stressing of 1.0×10^4 A/cm^2 at 180°C for 325 hours. A void has propagated across the solder-Cu interface in (b), a hallmark of Sn diffusion (Ke et al. 2011).

2.4.2. Cu Diffusion in Sn

The nature of Cu diffusion in Sn has been a matter of some debate since the 1950's. The β-tetragonal Sn lattice provides two main diffusion pathways for solute atoms: substitutional diffusion through vacancy hopping and interstitial diffusion. A substitutional solute atom has the option to hop into two vacancy sites; the nearest neighbor sites that reside in the basal (a-b plane) or the next nearest neighbor sites along the c-axis (Nicholas 1955). The jump length in the basal plane is 5% shorter than that

along the c-axis (Nicholas 1955), which results in substitutional diffusion via vacancy hopping being approximately 2 times faster along the a- or b-axis than diffusion along the c-axis (Khosla & Huntington 1975). In contrast, an interstitial site located at [x(a/4), y(a/4), z(c/8)] where x, y, and z are odd integers would have the fastest movement along the c-axis because the interstitial sites would be stacked on top of one another with a smaller length separation than along the a- or b-axes (Nicholas 1955, Liu et al. 2016). These two diffusion pathways would both display anisotropy, but in opposite directions with substitutional diffusion fastest along the a- and b-axes and interstitial diffusion fastest along the c-axis (Khosla & Huntington 1975, Nicholas 1955). Electromigration studies on Ag, Au (Shi & Huntington 1987), Cu (Dyson, Anthony & Turnbull 1967), and Ni (Yeh & Huntington 1984) diffusion in Sn have all found large diffusion anisotropies with c-axis diffusivity orders of magnitude greater than a-axis diffusivity, suggesting that diffusion of these solutes occurs by interstitial diffusion.

Typically, the type of diffusion that a solute atom would experience in a solvent material is decided by a ratio of their atomic radii. By Hägg's rule for interstitial solid solutions, if the solute to solvent radii ratio is less than or equal to 0.59 then the solute atom can occupy an interstitial site, therefore small atoms like C, B, N, and O are often interstitial diffusers (Pollock 1993). In the case of Cu diffusion in Sn however, the ratio of atomic radii R_{Cu}/R_{Sn} is approximately 0.9, making Cu an unlikely candidate for interstitial site occupancy. That noted, Hägg's rule was calculated for close-packed structures like face-centered cubic and hexagonal closed-packed, and β-Sn is a highly distorted tetragonal lattice with no close-packed planes which could allow it to accommodate larger interstitial atoms (Pollock 1993, LLoyd, Tu & Jaspal 2004). The

large radius ratio between Cu and Sn would then suggest substitutional diffusion as the expected diffusion path, but inspection of the Cu-Sn phase diagram provides a counter argument. The phase diagram shown in Figure 6 demonstrates the very limited solid solubility of Cu in Sn, only 0.7 wt% Cu. This low solid solubility would not be expected for a substitutionally diffused atom and instead follows more closely with interstitial diffusion (Pollock 1993). The inclusion of interstitial atoms would cause local straining in the lattice and as more and more solute atoms occupy interstitial sites the lattice strain energy would increase until the formation of a second phase becomes energetically favorable. This process is evident in the low solid solubility of Cu in Sn and the formation of the IMC Cu_6Sn_5 immediately upon solidification. This is in contrast with the known substitutional system between Sn and Pb where Pb can accommodate up to 19.2 wt% Sn and no second phases are formed (Saunders & Miodownik 1990).

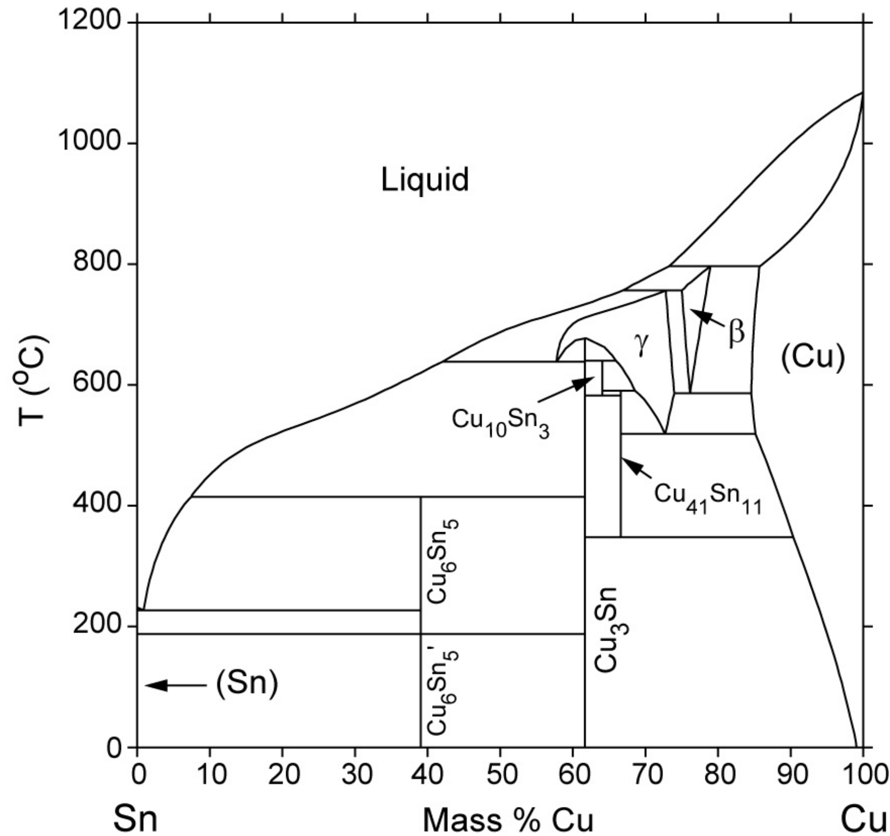

Figure 6. Cu-Sn Phase Diagram (reproduced from NIST Material Measurement, Phase Diagrams and Computational Thermodynamics database, accessed at https://www.metallurgy.nist.gov/phase/solder/cusn.html)

The following trends summarize diffusion of Cu in Sn: highly anisotropic and most rapid along the c-axis, low solid solution solubility, and immediate formation of second phase. These three trends support the theory that Cu diffusion in Sn is interstitial. The only stumbling block to acceptance of the interstitial diffusion theory is the large radius ratio between Cu and Sn. Literature has termed metals like Sn and Pb that exhibit anomalously rapid diffusion of large solute atoms (mostly noble or near noble) “fast diffusers” or “open” metals (LLoyd, Tu & Jaspal 2004, Mehrer 2007) and suggest that

instead of purely interstitial diffusion, a combination of interstitial and substitutional diffusion is taking place. The combination of interstitial and substitutional diffusion has been called the "dissociative mechanism" and is the ability of an atom to switch between an interstitial site and a substitutional site. When the atom jumps from a substitutional site into an interstitial site, it creates a vacancy that may help to accommodate the strain created by having a large atom in a small interstitial site (LLoyd, Tu & Jaspal 2004, Mehrer 2007, Mehrer & Divinski 2009). Alternatively, the interstitial solute atom could simply be tied to the vacancy and not hop into it, a phenomenon termed an "interstitial-vacancy pair" (Decker, Candland & Vanfleet 1975, Nakajima & Huntington 1981). A final potential method for mitigating the strain caused by the large radius ratio is simply to note that the atomic radius for an ion in a metal matrix may not be constant and can vary with valency. If the ionic radius of a Cu atom is actually smaller than the 1.28 Å cited in the periodic table, then the radius ratio between Cu and Sn may decrease to acceptable levels for interstitial diffusion. Most recently, the diffusion of Cu, Ag, Au, Zn, and Cd in Sn was studied using first principle and *ab initio* molecular dynamics methods by Liu and collaborators (Liu et al. 2016). Simulation of the diffusion of the above listed metals found very low energy barriers to interstitial diffusion along the c-axis, supporting the interstitial diffusion theory (Liu et al. 2016). A lattice schematic and diffusion activation energy plots illustrate these findings neatly and reproduced in Figure 7. Interestingly, simulations showed that interstitial Cu atoms would pair with vacancies, as suggested in the "interstitial-vacancy pair" mechanism, and slow Sn self-diffusion by limiting the number of vacancies (Liu et al. 2016).

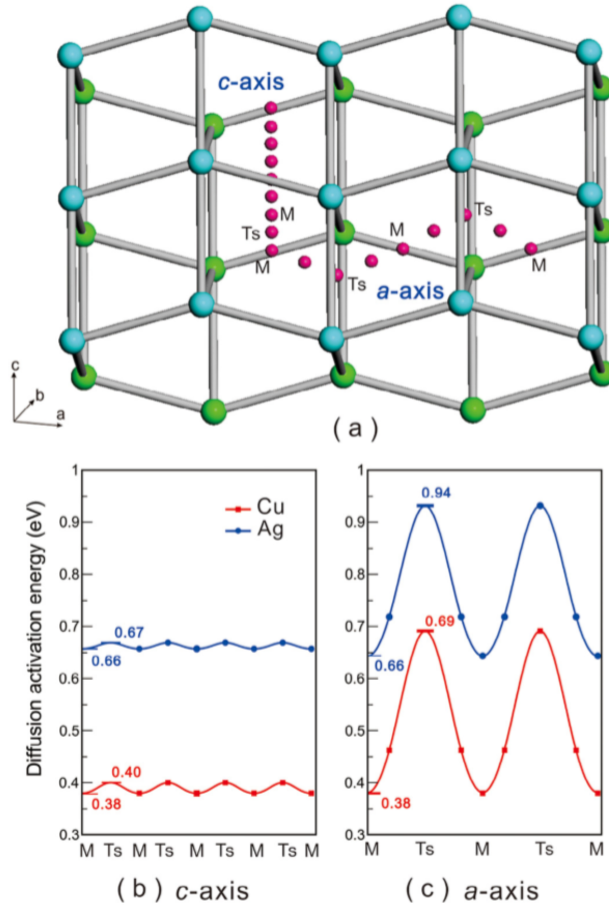

Figure 7. (a) Schematic of interstitial diffusion pathways (pink balls) in the β-Sn lattice (cyan and green balls) along the c-axis and axis. (b and c) Diffusion activation energy curves for interstitial diffusion along the c-axis and a-axis. Points marked M represent interstitial sites at (x/4, y/4, and z/8) and Ts represents a transitional site between interstitial sites (Liu et al. 2016).

The anisotropic diffusion of Cu in Sn has been shown experimentally in a multitude of studies and is in line with the expected results of interstitial diffusion. While the precise nature of Cu diffusion in Sn requires more research, the interstitial diffusion theory of Cu in Sn will be taken as fact for the remainder of the work in this thesis. The

following paragraphs describe the physicals effects of interstitial Cu diffusion in Sn during electromigration.

Cu diffusion is responsible for excessive under bump metallization consumption and formation of the IMC species Cu_6Sn_5 and Cu_3Sn (Ke et al. 2011). Figure 8 shows the same type of joint as in Figure 5, with an undamaged joint in (a) and an EM tested joint in (b). Where Figure 5 looked at high temperature degradation, Figure 8 looks at low temperature. At 60°C, lower activation energy diffusion types dominate, meaning that Cu migration will control the EM damage (Chen & Liang 2007; Huntington & Grone 1961). This evident in the fact that even in the current-crowded region in the bottom left corner of Figure 8(b) does not show large void formation, as would be characteristic of Sn diffusion. Instead the Cu trace has been severely degraded and large amounts of IMC have formed throughout the bulk of the solder ball and at the cathode interface. The electrons enter the joint through the bottom trace, driving the Cu atoms of the trace into the solder matrix through the fast diffusion corridors provided by the c-axis of the Sn structure. Cu atoms from the trace and solder react with Sn to form Cu_6Sn_5 and Cu_3Sn, which are both more brittle and less conductive than the solder alloy and contribute to increasing the overall resistivity of the joint (Huntington & Grone 1961; Lu et al. 2010). There is an abrupt decrease in Cu diffusivity at the cathode of the solder joint, where Cu atoms would transition from rapid interstitial diffusion in Sn to slower, self-diffusion in the Cu trace (Yeh, Choi & Tu 2002). A large concentration of Cu atoms forms at the cathode, leading to formation of a thick IMC layer, not seen at the anode where the Cu is diffusing from (Gan & Tu 2002).

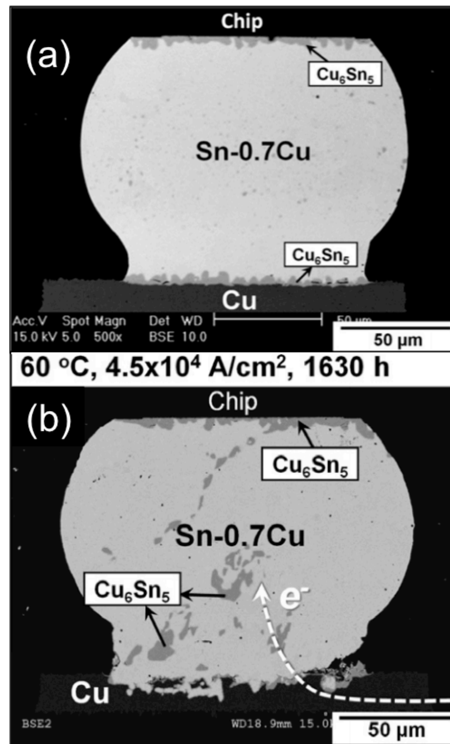

Figure 8. SEM images of cross-sectioned Sn-0.7Cu solder joints in the (a) unstressed condition and (b) after current stressing of 4.5×10^4 A/cm^2 at 60°C for 1630 hours. Large amounts of IMC compound have formed and the Cu trace at the anode has been degraded (Ke et al. 2011).

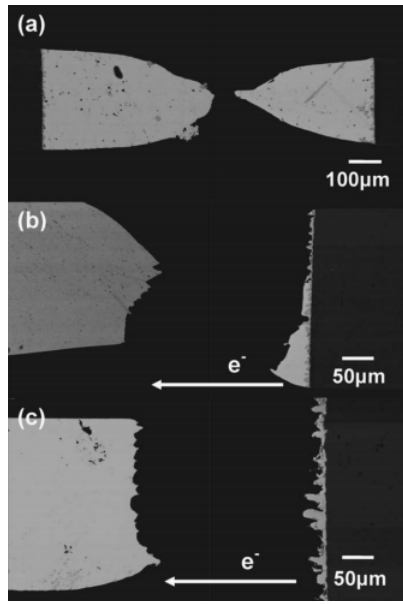

Figure 9. SEM images of cross-sectioned SnAgCu solder joints after tensile testing and (a) no EM, (b) 3.3×10^{3} A/cm^{2} at 100°C and (c) 5.0×10^{3} A/cm^{2} at 100°C. Variation in EM testing resulted a transition from ductile to brittle fracture (Ren et al. 2006).

Cu diffusion and the formation of intermetallics at the joint-trace interfaces cause a transition from ductile to brittle failure of solder joints that has been extensively researched (Ren et al. 2006; Yeh, Choi & Tu 2002; Lu et al. 2010). An as manufactured solder joint will exhibit ductile failure through the center of the solder joint whereas an EM tested joint will fail in a brittle manner, along the interface between the IMC layer at the copper-solder interface and the solder bulk (Tu 2003; Lu et al. 2010). Figure 9 shows the transition from ductile failure in a control joint to the brittle failure of a joint EM tested at 5.0×10^{3} A/cm^{2} at 100°C (Ren et al. 2006). Since the IMC is still attached to the Cu interface on the right side of the joint, the bonding between the IMC and Cu is stronger than that between the IMC and the solder. This is not a problem when the IMC

layer is thin, as in Figure 9(a) or 8(a), but when it grows due to Cu diffusion it becomes a weak point and leads to brittle failure at lower stresses (Lu et al. 2010). Joints with voids caused by Sn diffusion would also fail at lower stresses, but in a ductile manner that absorbs more energy than a brittle failure and therefore last longer before completely severing electrical contact (Lu et al. 2010).

2.4.3. Grain Boundary Diffusion

Grain boundary diffusivity, while not as rapid as Cu diffusivity, is still 10^9 times faster than Sn self-diffusion and requires investigation (Singh & Ohring 1984). The grain boundary area and therefore the grain size in the material determine the degree to which grain boundary diffusion will play a role. This is shown in Figure 10 where a Monte Carlo simulation-based algorithm was used to calculate the effective diffusivity of the SAC405 solder alloy (Li & Basaran 2009). Effective diffusivity takes into account Sn lattice diffusivity and grain boundary diffusivity. Increasing temperature accelerates lattice diffusivity, which is independent of grain size and therefore should show the same curve for various grain sizes. The percentage of effect diffusivity due to grain boundaries depends on the grain boundary area available, which increases with decreasing grain size as shown in the plot. This is of special interest because of how alloying elements and processing affect the microstructure of solder joints.

The impetus for creating more complex solder alloys comes from the fact that additional alloying elements like indium, cerium, zinc, and lanthanum can improve mechanical properties of lead-free solders by decreasing melting points, increasing creep rupture life and failure strain (Lin & Lin 2009). However, additional elements react with the Sn matrix to form intermetallics and these serve as heterogeneous nucleation sites for

Sn grain growth, creating a finer grain structure with increased grain boundary area (Lin & Lin 2009). In a 2009 study by Hsiu-Jen Lin, Jian-Shian Lin, and Tung-Han Chuang, EM lifetimes of Sn-3Ag-0.5Cu and Sn-3Ag-0.5Cu-0.5Ce-0.2Zn were compared. Although adding cerium and zinc reduced the formation of whiskers on the solder ball surface, the grain structure of the joints became exceedingly fine and they showed lower EM lifetimes than the regular Sn-Ag-Cu solder. Interestingly they also found that EM lifetimes could be increased by plating the Cu traces with nickel, which is more resistant to dissolution (Lin et al. 2005), preventing the degradation of the Cu trace and excessive IMC formation (Lin & Lin 2009).

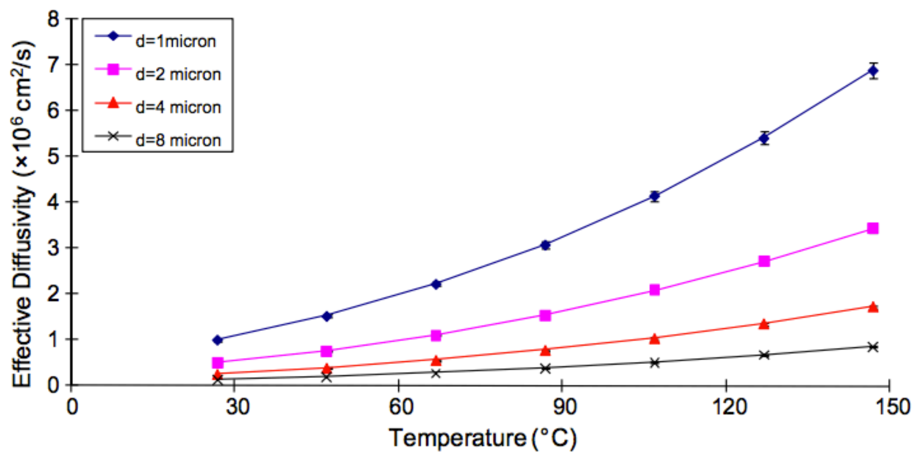

Figure 10. Effective Diffusivity of 95.5Sn-4.0Ag-0.5Cu, due to vacancy diffusion along grain boundaries, as a function of temperature at varying grain sizes. Data derived from a Monte Carlo simulation-based algorithm. Diffusivity decreases with increasing grain size due to decreasing grain boundary area (Li & Basaran 2009).

2.5. Grain Orientation Effects

The importance of grain orientation has already been highlighted by the anisotropy in diffusion characteristics along the a-axis vs. the c-axis for Cu and, to a lesser degree, Sn diffusion. The c-axis provides a diffusion highway for Cu atoms meaning that joints with a large number of Sn grains with c-axis oriented parallel to the electron flow will experience rapid IMC formation and metallization layer consumption during EM (Chen et al. 2015; Chen et al. 2013; Lu et al. 2008; Chen, Guo, et al 2015). Figure 11 illustrates this concept neatly, using 400 μm sandwich solder joints tested under 1.5×10^4 A/cm^2 at 90°C for 250 hours (Chen et al. 2013). Looking at the top set of images in Figure 11, it is evident that some solder joints grew thicker IMC layers compared to the others and this can be explained by using EBSD to analyze the Sn grain orientations in the joints, which is shown in the bottom set of images. When the c-axis is parallel to the electron flow, indicated by a red grain like in (a), Cu diffusion is the fastest, leading to growth of a thick IMC layer at the cathode. Whereas in a grain with the c-axis perpendicular to the electron flow, like the blue grains in (g) and (h), diffusion must occur along the a-axis and will be much slower, resulting in a very thin IMC layer. The relationship between the misorientation angle, the angle between the c-axis and electron flow, and IMC layer thickness was described by J.-Q. Chen et al. to follow a cosine-squared relationship (Chen et al. 2013).

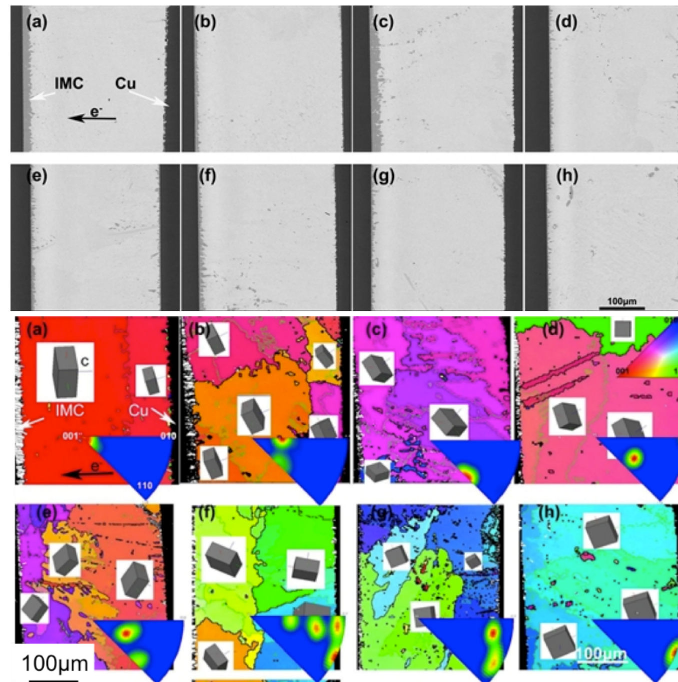

Figure 11. Eight sandwich solder joint structures after undergoing current stressing of 1.5×10^4 A/cm^2 at 90°C for 250 hours. The top set are SEM images of joints after EM and the bottom set are Sn inverse pole figure orientation maps of the same joints (Chen et al. 2013).

In the mid 2000's researchers began to focus on the effect of grain orientation and grain boundaries on EM damage. Lu and collaborators (Lu et al. 2008) demonstrated IMC buildup along grain boundaries parallel to the electron flow in bicrystal solder joints containing grains with very different c-axis orientations. Grains with the c-axis more closely aligned with the electron flow experienced rapid IMC growth due to Cu diffusion while grains with the c-axis perpendicular to the electron flow experienced void growth due to Sn diffusion along the grain boundary. The angle between the c-axis and electron flow was defined as the θ angle (also referred to as the α angle, but we will use θ for the

sake of clarity). It was determined that a joint would be more resistant to EM when it contained grains with larger θ angles and more susceptible with smaller θ angles. Chen et al (Chen et al. 2013) EM tested a series of polycrystalline solder joints with a range of θ angles and grain sizes. They correlated the average c-axis orientation of the joints with the thickness of the interfacial IMC that grew during testing. Samples with smaller θ angles had thicker interfacial IMC layers than those with larger θ angles (Chen et al. 2013). Sn grain orientation relative to the electron flow clearly had a significant impact on IMC growth, however the grain structure of these joints was inconsistent. Each sample contained multiple grains with various orientations and grain sizes, complicating the relationship between grain orientation and IMC growth. Without pre-testing EBSD characterization it is also unclear if the grain structure was constant or evolved during testing, as we will show is possible. Grain boundaries are also rapid diffusion pathways for Cu and Sn, however the high density of boundaries and variation between samples were not taken into account.

In order to most accurately determine the effect of grain orientation on EM, specific c-axis orientations need to be isolated in single crystal joints instead of averaged over several grains. Tasooji, Lara, and Lee (Tasooji, Lara & Lee 2014) investigated EM in a series of prefabricated C4 solder bumps and found that IMCs grew along high angle grain boundaries. They did not draw any clear relationships between grain orientation and IMC growth, likely due to the limited variation in orientation their bumps exhibited. In contrast Huang et al (Huang et al. 2015) found grain orientation to be the controlling feature in IMC growth in their study on flip chip solder bumps, although IMC particles grew near grain boundaries instead of along them as reported by Lu et al (Lu et al. 2008)

and the samples contained different grain boundary densities. The discrepancies between these studies highlight the difficulty of interpreting EM results in polycrystalline samples. EM damage will be accelerated in Sn grains with low θ angles and samples with high grain boundary densities, but the relationships between microstructure and IMC morphology, distribution, and growth rate are still unclear. To focus on grain boundary and grain orientation effects, Huang et al (Huang et al. 2016) conducted EM tests on solder joints with a single horizontal grain boundary between high and low θ angle grains. When electrons flowed from a low θ grain to a high θ grain, an IMC layer built up at the grain boundary. When electrons flowed from a high θ grain to a low θ grain, voids nucleated at the cathode Cu-solder interface and little IMC growth was observed. In this case, grain orientation determined whether voiding or IMC growth occurred rapidly, and the horizontal grain boundary affected where IMC particles would grow in the bulk. This result suggests that grain orientation determines whether a joint will fail due to crack propagation through interfacial voids or due to embrittlement caused by IMC growth. The presence of grain boundaries will affect where and how IMC particles coarsen, which in turn has been shown to affect the strength of the solder (Lin, Hu et al. 2005; Deng et al. 2005). Further study of single and bicrystal solder joints will lead to greater understanding of the void and IMC growth that impact solder joint strength and reliability.

Most recently, Shen and Chen (Shen & Chen 2017) discussed variations in interfacial IMC growth due to θ angles with the following conclusions: low θ angles result in rapid IMC growth, intermediate θ angles result in dissolution of interfacial IMC on the anode and regrowth on the cathode, and high θ angles result in no interfacial IMC

growth. However, exclusively post-mortem analysis again makes the relationship between as-fabricated microstructure and IMC growth unclear and the variation in grain size makes individual bumps in this study difficult to compare. Tian et al expanded this work in a 2018 study where they analyzed cross-sectioned polycrystalline SnCuNi solder joints before and after EM testing (Tian et al. 2018). They showed that when the c-axis of the Sn grain was aligned with the electron flow and directed towards the surface of the cross section, the growth of bulk IMC particles was visible as they formed hillocks that protruded from the sample surface. This study (Tian et al. 2018) and Huang et al's 2015 (Huang et al. 2015) and 2016 (Huang et al. 2016) studies are some of the few to discuss growth of IMC particles in the solder bulk as opposed to grain boundaries and it is consistently correlated with low θ angle grains. Low θ angle β-Sn grains will experience slow Cu diffusion that builds up in the grain and causes IMC particles to nucleate in the solder bulk.

To date, the orientation of Sn grains relative to the electron flow has been random, as no processing technique has been put into place to control it. There is a tradeoff between decreasing the likelihood of getting large c-axis oriented grains by decreasing grain size and increasing grain boundary diffusivity due to larger grain boundary area (Lin, Lin & Chuang 2009; Chen, Guo, et al 2015). Since lattice diffusion along the a-axis of Sn presents the lowest diffusivity values, single crystal joints with the a-axis oriented along the electron flow would be most resistant to EM damage (Chen et al. 2015). The use of a strong magnetic field during reflow to select for specific grain orientations has been suggested, due to the slight variation between the magnetic susceptibilities of Sn

single crystals along the a-axis vs. the c-axis (Chen, Guo, et al 2015). Results of this technique are inconclusive, as there are very few studies that have been done.

CHAPTER 3

GRAIN ORIENTATION-ACCELERATED INTERMETALLIC GROWTH IN SINGLE AND BI-CRYSTAL SN SOLDER JOINTS, INVESTIGATED BY EBSD AND X-RAY MICROTOMOGRAPHY

3.1 Introduction

It is clear from this extensive body of work that both grain orientation and grain boundaries of β-Sn have a significant effect on EM damage. Research has shown that the θ angle of a Sn grain will affect IMC growth, both interfacial and bulk, as well as the rate of Cu dissolution and void growth. Grain boundaries appear to determine where IMC particles will nucleate or build up. However, determining consistent relationships between microstructure and EM damage has been complicated by the use of a variety of testing structures, from pre-fabricated solder bumps to solder bars or lines, which makes comparison between studies difficult as each testing geometry may result in different current crowding and joule heating effects (Chen & Liang 2007; Tu 2003). The use of polycrystalline samples also limits the conclusions that can be drawn because grain boundary diffusion and grain orientation will always be confounded. The fabrication of multiple solder joints without current crowding and joule heating effects, with identical fabrication, and comparable grain orientations and grain sizes would simplify the investigation of grain orientation and boundary effects on EM damage. Furthermore, the majority of analysis is done on post-EM-tested sample cross sections which is effective at determining average changes in microstructure when compared to as-fabricated samples but cannot capture the initial state of a particular sample. Without a comprehensive

understanding of the samples' initial state one cannot determine how its grain structure evolved into its final state, nor any relationship that the IMC or void growth may have had with the initial structure.

Finally, IMC growth and void growth are usually considered separately from one another and are only discussed as a direct result of orientation instead of in a dynamic relationship with it. This study will show how IMC growth, void growth, and grain structure evolution are interrelated processes that must be analyzed together to fully understand the microstructure that results from EM. Understanding these three processes in relation to each other will shed light on different IMC morphologies, Sn matrix recrystallization, and the phenomena of void faceting and burrowing. A simple and symmetric sample geometry ensures that there will be no localized current crowding or joule heating effects and a unique fabrication technique creates samples with comparable grain orientations and grain sizes. In order to fully capture the initial and final sample states SEM, EBSD, and X-ray microtomography analysis will be used in concert. SEM imaging will determine differences in surface characteristics such as hillock or IMC formation. Grain structure will be analyzed with EBSD to determine θ angles and microstructural changes due to testing or IMC growth. Most importantly, the initial and final 3D void and IMC morphologies will be quantified using nondestructive X-ray microtomography. This allows for the calculation of void and IMC growth rates and their relation to grain orientation, as well as 3D visualizations that are critical in understanding 2D SEM and EBSD analysis. This multimodal approach allows for the understanding of IMC growth, matrix transformation, and void evolution in a novel way.

3.2 Materials and Experimental Procedure

In order to isolate large single and bicrystal regions in the Sn solder, the solder joints were fabricated in a two-step process. First a larger initial sample was created and then it was sectioned into smaller solder bar joints, as seen in Figure 12 (a). The initial sample was a sandwich-joint composed of 250 μm thick Sn ribbon (Indium Corporation, 99.99% purity), placed between two oxygen-free high conductivity (OFHC) Cu pellets (McMaster-Carr, Cu alloy 101). The Sn ribbon was coated in Indalloy Flux #5 RMA (Indium Corporation) prior to stacking to remove Cu and Sn surface oxides during reflow. The solder stack was reflowed on a standard hot plate in ambient air with a hold of 20 seconds above 232°C and then transferred to a pre-chilled Cu surface to cool at a rate of 3.4°C/second. The solder stack was then cross-sectioned, mounted in epoxy, and mechanically polished finishing to a 0.05 μm colloidal silica finish. The joint microstructure was investigated using a polarized light microscope and Zeiss Auriga SEM with an EBSD detector to determine the orientation and size of the Sn solder grains and an EDS for compositional analysis. TSL OIM Data Collection and Analysis software were used to gather the EBSD patterns and create OIM maps.

Once single and bicrystal regions larger than 500 μm were identified, one half of the solder stack was sectioned into rectangular solder bars 500 μm wide, 500 μm thick, and 4.25 mm long by electrical discharge machining (EDM). The bars were mechanically polished to a cross-section area of 300 μm by 300 μm to remove any surface damage induced by EDM. EBSD mapping was done on the front surface of the solder bars to confirm the grain orientation and size, as shown in Figures 12 (b) and (c). EBSD

mapping of the sides of several solder bars confirmed that the horizontal grain boundaries extended through the width of the samples.

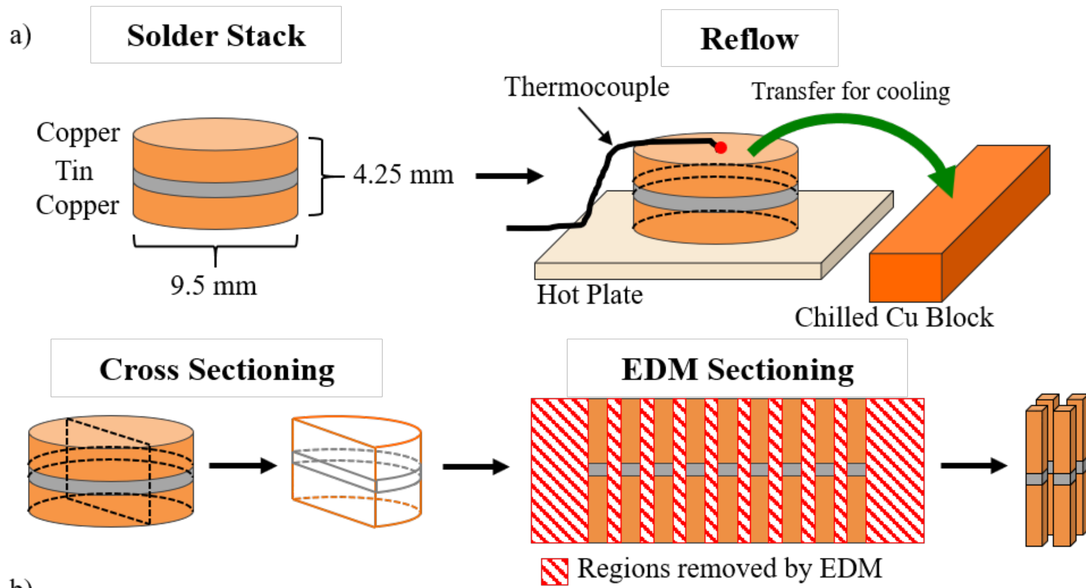

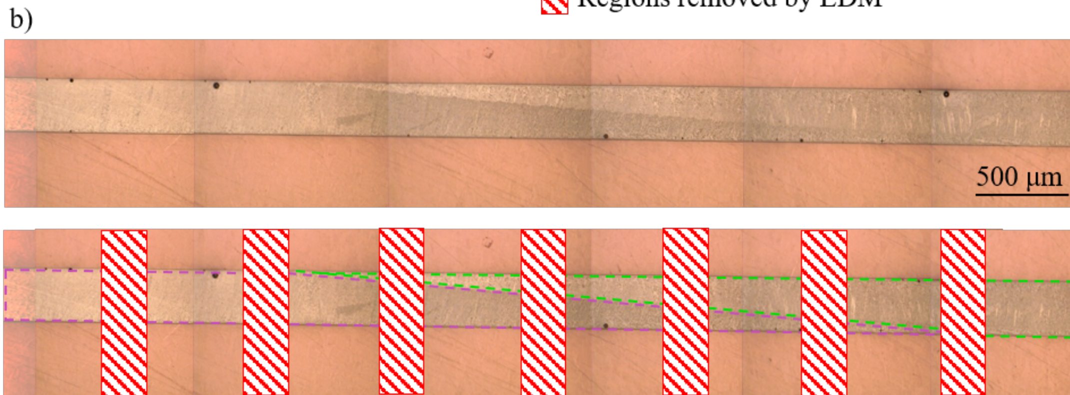

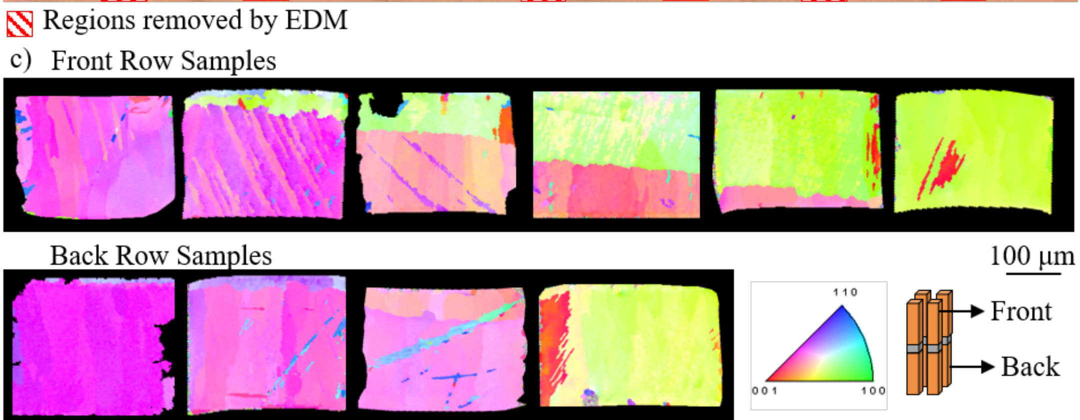

Figure 12. Single and bicrystal solder bar fabrication procedure (a), expected samples (b), and preliminary EBSD for sample selection (c).

IMC growth due to thermal aging and EM depends on Cu diffusion. Interstitial diffusion of Cu in Sn is highly anisotropic with the fastest diffusion direction along the c-axis of the Sn grain. The solder bars were ranked from slowest to fastest diffusion by comparing the angle between the c-axis of the β-Sn grain and a vector normal to the Cu/solder interfacial plane, the θ angle. Six samples were selected for testing, three for thermal aging and three for EM testing. Each sample set contains a slower diffusion sample with a large θ angle, a faster diffusion sample with a smaller θ angle, and a bicrystal sample containing a small θ angle grain and a large θ angle grain, shown in Figure 13. Specific θ angles are summarized in Table 2.

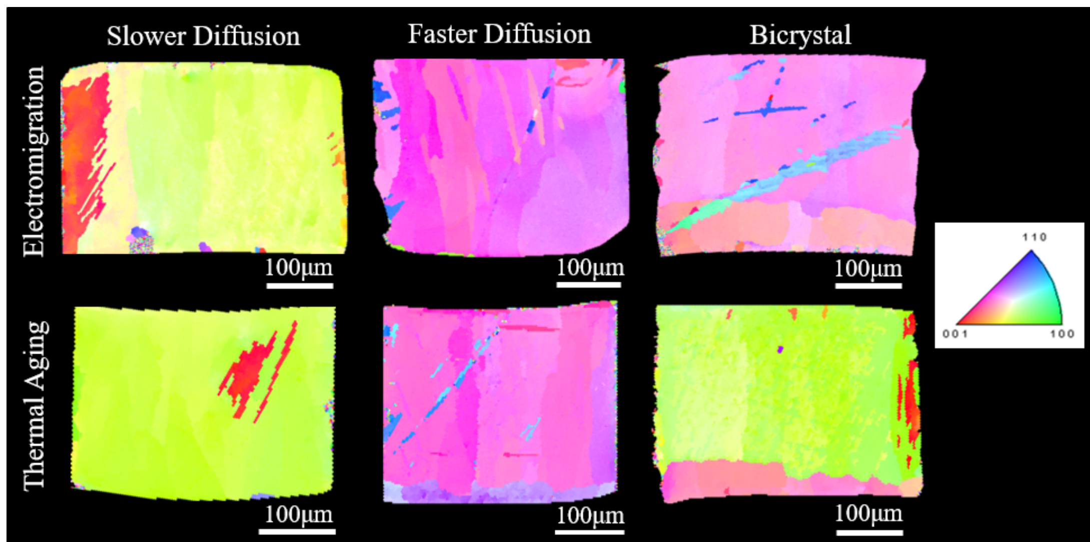

Figure 13. OIM maps of samples selected for testing. The slower and faster diffusion samples are composed of a single grain with a predominant single orientation, while the bicrystal samples contain two grains with different orientations.

Table 2. Angles between the c-axis and electron flow direction for samples to be used in testing.

	Single Crystal Slower Diffusion	Single Crystal Faster Diffusion	Bicrystal
EM Testing	72°	50°	55°/88°
Thermal Aging	76°	50°	54°/84°-86°

EM testing was done at a current density of 1 x 10^4 A/cm^2 for 100 hours. The testing fixture was placed inside an insulated box furnace and heated to 140°C to avoid temperature fluctuations due to resistive heating. If the sample thermocouple indicated a temperature increase beyond 140°C, forced-air cooling was applied to restabilize the temperature. Lab-scale x-ray microtomography (Zeiss 520 Versa) was done before and after EM testing in order to analyze and quantify IMC and void growth. The tomography scans were first filtered in ImageJ to increase contrast and remove noise and then segmented in Avizo 9 (ThermoFisher Scientific, Waltham, MA, USA) to create 3D volume renderings for analysis and visualization. Thermal aging was done at 140°C for 100 hours in order to compare the microstructural changes driven by current flow and those driven by thermal diffusion. Since the thermal aging samples would not experience temperature fluctuations that would require application of additional cooling or heating methods, these samples could be tested in a vacuum chamber. After testing, samples were imaged in the SEM and scanned using x-ray tomography before being mounted in epoxy

and mechanically polished to 0.05 μm colloidal silica finish. The mounted samples were analyzed in the SEM using EBSD and EDS to determine changes in grain structure and composition.

3.3 Results and Discussion

3.3.1 Surface and Grain Orientation Evolution

The six solder joints were imaged in the SEM before and after testing, as shown in Figure 14. The faster diffusion and bicrystal EM-tested samples exhibited severe surface deformation and consumption of the Cu anode. The slower diffusion EM-tested sample and the thermally aged samples maintained planar faces similar to their as-fabricated condition. Of the thermally aged samples, only the faster diffusion sample, Figure 14 (k), showed surface relief, in the form of fine teardrop protrusions from the sample surface. Focused ion beam (FIB) cross sectioning revealed these protrusions to be Cu_6Sn_5 particles that coarsened during aging. Each of the EM-tested samples had a different characteristic surface morphology after testing, illustrated in Figure 14. The slower diffusion sample showed teardrop patterns similar to the faster diffusion sample in the thermal aging set, although not as extended from the sample surface, resembling Sn hillocks seen by Chen et al (Chen et al. 2013) and Tian et al (Tian et al. 2018) during EM testing of solder bumps. The difference in protrusion height is due to the formation of a more tenacious surface oxide on the EM sample, as the EM testing was conducted in air while the thermal aging was done in vacuum. As with the thermally aged sample, these teardrops are caused by IMCs coarsening at and slightly beneath the sample surface. The faster diffusion sample in the EM set experienced major degradation with the surface rippling and cracking in the vicinity of the ripples. The Cu anode consumption is evident

from the SEM images, particularly in the bottom right corner of the joint where it appears to have crumpled inward as the Cu diffused away from the anode interface. Inspection of the bicrystal sample revealed evidence of Cu_6Sn_5 hexagonal needles, formed close enough to the sample surface to be visible in multiple locations, highlighted by white arrows in Figure 15 (d). These needles are unique to the bicrystal EM-tested sample and were not seen on any others.

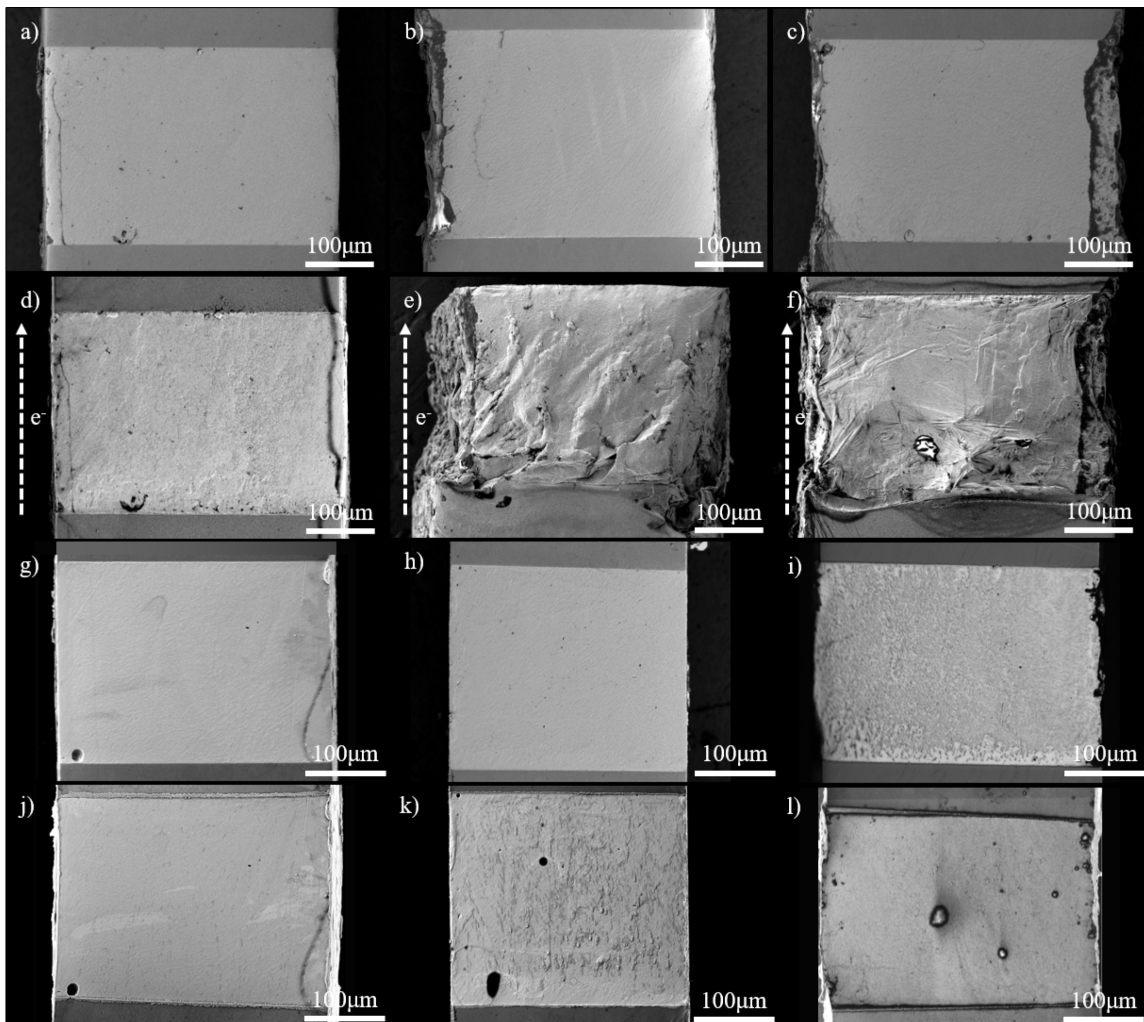

Figure 14. SEM images of solder bar samples before and after EM testing (a-f) and thermal aging (g-l): Pre-EM (a-c), Post-EM (d-f), Pre-aging (g-i), Post-aging (h-l).

Slower diffusion samples (left column), faster diffusion samples (center column) and bicrystal samples (right column) are shown. The dashed white arrow shows the electron flow direction.

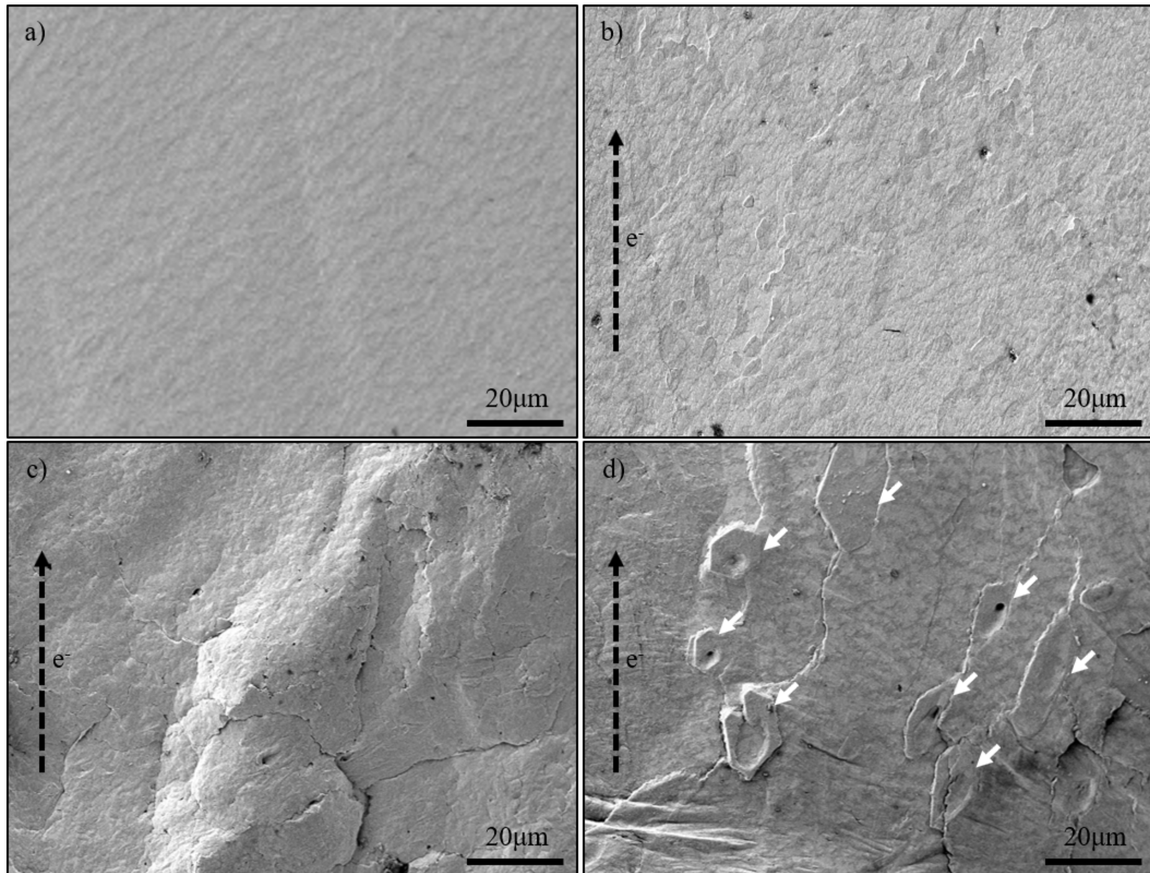

Figure 15. SEM images of solder joint surfaces before (a) and after EM testing (b, c, d). Variations in IMC growth between the slower diffusion sample (b), faster diffusion sample (c), and the bicrystal sample (d) cause a variety of surface deformations, in particular the growth of hexagonal Cu_6Sn_5 IMC needles (indicated with white arrows) visible on the surface of (d).

Samples were analyzed using EBSD to determine the original orientation of the β-Sn grains then repolished and analyzed again after testing. The post-testing EBSD maps reveal if and how the β-Sn grains recrystallized in response to thermal aging and EM. As shown in Figure 16, the initial grain orientation was retained in all cases for the thermally aged samples. In contrast, the EM-tested samples experienced a range of recrystallization, seen in Figure 17. The slower diffusion sample showed minor recrystallization in isolated patches over the joint surface. The faster diffusion sample transformed almost entirely into columnar grains of Cu_6Sn_5 that spanned the length of the joint. The bicrystal sample recrystallized entirely.

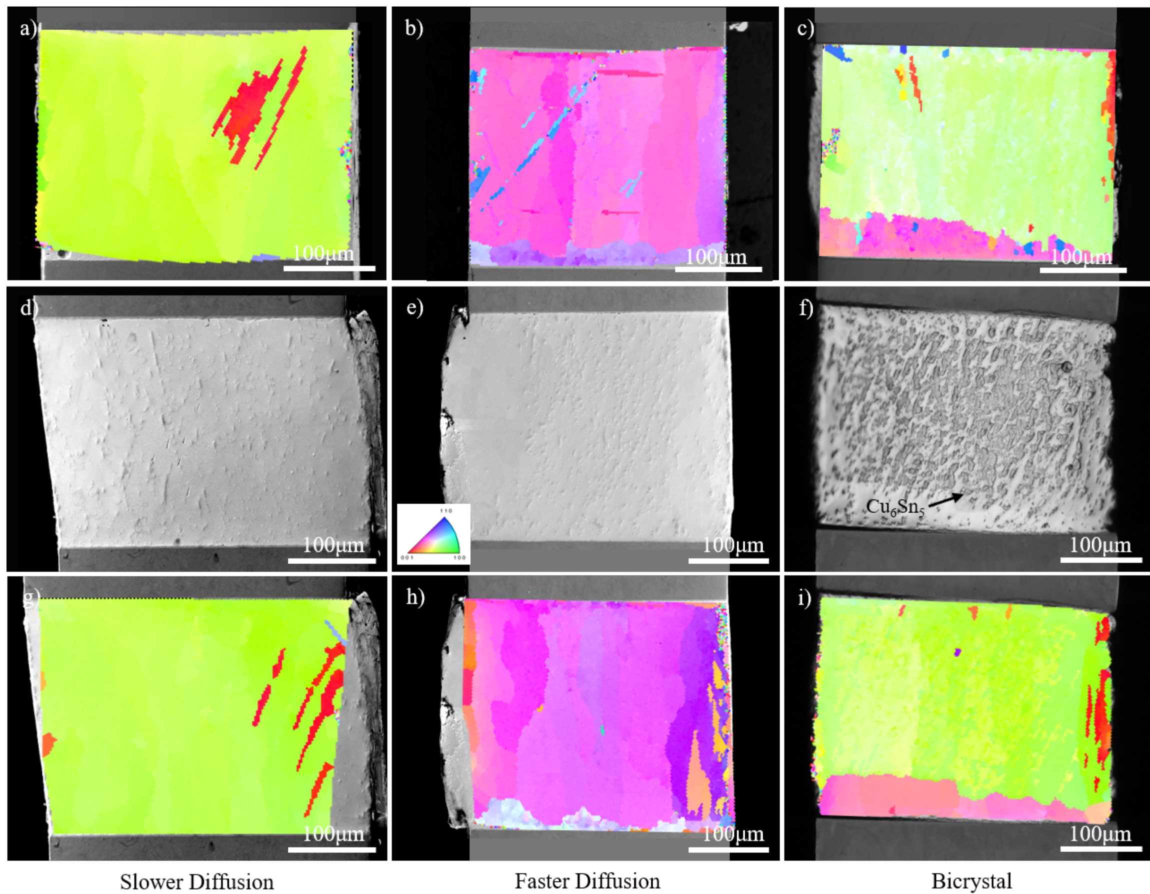

Figure 16. SEM images and OIM maps of pre- and post-thermal aging samples showing the change in grain structure after aging: (a, b, c) pre-aging OIM maps, (d, e, f) SEM images of repolished sample surfaces after aging, (g, h, i) post-aging OIM maps.

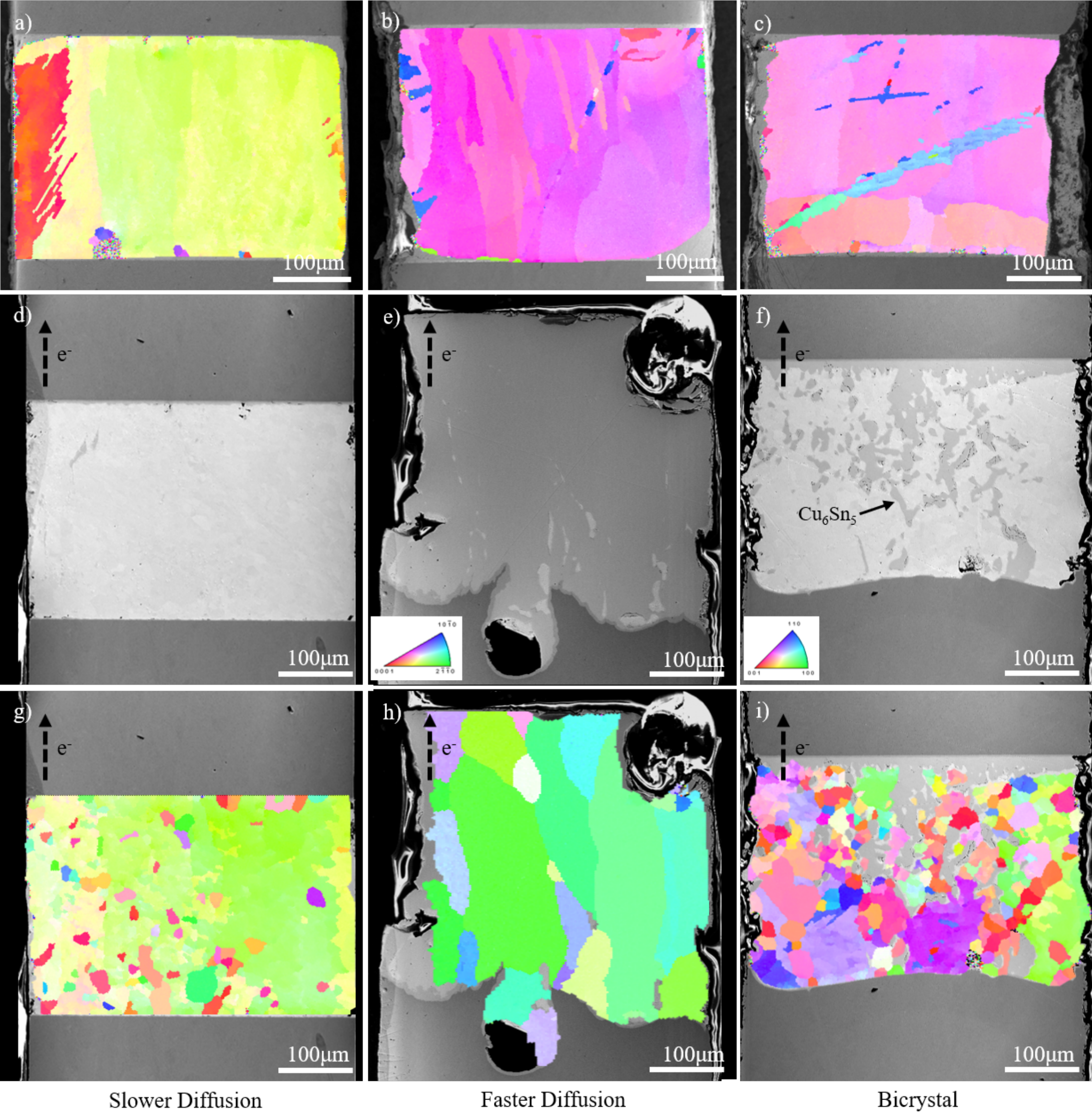

Figure 17. SEM images and OIM maps of pre- and post-EM tested samples showing the change in grain structure after testing: (a, b, c) pre-EM OIM maps, (d, e, f) SEM images of repolished sample surfaces after testing, (g, h, i) post-EM OIM maps.

Although both thermal aging and EM experiments were conducted at the same temperature and duration, their effects on solder joint microstructure were significantly different. The thermal aging samples showed little surface deformation after testing and EBSD mapping showed that initial crystal orientations remained unchanged. The EM-tested samples experienced rapid IMC and void growth, which had a pronounced effect on their final microstructures. While both sets of samples had similar θ angles, the driving force for diffusion in the EM case is much higher than the in the thermal aging case. In EM, atomic diffusion is driven by both by electron momentum transfer, often called the "electron wind force," and by the chemical potential gradient created by the variation in atomic concentrations of Sn and Cu throughout the solder joint (Gan & Tu 2005). Diffusion in the thermal aging case is only driven by the chemical potential gradient and is therefore much less damaging than the EM-driven diffusion. Only the thermally aged bicrystal joint experienced appreciable IMC growth. Rounded IMC particles coarsened at the grain boundary, as Cu that diffused through the fast diffusion grain could not easily diffuse into the slower diffusion grain. Similarly, Cu diffusion in the slow diffusion grain was concentrated along subgrain boundaries and formed elongated IMC particles. The bicrystal nature of the joint lead to more IMC growth during thermal aging than in the single crystal samples where grain orientations were isolated. This suggests that in slow diffusion cases like thermal aging, grain boundary diffusion might be the controlling feature for IMC growth.

While thermal aging did not result in Sn grain structure changes or void growth, the IMC coarsening is still important to note. Isothermal aging above at 150°C has been

shown to reduce the shear strength of lead-free solder joints due to coarsening of bulk IMC particles (Lin et al. 2006; Deng et al. 2005). Thermal cycling has proven to be significantly more damaging than thermal aging due to the build-up of plastic deformation at strained regions in the joint that then become crack nucleation sites (Lin et al. 2006). This crack growth was captured in a 2019 study by Regalado and collaborators (Regalado et al. 2019) on thermal cycling of nano-sintered silver solder. Tomography reconstructions showed the formation of a dense network of microcracks that lead to solder delamination from the substrate and substrate cracking. The relatively short timescale of these experiments (100 hours), single temperature hold, and slower diffusion kinetics are why the thermally aged samples show little damage in comparison to EM-tested samples. However, comparisons between thermally cycled and power cycled joints would be an interesting direction for future work.

3.3.2. IMC Growth

Cu_6Sn_5 and Cu_3Sn IMCs form when Sn-rich solders in contact with Cu substrates undergo reflow, thermal aging, and EM. In order to characterize the morphology and distribution of IMC particles in the solder bulk, the solder bars were scanned using x-ray microtomography before and after EM testing. The thermally aged bars were only scanned after aging. X-ray microtomography nondestructively captures 3D structural information based on density, as x-rays will attenuate differently based on the density of the materials they pass through. Phases with higher densities appear brighter and lower densities darker, allowing for differentiation between Cu, tin, IMCs, and void space. This technique enables quantification and visualization of IMC and void volumes that lend unique insight into their evolution and relation to the surrounding solder matrix. Pre-

testing scans revealed that there were no IMC particles in the solder bulk larger than 1 μm, i.e., the resolution of the tomography scans. SEM imaging of the sample surfaces prior to testing showed finely interspersed IMC particles, the majority of which were less than 1 μm long and 0.5 μm wide. While these particles could not be captured by pre-test tomography scans, SEM analysis confirmed the size and distribution of particles to be consistent across all six samples.

Renderings of the Cu_6Sn_5 bulk IMC that grew in the EM samples are presented in Figure 18. A significant difference in IMC growth is immediately evident from the reconstructions. The slower diffusion sample shows rod and plate-like IMC particles, the faster diffusion sample transformed almost completely into Cu_6Sn_5, and the bicrystal sample formed a dense network of rod-like IMCs. Quantification of the IMC volumes and comparison to the initial scan allowed for the calculation of an IMC growth rate for each sample, shown in Figure 19. The faster diffusion sample grew at a rate of 202.5 μm^3/second, approximately 26 times faster than the bicrystal sample and approximately 500 times faster than the slower diffusion sample.

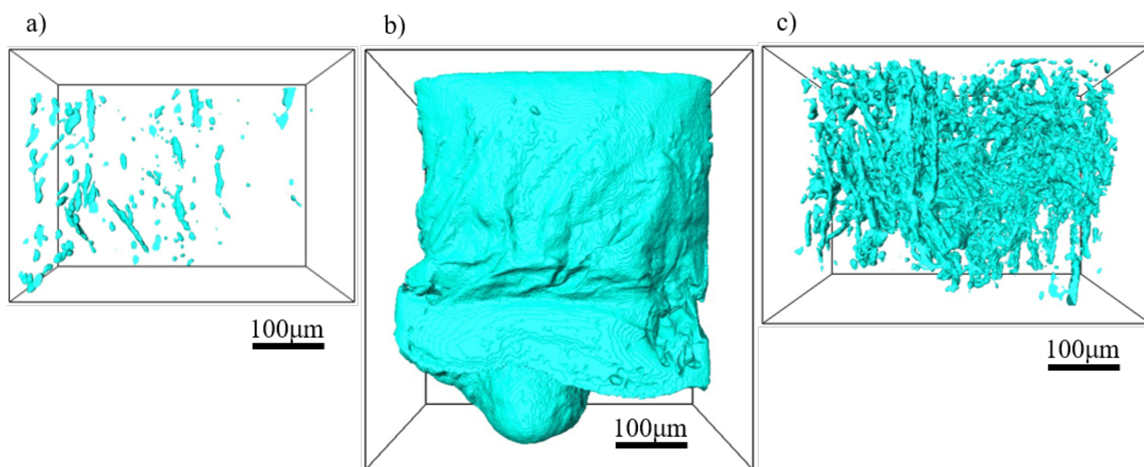

Figure 18. IMC volume after EM for: (a) slower diffusion sample, (b) faster diffusion sample, and (c) bicrystal sample.

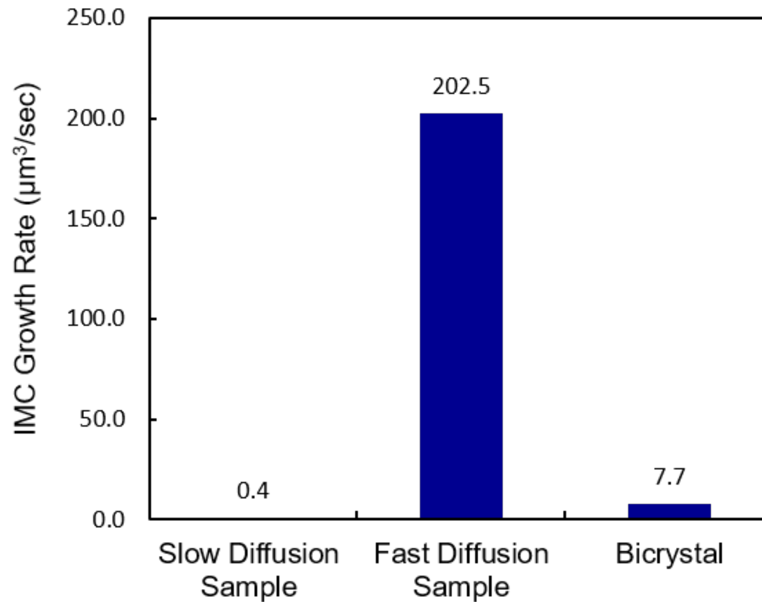

Figure 19. IMC growth rates for each sample, showing drastically rapid IMC growth in the faster diffusion sample.

The thermally aged samples experienced much less IMC growth as evidenced in Figure 20. In order to resolve the fine IMC particles in the thermal aging samples and avoid interference from interfacial voids, only the center volumes of each sample were segmented. The slower diffusion and faster diffusion single crystal samples developed an even dispersion of fine IMC particles with no difference in particle size or distribution. IMC particles in the bicrystal sample coarsened in two regions, forming elongated particles in vertical chains in the slower diffusion grain and rounded particles clustered along the plane of the horizontal grain boundary. EBSD analysis of the slow diffusion

grain of the bicrystal sample shows that it contains vertical subgrain boundaries. Cu diffusion would be slightly more rapid along the vertical boundaries than the surrounding matrix, causing IMC particles to nucleate and grow along these boundaries preferentially. The high angle horizontal grain boundary served as a fast diffusion pathway for Cu to migrate laterally within the sample, creating a sheet of rounded, as opposed to elongated, particles.

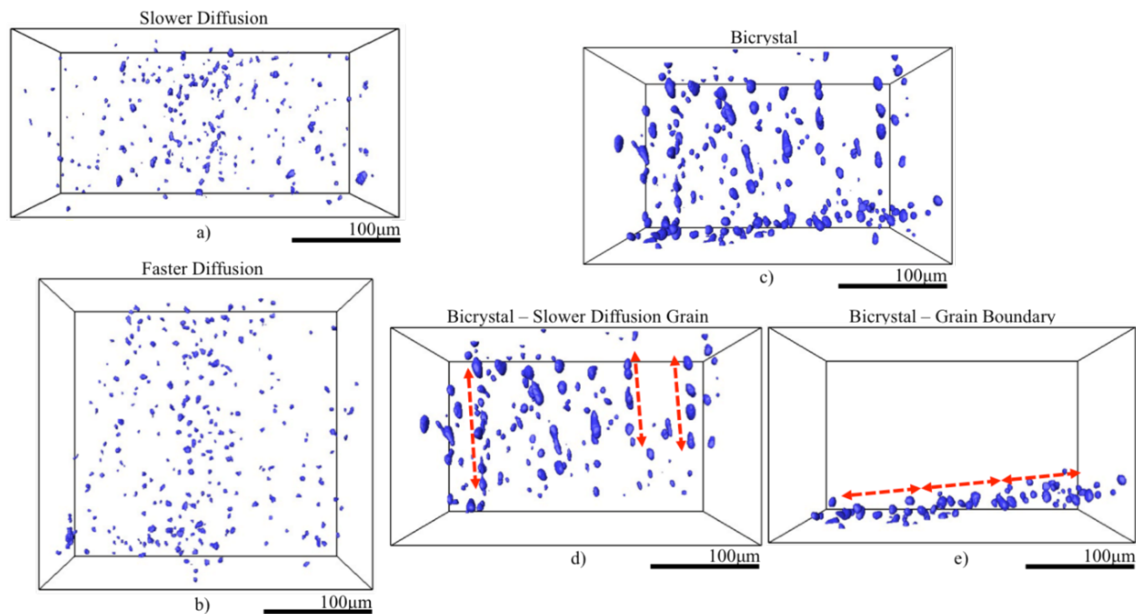

Figure 20. IMC volumes from sample centers after thermal aging for: (a) slower diffusion sample, (b) faster diffusion sample, and (c) bicrystal sample. Two distinct IMC distributions visible in the bicrystal sample, (d) elongated particles with vertical alignment in the slower diffusion grain and (e) rounded particles that coarsened along the horizontal grain boundary. Cu diffusion directions are shown by red arrows.

3.3.3. IMC Characterization

3.3.3.1 Morphology and Growth

The ability to visualize the bulk IMC particles using microtomography was of particular interest in these experiments. In 2016 Mertens, Kirubanandham, and Chawla used x-ray microtomography to capture rapid IMC growth in a solder joint after close to 500 hours of EM testing (Mertens, Kirubanandham & Chawla 2016). These experiments were done on polycrystalline joints so relationships between the branched IMC morphology and matrix orientation were unclear, but they proved that x-ray microtomography was a uniquely powerful tool to understand IMC growth. In our work reconstructions of the Cu_6Sn_5 IMC from the EM-tested samples demonstrate two distinct types of IMC growth. In the slower diffusion and bicrystal samples, Cu diffuses into the solder bulk along the c-axis of the β-Sn grain and along grain boundaries where it reacts with the Sn matrix to form Cu_6Sn_5 particles. These particles gradually coarsen over time into rod or plate-like features. The second type of IMC growth is seen in the faster diffusion sample, where Cu diffused to the cathode instead of building up in the solder bulk. The cathode interfacial Cu_6Sn_5 layer grew rapidly towards the anode in large columns instead of forming IMC particles in the solder bulk.

These two types of IMC growth can be clearly differentiated when comparing their orientations and grain size using EBSD, shown in Figure 13. The IMC in the faster diffusion sample is composed of less than 20 columnar grains with similar orientations. The IMC in the bicrystal sample is composed of multiple, fine grains less than 200 μm^2 in area. IMC grains close to the cathode interface tend to have an angle of less than 20° between the (0001) plane and the Cu interface and grow along the [0001] direction. Bulk

IMC particles do not have any consistent orientations. The small angle between the basal plane of η-Cu_6Sn_5 and the Cu interface is consistent across multiple interfacial IMC grains, suggesting an orientation relationshipt between the cathode Cu and interfacial IMC. Previous work has shown that η-Cu_6Sn_5 has the following relations with Cu: $\{0001\}_{\eta\text{-IMC}} // \{011\}_{Cu}$, $\{10\bar{1}0\}_{\eta\text{-IMC}} // \{111\}_{Cu}$, and $\{11\bar{2}0\}_{\eta\text{-IMC}} // \{001\}_{Cu}$ (Suh, Tu & Tamara 2007; Wang, Gan & Hsieh 2010; Zhang et al. 2016; Zhang, Li, et al 2016). Our Cu substrate has a primarily {111} texture so one would expect to see $\{10\bar{1}0\}$ planes of η-Cu_6Sn_5 growing parallel to the interface, however we do not see this orientation. This is because solder joints with polycrystalline Cu substrates, regardless of grain orientation, characteristically show Cu_6Sn_5 growth along [0001] normal to the Cu (Tasooji, Lara & Lee 2014; Jiang & Chawla 2010; Li, Yang & Kim 2012), as seen in our samples. This is likely due to crystals with the fastest growth direction, [0001], normal to the interface growing more rapidly and eclipsing less favorably oriented grains early on in reflow.

The grain orientation differences between the interfacial and bulk IMC in the bicrystal sample are illustrated in Figure 13(c) where the angle between the (0001) plane of the hexagonal Cu_6Sn_5 lattice and the Cu interface has been plotted as a function of distance from the cathode interface. The faster diffusion sample IMC has a consistent orientation of less than 30° with reference to the interface throughout the sample, meaning the IMC grew from the Cu interface towards the anode. Within 50 µm of the cathode interface the bicrystal sample IMC grains pattern off of the polycrystalline Cu and display a small angle between the basal hexagonal place and the interface. Further into the bulk of the bicrystal sample the angle between the basal plane and Cu interface is random, indicating the orientation relationship is no longer present. These bulk particles

did not pattern from a Cu interface, instead they nucleated along high and low angle grain boundaries and therefore have a random crystallographic orientation. Grain boundary coarsening of IMC particles is visible in the thermally aged bicrystal in Figure 16 (c,d,e). The EM-tested bicrystal sample experienced much more IMC growth and Sn matrix recrystallization, providing a high density of grain boundaries for Cu diffusion and IMC growth. Recrystallization caused the initial horizontal boundary, visible in the thermal bicrystal, to be lost. The grain orientation comparison, combined with the morphology difference seen in the tomography scans, supports the hypothesis that the bicrystal sample displays both interface and bulk-nucleated IMC growth. Bulk-nucleated growth results in randomly oriented η-Cu_6Sn_5 particles that are rod or plate-like and interface-nucleated growth results in columnar Cu_6Sn_5 grains with the (0001) plane parallel to the Cu interface. Bulk-nucleated IMC particles are difficult to capture in 2D surface analysis of solder joints precisely because they are mostly in the bulk of the sample and not visible. A few studies have reported IMC growth in the solder bulk, seen as hillocks protruding from polished sample cross sections (Huang et al. 2015; Huang et al. 2016; Tian et al. 2018), but none have shown the 3D structure of the particles or discussed how they might differ from interface-nucleated IMCs.

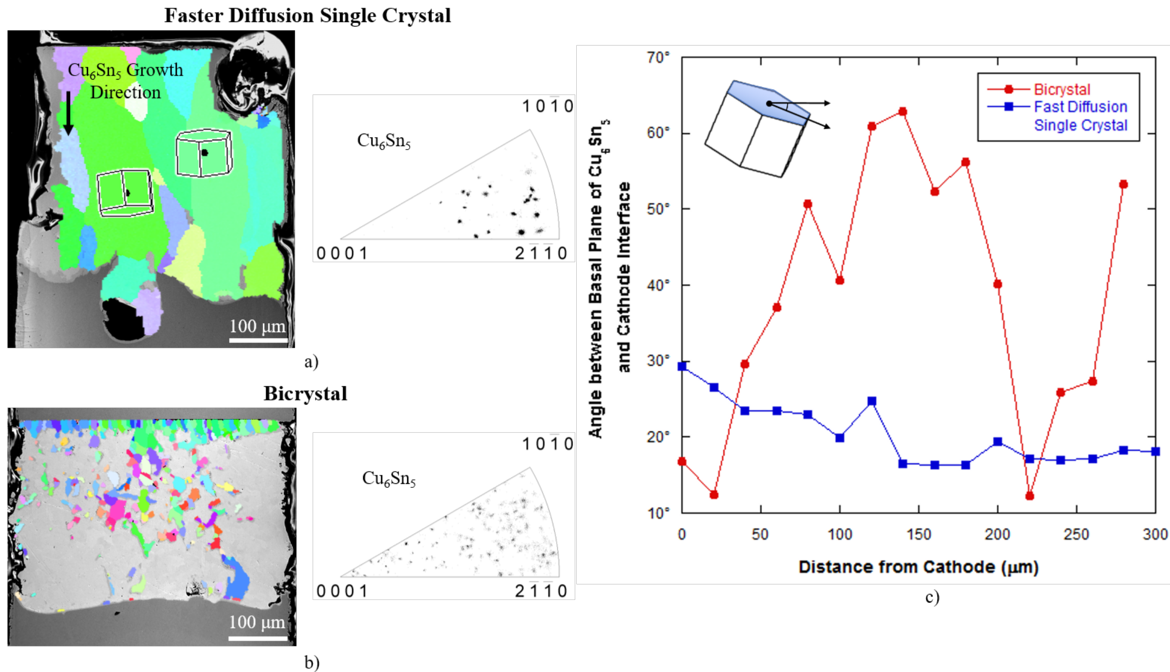

Figure 21. Difference Cu_6Sn_5 IMC growth in the faster diffusion sample (a) and bicrystal sample (b) shown both by EBSD maps, IPF's, and plotting the angle between the basal plane and the Cu interface (c).

This variation in morphology and orientation has strong implications for solder joint reliability, as Cu_6Sn_5 has been shown to display anisotropic mechanical properties (Jiang & Chawla 2010; Song et al. 2012). Jiang and Chawla demonstrated a 20% reduction in strength and a 7% reduction in Young's modulus when comparing Cu_6Sn_5 micropillars indented perpendicular and parallel to the [0001] direction of the hexagonal crystal (Jiang & Chawla 2010). If an entire joint transforms into large grains of Cu_6Sn_5 with similar orientations a crack would easily propagate through the joint along the (0001) planes. This type of fracture occurred during post-EM handling of the faster diffusion sample as the fully transformed joint was very brittle. Imaging and EBSD

mapping of the fracture surface conducted in the SEM showed a transgranular cleaveage fracture that propagated along (0001) planes, parallel and adjacent to the Cu/solder interface. In contrast, disconnected IMC particles would slow crack growth. Since the particles are randomly orientated, the basal planes will not align, making it difficult for a crack to jump into a neighboring particle. If multiple IMC rods fractured, the crack would still have to proceed through the ductile Sn matrix before complete failure could occur. In this manner, the slower diffusion and bicrystal samples would be more resistant to crack propagation than the faster diffusion sample.

3.3.3.2 Relationship to Sn Matrix Recrystallization

Bulk-nucleated IMC particle growth was seen in both the slower diffusion and bicrystal samples. The bicrystal sample exhibited complete recrystallization of the β-Sn matrix and the formation of an interconnected IMC network. The slower diffusion sample showed regions of recrystallization and isolated IMC particles. We believe that a cyclical process links matrix recrystallization and the tortuous IMC morphology. The slower diffusion sample displays an early part of the cycle while the bicrystal sample is a later stage. As IMC particles form and coarsen in the solder bulk, they impose stress on the surrounding Sn matrix. The Sn matrix will recrystallize in response to that stress and the IMC particles provide a heterogeneous nucleation site for new Sn grains to form. This recrystallization forms new grain boundaries in the vicinity of the IMC particle. New IMC particles nucleate along the recrystallized grain boundaries due to the rapid grain boundary diffusion of Cu. Since the recrystallized grain boundaries are connected to the initial IMC particle they nucleated from, it is possible that secondary IMC particles may grow along the boundaries and eventually reconnect with the original particle. In this

manner, originally disconnect particles could become connected, forming the network visible in tomography and EBSD analysis of the bicrystal sample. Over time, the cycle of IMC growth and matrix recrystallization causes the entire solder joint to recrystallize and form a dense interconnected network of IMC particles. The IMC growth/recrystallization cycle is shown schematically in Figure 22 (c).

Early and late stages of this process can be seen in Figure 22 where we compare recrystallization in the slower diffusion and bicrystal samples. The slower diffusion sample shows the early stages of IMC growth and recrystallization. First, IMC particles (outlined in black) coarsen along the low angle subgrain boundaries, shown in blue in Figure 22 (b), (i) and (ii). The fastest IMC growth direction, the [0001] direction, is aligned with the vertical boundaries. Recrystallized Sn grains, shown numbered 1-5 in Figure 22 (b) (i) and (iii), form in response to the IMC growth and surround the IMC particles. The bicrystal sample shows the late stage of this process, where the majority of the joint has recrystallized. Figure 22 (e) shows an EBSD map color-coded by grain maximum Feret diameter with blue grains being the smallest and red the largest. The maximum Feret diameter is the longest distance between any two points along the boundary of a shape, similar to how one would measure the maximum diameter of a shape using calipers. Sn matrix grains surrounding the IMC network are blue or green (small), while those farthest away from the network are red and orange (large). This supports the idea of a continuous recrystallization process where recrystallized grains grow and finer grains nucleate within them where they contact the IMC particles, leading to a gradient in grain size. While recrystallization also took place in the faster diffusion sample, it was not driven by the same cyclic process, since the EBSD map of that sample

indicates the IMC grew as a series of columns that nucleated at cathode interface and consumed the matrix Sn between them as the columns coarsened.

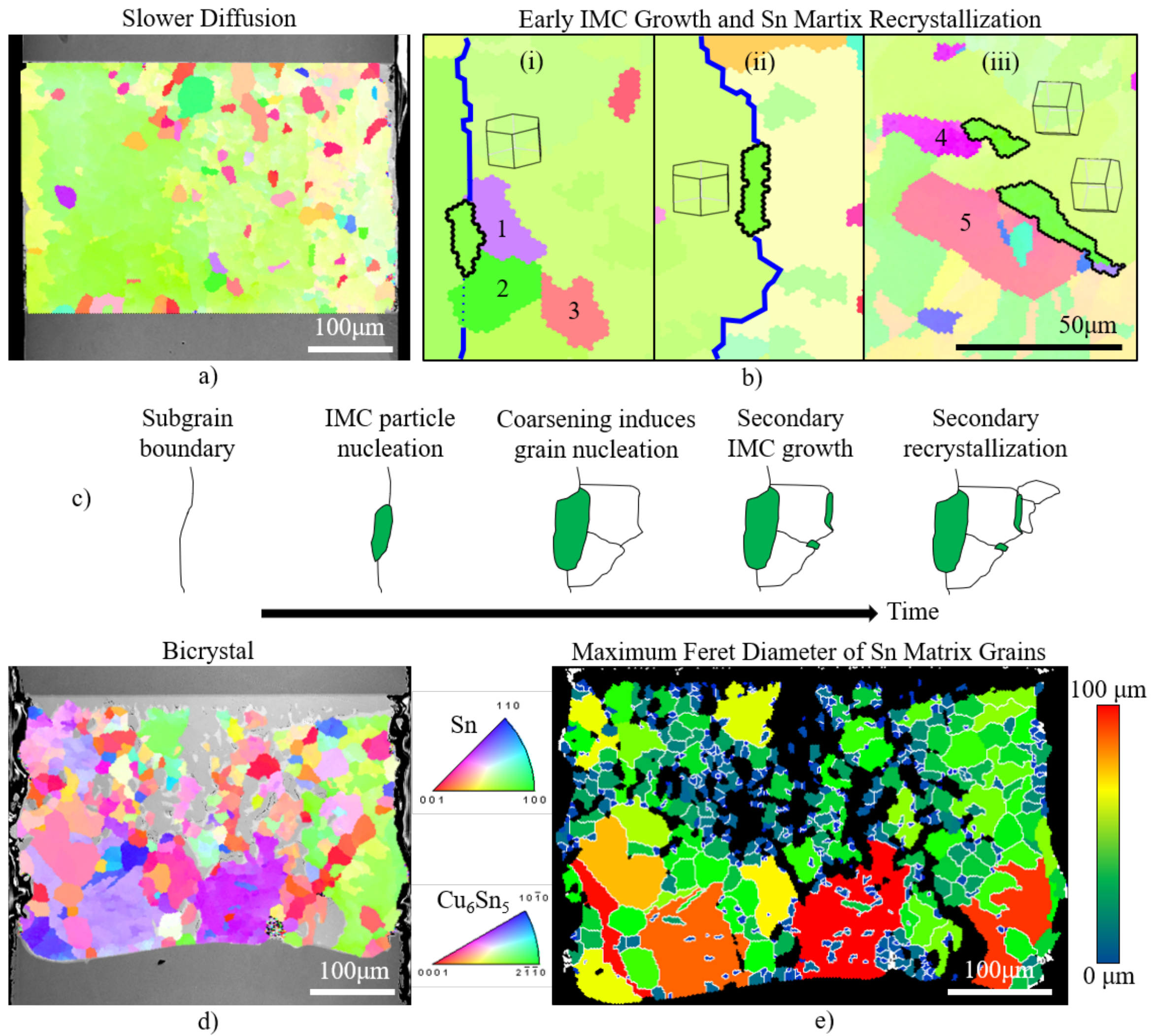

Figure 22. IMC PSN Recrystallization in the slower diffusion sample (a,b) and bicrystal sample (d,e) with recrystallization schematic shown in (c). Magnified regions (b) of the post-EM EBSD map (a) show recrystallized Sn grains (numbered 1-5) and Cu_6Sn_5 IMC particles (outlined in black) along subgrain boundaries (lined in blue). The orientation of the IMC particles is shown using the hexagonal lattice insets. Late-stage recrystallization of the bicrystal sample is shown in (d), where the EBSD map is recolored to show

maximum Feret diameter, smallest grains in blue, largest in red, and grain boundaries in white.

It is well known that solder recrystallizes under thermomechancial stresses, like those seen in thermal and power cycling of microelectronic packages. This recrystallization occurs in localized zones of high strain and temperature due to coefficient of thermal expansion (CTE) mismatches between packaging components and Joule heating caused by current crowding at the solder-metallization interface (Bieler et al. 2006; Ouyang, Tu & Lai 2012; Yin et al. 2012; Matilla & Kivilahti 2012; Bieler et al 2012; Sundelin, Nurmi & Lepisto 2008). In contrast to most solder studies that use either prefabricated packages or solder bumps, the samples in this study have a uniform cross-sectional area across the length of the joint. They are also not attached to a PCB or silicon die that could impose stress on the sample during testing. This means that there are no regions of localized stress or joule heating due to sample geometry and the test configuration ensures a stable temperature so the recrystallization must occur due to stress generated within the sample.

Recrystallization through particle stimulated nucleation (PSN) of new grains has been discussed in the context of grain refinement after cold work and annealing where there is a high density of dislocations surrounding a particle which upon annealing nucleates new highly misoriented grains (Yin et al. 2012; Doherty et al. 1997). In this study, the only source of dislocation pile-up would be the coarsening bulk Cu_6Sn_5 particles, making them a logical nucleation site for new grains. However, PSN has not been explored as a recrystallization mechanism in solder EM studies, possibly for the

following reasons: localized strain or heating zones, difficulty comparing initial and final grain orientations, and use of solder alloys with a range of IMC particle sizes. Strains generated by CTE mismatch between board components, joule heating, or implied mechanical force will affect the entire solder volume and therefore dwarf highly localized strains around IMC particles. Logically a sample would recrystallize in the region with highest strain, around a solder bump neck for example, and PSN recrystallization can only be seen when other strains have been eliminated.

A large focus of this study was the comparison initial and final grain orientations through EBSD and visualization of 3D microstructure using x-ray microtomography. EBSD comparison before and after testing is not by itself unique. By comparing EBSD maps before and after testing, Chen et al showed Sn grain rotation in a solder bump neck due to current crowding and strain during EM (Chen et al. 2015). Telang and Bieler [5,6] showed grain coarsening and orientation trends in SnAg solder under isothermal aging, creep, and thermomechanical fatigue (Telang et al. 2003; Telang et al. 2002). However, the combination of EBSD and tomography is particularly powerful because it connects the evolution of the 2D grain structure with the 3D structure of the solder joint, without damage that could be induced during serial sectioning. Rendering the IMC network in 3D allowed us to see similarities and differences in growth between the three samples, not immediately evident through EBSD analysis. While the slower diffusion and bicrystal samples had very different final EBSD maps, their rod and plate-like IMC structures seen in tomography suggested they showed two stages of the same type of IMC growth. The connection between PSN recrystallization and its enhancement of further IMC growth was only made possible by using both techniques in tandem. Meanwhile, EBSD and

tomography of the faster diffusion sample confirmed that it experienced a distinctly different form of IMC growth from the other two samples. Finally, the use of a simple Sn-Cu system without Ag_3Sn precipitates may have allowed this type of recrystallization to proceed more rapidly, as Ag_3Sn precipitates have been shown to pin grain boundaries and delay recrystallization in creep and thermal fatigue studies (Kerr & Chawla 2004; Borgesen et al. 2018; Lee et al. 2010). The combination of a sample geometry without stress concentrations, rapid IMC coarsening, comprehensive pre and post-test analysis, and a simple two element system may have made it possible to see PSN recrystallization in the context of EM where it had not been seen before.

3.4 Summary

The purpose of this work was two-fold; first, to compare microstructural evolution due to thermal aging and EM done at the same temperature and second, to evaluate those microstructural changes using tomography to visualize and quantify IMC growth and EBSD to determine changes in crystallography. Two sets of single crystal and bicrystal solder joints were fabricated with a range of comparable grain orientations. One set was thermally aged for 100 hours at 140°C and the second set was EM tested for 100 hours at 140°C under a current density of $1x10^4$ A/cm^2. SEM and microtomography analysis allowed for visualization and quantification of IMC growth and relation to grain orientation evolution. We reached the following conclusions.

1. Thermally aged samples did not exhibit grain recrystallization or significant IMC particle growth after aging for 100 hours. EM-tested solder joint evolution varied significantly between slower diffusion, faster diffusion, and bicrystal samples.

2. Two IMC growth processes were discussed: cathode-nucleated columnar Cu_6Sn_5 growth and bulk-nucleated rod-like Cu_6Sn_5 growth.
3. Bulk-nucleated growth of IMC particles was related to β-Sn matrix recrystallization by PSN recrystallization theory, not previously addressed in the context of EM.

This research shows that solder joint evolution under EM is a complex problem that requires a multidimensional analysis approach to understand. The most obvious solution to reduce EM-driven damage is a single crystal solder joint with the c-axis perpendicular to the electron flow, but as we've shown, that might only be a short-term cure. PSN recrystallization at subgrain boundaries will cause an increase in grain boundary density and loss of the original orientation. IMC growth and matrix orientation evolution are interrelated phenomena that should be considered together when trying to determine a future solution for EM-driven damage.

CHAPTER 4

ORIENTATION-DRIVEN VOID EVOLUTION DURING ELECTROMIGRATION, INVESTIGATED BY X-RAY MICROTOMOGRAPHY

4.1 Introduction

Voids are a consistent concern in solder joint reliability since void growth can cause open circuit failure and joint embrittlement (Chen & Liang 2007; Tu 2003). Voids formed due to EM have been described as pancake-like voids (Yeh et al. 2002; Chang, Liang & Chen 2006; Zhang et al. 2006; Chang, Chiang & Chen 2007; Chang et al. 2017; Ho et al. 2016; Han et al. 2012; Lin et al. 2005; Xie et al. 2014), finger or slit-like voids (Tian et al. 2011; Fridline & Bower 1999; Wang, Yao & Keer 2017), or discrete spherical voids (Chang et al. 2017). Pancake-like voids nucleate at current-crowding locations in the solder joint and propagate across the solder-metallization interface, while finger or slit-like voids are formed due to void growth along the current flow direction or collapse of spherical voids (Tian et al. 2018; Fridline & Bower 1999; Wang, Yao & Keer 2017). The type of void that develops is dependent on current-crowding, joint geometry, and, as we will show, local grain orientation.

Voids can be present in as-fabricated samples due to imperfect contact between the solder and metallization layer or due to reacting flux that becomes gaseous during reflow and cannot escape the liquid solder (Li et al. 2012; Qu et al. 2014). Since these voids are bubbles in the liquid solder all voids are initially spherical and typically in contact with a solder/metallization interface, as visible in Figure 12 (a, c, e). Since void growth during EM is driven by vacancy diffusion it will be affected by current crowding, joule heating,

and local grain orientation. The most commonly described void type is pancake voiding, where a single void nucleates at the corner of a solder joint due to current crowding and joule heating and propagates along the solder/metallization interface, eventually causing failure. As discussed above, our sample geometry does not display current crowding or joule heating effects due to a constant cross-sectional area throughout the sample, and as a result, the void growth seen in the solder bars is significantly different from pancake voiding. It more closely follows the nucleation, growth, and coalescence of discrete spherical voids described by Chang et al. who analyzed EM voids using 3D laminography (Chang et al. 2017). Xie et al. also visualized void growth due to EM using x-ray microtomography and reported rapid void growth at the anode within 100 hours of testing (Xie et al. 2014). However, we see two additional void behaviors not previously shown in EM literature: void faceting and burrowing, as described in the following two sections.

4.2 Materials and Experimental Procedure

This chapter details the analysis of voids found in the EM-tested samples described in Section 3.2 of Chapter 3. The materials and experimental procedure are therefore the same as that presented in Section 3.2 and will not be repeated here. The thermally aged samples were not tomography-scanned prior to testing so it was not possible to comment on their void growth. They did not experience the faceting or burrowing behaviors seen in the EM-tested joints because the rate of diffusion is significantly lower.

4.3 Results and Discussion

4.3.1 Void Faceting

The phenomenon of void faceting has been described in a series of simulation papers as the formation of flat faces driven by variations in adatom diffusivity on various crystallographic planes present on the void surface (Kraft & Artz 1997; Sun, Suo & Yang 1997). To the best of the authors' knowledge experimental verification of this phenomena has yet to be reported. It is known from basic crystallographic thermodynamics that surface diffusion will vary with crystallographic orientation due to the difference in atomic arrangement, and therefore binding energy, along different crystallographic planes (Blakely 1973). A material with anisotropic diffusion properties undergoing significant atomic diffusion would be expected to show preferential diffusion along certain directions not only in the bulk of the material, but also along the surfaces of voids present within it. Variations in surface diffusion along different crystallographic planes in β-Sn have been shown by several studies (Qian et al. 2005; Sellers et al. 2010; Eckhold et al. 2015) [59-61]. However, many papers simulating void evolution under current and temperature stressing have ignored crystallographic effects and therefore have discussed void coalescence, fracture, and migration only in the context of spherical, elliptical or cardioid voids (Chang, Chiang & Chen 2007; Chang et al. 2017; Ho et al. 2016; Wang, Yao & Keer 2017; Li et al. 2012; Qu et al. 2014; Pete et al. 2012; Orgutani & Oren 2004).

The combination of high current density and the anisotropic diffusion properties of β-Sn, isolated in single crystal joints in our study, drove certain spherical voids to develop flat, faceted surfaces. The degree of faceting was analyzed by quantifying the

initial and final void sphericities. Sphericity is the ratio between the surface area of a perfect sphere with the same volume as a specific void to the surface area of the actual void. If the void is perfectly spherical, its sphericity will be 1, while a cuboidal void has a sphericity of approximately 0.806, a deviation of 0.19 from a sphere. Deviations from sphericity for voids before and after EM testing are shown in Figure 23, together with reconstructions of representative voids before and after testing. Three trends are clearly visible: (i) voids in the slower diffusion sample show the greatest deviation from sphericity because they have become faceted, (ii) most voids in the faster diffusion sample have remained spherical, and (iii) the bicrystal sample shows both faceting and spherical growth at cathode and anode respectively. The mixed-mode void growth in the bicrystal sample is due to the orientation of the grain surrounding the voids at each interface. The anode voids are surrounded by a faster diffusion grain with a lower θ angle, similar to the faster diffusion sample (55° and 50° respectively). Therefore, the anode voids preserve their spherical shape, while the cathode void is surrounded by a high θ angle grain similar to the slower diffusion sample (88° and 72° respectively) and exhibits void faceting.

While it is unclear how rapidly the bicrystal sample recrystallized, it can be presumed that the PSN-recrystallization began in the bulk of the sample and spread towards the edges over time, leaving the interfacial voids unaffected in the initial stages of the EM test. Recrystallization would have destroyed the original orientation relationships and θ angles. Since the void morphologies match the original orientations, they must have evolved before recrystallization reached the interfaces. This suggests a sequential microstructure evolution where voids change shape early in EM stressing,

followed by recrystallization of the surrounding matrix and IMC growth. Voids initially present at both interfaces disappeared after testing, but their disappearance did not follow clear trends with void size, spacing, or interfacial density. Investigation into how surrounding voids behave after a void disappears will determine if the void collapsed due to backfill by Sn (Hu et al. 2003) or IMC or if the voids coalesced. If the voids coalesced a neighboring void should increase in volume, while if a void collapsed the neighboring voids would remain at a constant volume.

Simulations suggest that the deciding factor that controls whether a void will remain spherical or form facets is the relationship between EM-driven surface diffusion and crystallographically-driven anisotropic surface diffusion (Fridline & Bower 1999; Kraft & Artz 1997; Subramanian, Sofronis & Ponte Castaneda 2005). When EM-driven diffusion is rapid, as in the case of the faster diffusion sample with a small θ angle, a void will maintain a spherical equilibrium shape. When EM-driven diffusion is slower, due to a large θ angle, anisotropic surface diffusion dominates causing voids to facet along low surface energy crystallographic planes. In β-Sn the (100) and (211) surfaces have the lowest surface energy, making growth along those planes energetically favorable (Sellers et al. 2010; Eckhold et al. 2015). Therefore, it is likely that the voids in the slower diffusion sample and at the cathode of the bicrystal sample formed facets along those planes. Belyakov et al. reported crystallographically faceted void formation in several lead-free solder alloys subjected to thermal aging (Belyakov & Atkinson 2010). These void facets appear to have a relationship to the β-Sn matrix orientation and grew in a layered fashion, but further relationships with crystallography were not expanded upon. The voids were faceted in both the as-soldered and post aging conditions and appeared

related to bulk Ag_3Sn and Cu_6Sn_5 IMC particles. In contrast, our samples show a transition from spherical to faceted based on clearly defined differences in diffusion due to EM and anisotropic surface energy effects and are not related to IMC particles, as confirmed by tomography and SEM analysis. Voids in the thermal aging cases did not exhibit faceting within 100 hours, likely due to the slower diffusion kinetics, but might exhibit the phenomenon with longer testing. Further analysis of the relationships between local crystallography and void faceting are in progress.

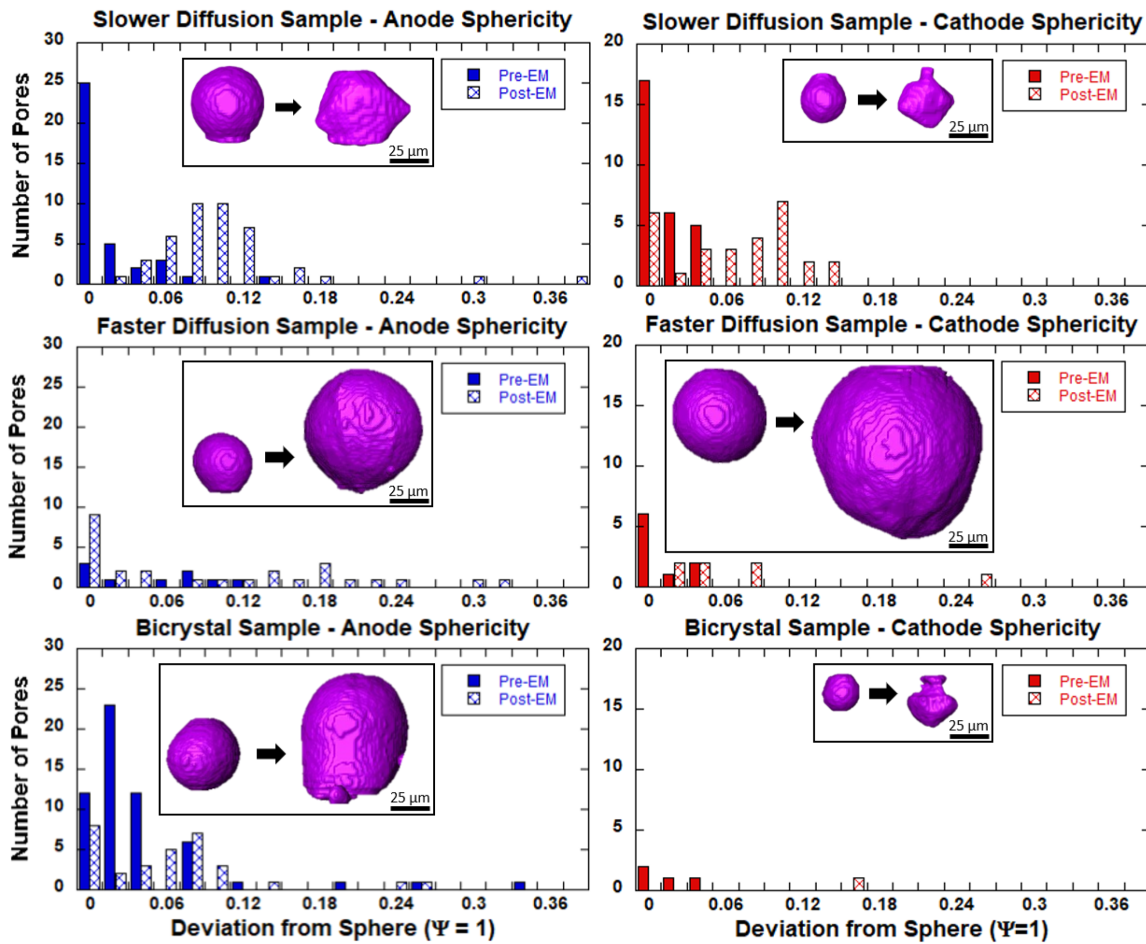

Figure 23. Histograms showing deviation of sphericity in anode and cathode voids before and after EM testing. Deviation from sphericity is determined by the following: $\Psi_{perfect\ sphere} - \Psi_{void}$. Reconstructions of a representative void before and after testing

are shown in the insets. Void faceting is evident in the slower diffusion sample and cathode of the bicrystal sample, while voids remain spherical in the faster diffusion sample and anode of the bicrystal sample.

4.3.2 Void Burrowing

The second unique void behavior seen in our samples is void burrowing. Void burrowing refers to the rapid consumption of Cu surrounding a void causing it to migrate or "burrow" into the Cu interface at an unusually rapid rate compared to the rest of the sample interface. The result is massive localized Cu consumption and void migration opposite the electron flow direction. This behavior only occurred in the faster diffusion sample where interstitial Cu diffusion was expected to be rapid and at the anode interface with the fewest initial voids, visible in Figure 24 (a). Current density in the vicinity of a void is higher than the average cross-sectional current density of the solder joint due to a local reduction in cross-sectional area (Chang et al. 2017; Han et al. 2012; Xie et al. 2014). This causes current crowding around voids and increased atomic diffusion. Figure 24 (d) and (e) show the early stages of this type of void growth at the bicrystal anode which was surrounded by a fast diffusion grain. Rapid Cu diffusion around the void edge causes the void to develop a ridge around the bottom, with a dimple in the middle. The dimple is the result of the void preventing Cu diffusion directly along the electron flow, instead Cu atoms beneath the void must diffuse around it before being able to travel into the solder bulk. This causes a reduction in Cu dissolution right beneath pores and creates small Cu peaks, visible in blue in Figure 24 (e). These Cu peaks correspond to the dimples seen at the base of the void in Figure 24 (d). The faster diffusion sample likely

experienced a similar type of void growth initially, with the difference that the burrowing void nucleated at the interface instead of being present in the as-reflowed condition.

Several features appear to have caused the burrowing behavior. The low θ angle of the grain ensured rapid Cu diffusion and the single crystal nature of the joint ensured that there were no barriers present to hinder diffusion in the sample bulk. While the initial anode surface being nearly void-free might suggest that the interface would experience planar consumption, we see instead that a distribution of voids across the interface ensures a uniform increase in current density across the anode interface (Xie et al. 2014) and therefore more planar Cu consumption. Nucleation of an isolated void lead to current crowding in the center of the interface and rapid diffusion close to the void. It is interesting to note that the single preexisting anode void in the faster diffusion sample did not burrow into the interface and instead expanded and remained at the same position in the solder matrix. The final detail that may have encouraged void burrowing is the excess of Cu provided by the Cu bars attached to the solder. Had the Cu interface instead been a thin metallization layer, the void would have propagated along the Cu interface in a pancake-voiding fashion as it progressively consumed the Cu layer (Hu et al. 2003). With an unlimited Cu supply and lack of current crowding due to sample geometry, the void was free to propagate directly into the Cu bar.

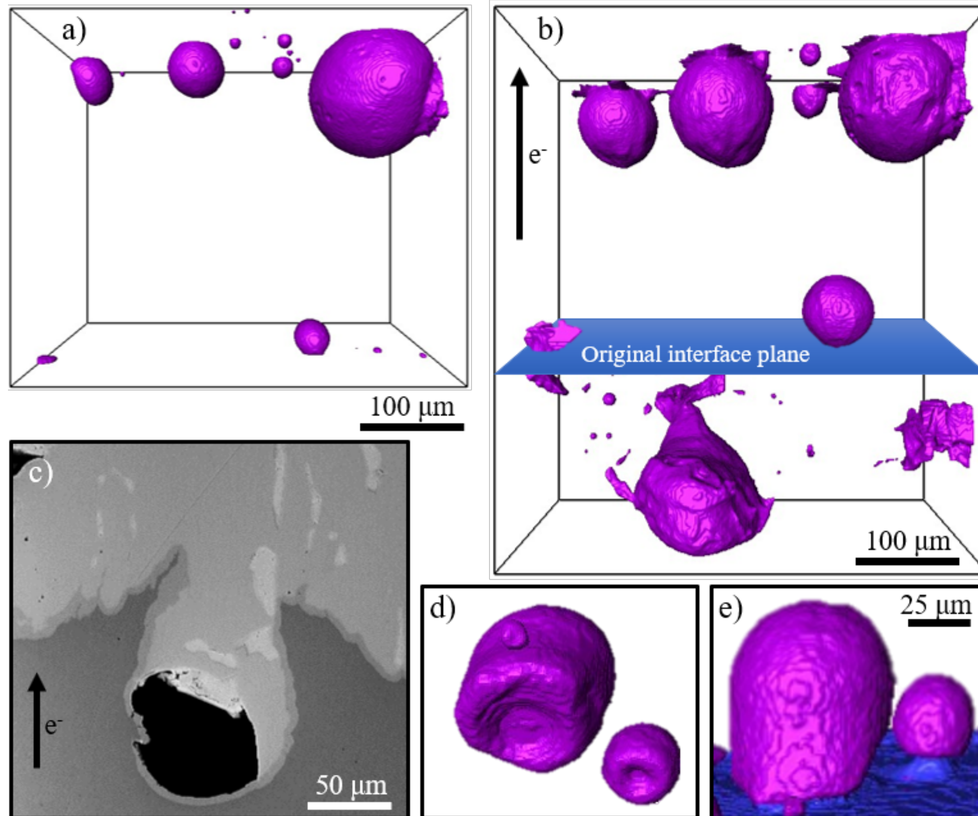

Figure 24. Void burrowing shown by void reconstructions of the faster diffusion sample before and after EM testing (a and b), SEM image of polished sample cross-section showing burrowed void (c), and dimpled bicrystal anode voids showing rapid Cu dissolution around void edge and Cu peak beneath the voids (d and e).

4.4 Summary

The goal of this analysis was to determine how the crystallography of solder affects the evolution of voids present in it upon fabrication. Spherical voids created by entrapped air or outgassing flux are common in as-manufactured solder joints, but their effects on EM deformation and relationship with grain orientation have not been well understood. Characterization of samples before and after testing using x-ray microtomography

provided 3D reconstructions of the void space. In-depth analysis of the surface reconstructions in conjunction with EBSD mapping on surface cross sections before and after testing revealed how and why voids evolved the way they did. We reached the following conclusions.

1. EM-tested solder joint evolution varied significantly between slower diffusion, faster diffusion, and bicrystal samples.
2. Void faceting occurred in the slower diffusion sample and bicrystal cathode due to large θ angles of the grains surrounding the voids which resulted in slow EM-driven diffusion. Faceting is controlled by anisotropic atomic surface diffusion and has not been reported in literature investigating void growth during EM testing.
3. Void burrowing occurred in faster diffusion sample due to rapid EM-driven diffusion, current-crowding at void edges, and unlimited Cu at the anode interface.

This research shows that void evolution is highly affected by the c-axis orientation of the grain surrounding the void as opposed to the overall orientation of the joint, as evidenced by the difference in void behavior at the cathode and anode of the bicrystal sample. Visualization and quantification of void growth and faceting would not have been possible without x-ray microtomography to capture the initial and final 3D structure of the entire joint. Faceting and burrowing behaviors both have implications for the reliability and lifetime of solder joints. Single crystal joints with small θ angles will experience rapid void growth and burrowing, leading to open circuit failure. Single crystal joints with large θ angles could exhibit void faceting. The sharp edges and pointed

corners of the faceted voids would be stress localization sites. As the joint experiences thermomechanical stresses during service, the stress localization sites would be sites for crack initiation. The results of this experiment suggest that bicrystal structures would be best suited for joint stability under EM because the joint would avoid the degree of damage shown by either a slow of fast diffusion grain. This work also reinforces the importance of understanding EM effects as a result of sample geometry, crystallography, and pre-existing structure in concert.

CHAPTER 5

3D EVOLUTION OF INTERMETALLIC AND VOID STRUCTURE UNDER INTERRUPTED ELECTROMIGRATION IN BI-CRYSTAL PURE SN SOLDER JOINT

5.1 Introduction

EM is of particular concern in Sn-rich solders due the anisotropic diffusion properties of the tetragonal β-Sn lattice and rapid diffusion along grain boundaries. Solder joints do not have controlled grain structures and have been shown to solidify in single crystals, six grained "beachball" type structures, and fine-grained interlaced twin structures (Lehman et al. 2010). This means that an individual joints' susceptibility to EM can vary dramatically due to differences in grain structure and prediction of joint lifetime becomes very difficult (Chen et al. 2013; Wilde 2014; Deng et al. 2005). In order to study precisely how EM drives IMC and void formation, researchers have focused on the fastest diffusion pathways for Cu and Sn atoms: the c-axis of the Sn grains and grain boundaries (Tu 2003; Chen & Liang 2007; Dyson, Anthony & Turnbull 1967; Lehman et al. 2010). Research has shown that c-axis orientation affects interfacial IMC growth (Tian et al. 2018, Chen et al. 2013), bulk IMC growth (Deng et al. 2005; Shen & Chen 2017; Lu et al. 2008), void growth (Chen et al. 2013; Deng et al. 2005; Ma et al. 2018) and surface deformation (Kerr & Chawla 2004; Jiang & Chawla 2010). However, investigation into the effect of grain boundaries has been more complex as boundaries vary in atomic structure, which affects the energy barriers for diffusion, and therefore grain boundary diffusivity. Grain boundaries with high misorientation angles are more

disordered, have higher grain boundary energies and therefore faster diffusion. Low angle and twin boundaries have higher order and very low grain boundary diffusivities (Wilde 2014). Grain boundaries also vary in orientation relative to the electron flow and single joint may contain a high density of a large variety of boundaries.

This makes determining the effect of grain boundary type and orientation difficult. One common trend is IMC accumulation along high boundaries regardless of orientation relative to the electron flow (Kerr & Chawla 2004; Jiang & Chawla 2010; Deng et al. 2005; Shen & Chen 2017; Ma et al. 2018; Maruyama 1960), particularly in the case of atoms moving form a fast diffusion grain to a slow diffusion grain (Kerr & Chawla 2004; Deng et al. 2005). Fine IMC particles could act as dislocation and boundary pinning sites like in dispersion strengthened materials (Kerr & Chawla 2004), however particle coarsening over time would result in decreased strength (Deng et al. 2005). Large networks of similarly oriented Cu_6Sn_5 IMC would also be problematic because Cu_6Sn_5 is brittle (Jiang & Chawla 2010) and cleavage along the basal planes of the hexagonal crystals could propagate easily from grain to grain (Jiang, Jiang & Chawla 2012). There is disagreement about the effect of twin boundaries on EM as well. Shen and Chen stated that since Sn solder joints often have a high density of twins and they are not rapid grain boundary diffusion pathways, grain boundary diffusion of Cu was less important than bulk diffusion (Jiang, Jiang & Chawla 2012). While they saw little effect of twin structures, Chen et al. reported IMC buildup along a twin boundary in one case and a significant decrease in EM damage due to a heavily twinned structure in a second case. Findings by Lu et al. support the possibly that highly interlaced twin structures, as sometimes form in Sn-rich solder joints, could slow Cu diffusion by effectively averaging

out any grain orientation effects (Lu et al. 2008). Twins are an inevitable part of Sn-rich solder structures as Sn tends to solidify in a twinned structure (Lehman et al. 2010; Ma et al. 2018) and readily forms twins during mechanical loading (Ishii 1959; Maruyama 1960) and thermomechanical fatigue (Chen, Wang et al. 2012). As such a common yet little understood feature in Sn solders, twins merit investigation as a separate subset of grain boundaries within EM experiments.

Although complex and manifold, understanding the relationships between grain structure and IMC and void growth is key in attempting to mitigate EM damage. To this aim we designed an EM experiment to shed light on these relationships using a bicrystal solder joint composed of a low θ angle grain and a high θ grain, with a clearly identifiable twin network and separate high angle grain boundary. The sample was analyzed using x-ray microtomography at multiple time steps during the experiment in order to capture its microstructural evolution in 3D. Most EM studies focus on post-mortem or 2D surface analysis, however how features formed and how they relate to each other is difficult to trace using those techniques alone. It is important to fully characterize the initial structure of sample in order to understand the structures that develop from it. Chawla and collaborators applied x-ray microtomography analysis to the study of solder joints and demonstrated its ability to capture rapid void and IMC growth (Xie et al. 2014; Bieler et al 2012; Kim & Lu 2006) and crack growth from thermal cycling (Regalado et al. 2019). The best solution for complete characterization is a combination of x-ray microtomography for 3D phase analysis, SEM imaging for surface damage, and EBSD analysis for grain boundary and orientation information. The solder joint structure could be probed at multiple time steps only because x-ray microtomography is nondestructive

and the wealth of quantitative information it yields is unparalleled. The interrupted testing process also added a thermal cycling element that mimics what a joint could experience in service. Using these techniques, surface deformation in the combined context of EM and thermally cycling will be discussed. Multiple types IMC growth will be correlated with both grain orientation and grain boundary structure, and anomalous void growth behavior explained.

5.2 Materials and Experimental Procedure

This experiment was conducted on a sample fabricated in the same fashion as the joints discussed in Chapters 3 and 4. Please refer to Section 3.2 for the complete fabrication procedure, as it is discussed here in brief. Solder joints were fabricated from a larger sandwich-style joint composed of a Sn ribbon 250 μm thick (Indium Corporation, 99.99% purity), placed between two oxygen-free high conductivity (OFHC) Cu pellets (McMaster-Carr, Cu alloy 101), 2 mm thick and 9.5 mm in diameter. The solder stack was reflowed on a standard hot plate in ambient air with a hold of 20 seconds above 232°C and then transferred to a pre-chilled Cu surface to cool at a rate of 3.4°C/second. The solder stack was then cross sectioned, mounted in epoxy, and mechanically polished to an 0.05 μm colloidal silica finish. The fabrication procedure is shown schematically in Figure 25 (a). Polarized light microscope images and EBSD analysis done in a Zeiss Auriga SEM confirmed the presence of large single crystal and bicrystal regions in the solder stack cross section. TSL OIM Data Collection and Analysis software were used to gather the EBSD patterns and create OIM maps.

The solder stack was sectioned into bars that were mechanically polished to their final 300 μm wide by 300 μm thick dimensions to remove surface damage caused by the EDM

sectioning. The front surfaces of the bars were polished to a 0.05 μm colloidal silica finish for SEM and EBSD analysis. EBSD mapping confirmed that several joints contained single crystal and bicrystals and a bicrystal sample was selected. The bicrystal sample chosen for this experiment contained a large fast diffusion grain with a θ angle of 46° and a smaller slow diffusion grain with a θ angle of 71°, with a high angle horizontal grain boundary spanning the width of the joint between them, shown in Figure 25 (b). The large fast diffusion grain also contained several lens-shaped subgrains, slanted at 26°±1° from the length of the bar. The subgrain boundaries had a misorientation of 62°±1° and were identified as {101) twin grain boundaries rotated 62.8° about a common <100] axis, one of two commonly observed twin types in Sn (Chalmers 1935; Tu & Turnbull 1970). In order to highlight the expected difference in diffusion throughout the bicrystal sample, the EBSD map shown in Figure 25 (b) was recolored to show the angle between the c-axis and electron flow, with yellow and green representing smaller θ angles and orange and red representing larger θ angles, shown in Figure 25 (c).

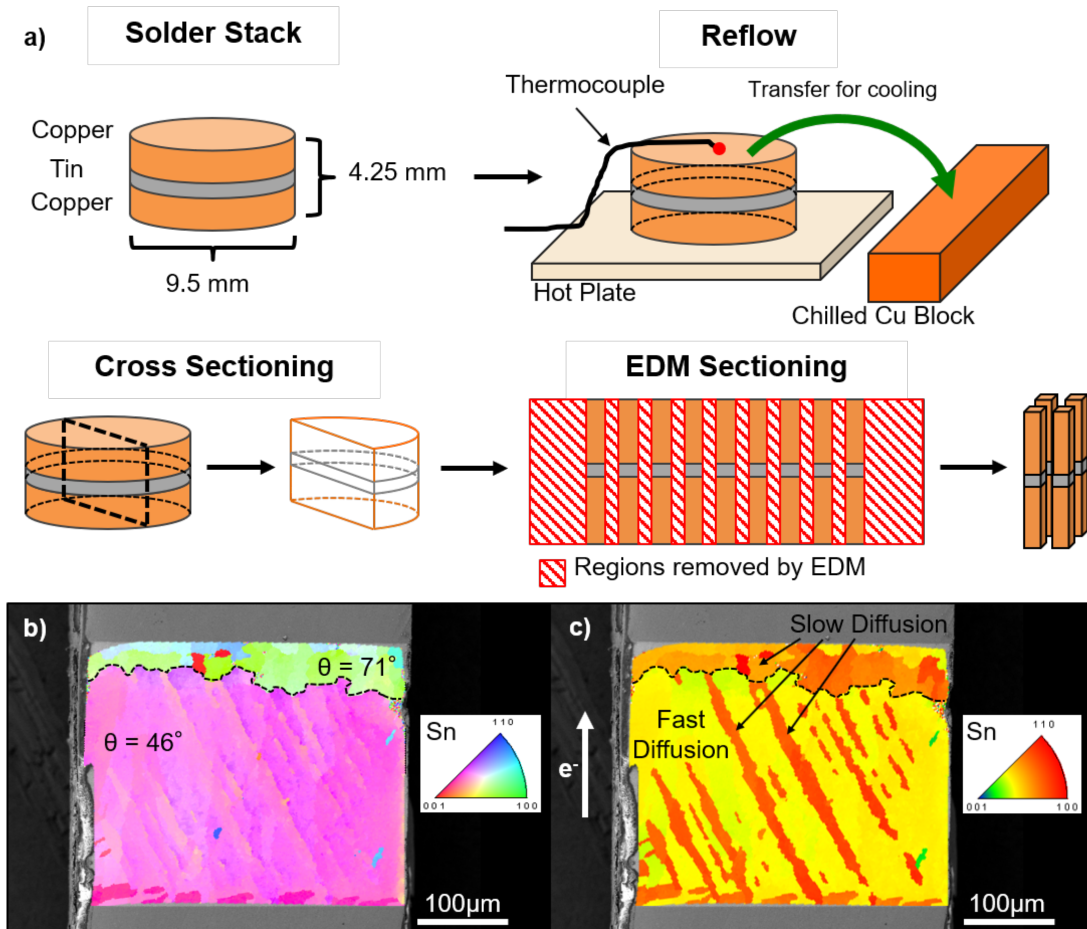

Figure 25. (a) Sample fabrication process from solder stack to individual solder bars. (b) OIM map of the selected bicrystal sample. The sample is composed of a fast diffusion grain (θ angle = 46°) and a slow diffusion grain (θ angle = 71°) with a high angle grain boundary between them (dashed black line). (c) OIM map recolored to show the angle between the c-axis and electron flow (θ angle). Green and yellow indicate small θ angles and fast diffusion and red and orange indicate larger θ angles and slower diffusion. The slanted orange subgrains are twins.

The sample was EM tested at a current density of 1 x 10^4 A/cm^2 for a total of 100 hours with interruptions for lab-scale x-ray microtomography scans (Zeiss 520 Versa).

The test fixture was placed inside a box furnace and kept at 140°C in air to eliminate temperature fluctuations caused by resistive heating. X-ray microtomography scans and SEM imaging were performed at the following timesteps: 0, 12, 25, 50, 75 and 100 hours. The scans were processed in ImageJ (U.S. National Institutes of Health, Bethesda, Maryland, USA) using a combination of nonlocal means, bandpass, and anisotropic 2D diffusion filters to reduce noise (Schneider, Rasband & Eliceiri 2012) and then segmented in Avizo 9 (ThermoFisher Scientific, Waltham, MA, USA) to create 3D volume renderings for analysis and visualization. After the EM test was complete, the sample was mounted in epoxy and polished to a 0.05 μm colloidal silica finish for SEM and EBSD characterization.

5.3 Results and Discussion

5.3.1 Surface Deformation

Significant surface deformation is immediately evident from the SEM surface images shown in Figure 26. The solder section of the joint was originally almost square with a smooth front surface. Over time the sample decreased in height, bulged outwards on its free surfaces, and appeared to slant slightly towards the right. The sample decreased in height by a total of 40 μm by the completion of the EM test. This change in dimension was due to compression of the solder region by the Cu bars on either side. The EM fixture fixed the position of the Cu bars at room temperature and upon being brought to 140°C for testing, the Cu bars expanded and compressed the Sn. The Sn likely work hardened as a result of the compression as it did not return to its original dimensions upon cooling. The sample was then removed from the fixture, scanned for tomography, and replaced in the fixtured in its compressed state. Upon heating the solder would again be

compressed by the Cu bars. The sample experienced a total of 5 heating cycles during the experiment. The linear expansion of the Cu bars due to heating was calculated using the following equation:

$$dl = l_0 \alpha_{Cu} (\Delta T),$$

where dl is the change in length, l_0 is the original length of the bars, α_{Cu} is the linear coefficient of thermal expansion (CTE) of Cu (17 x 10^{-6}/K), and ΔT is the increase in temperature. For each thermal cycle, the Cu bars would have expanded approximately 8 μm inwards. Over the course of 5 thermal cycles, the total compression would be 40 μm which matched the total decrease in solder height.

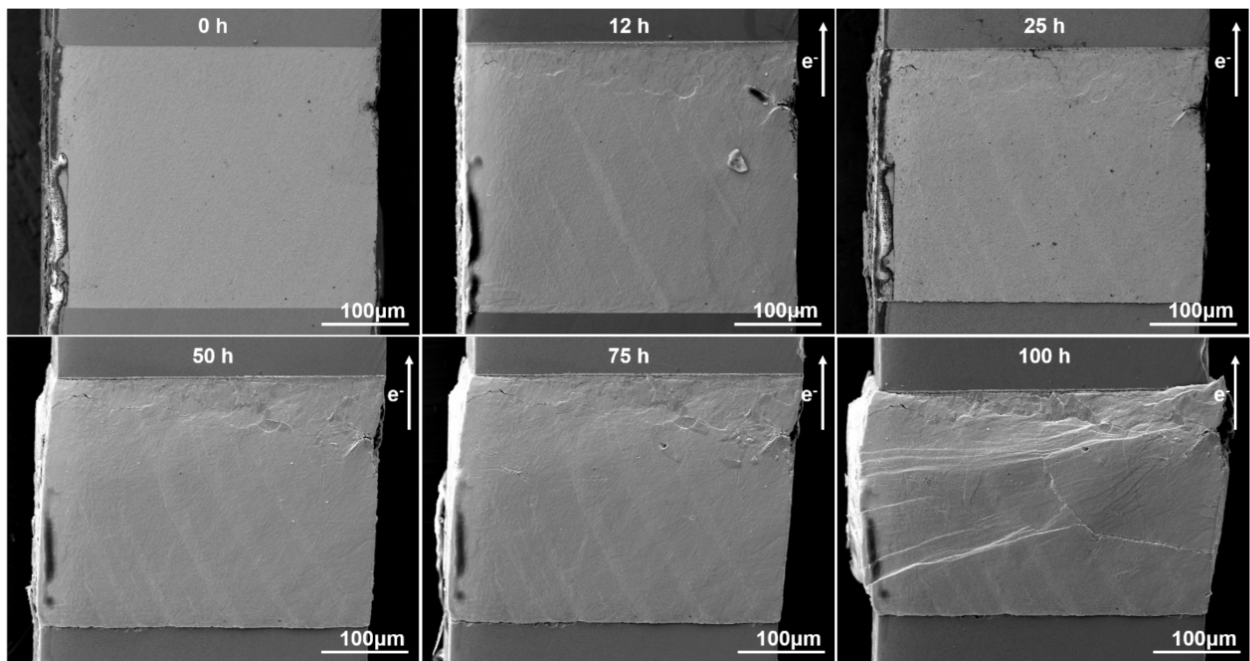

Figure 26. SEM images of sample surface at 0, 12, 25, 50, 75, and 100 hours of EM testing. Compression from thermal expansion caused the sample to bulge and slant to the right.

In addition to the changes in sample dimension, Figures 26 and 27 show grain boundary sliding along the high angle horizontal grain boundary, ledge formation, and IMC particle coarsening in the vicinity of the slow diffusion grain. Grain boundary sliding in a variety of solder alloys as a result of thermomechanical fatigue or thermal cycling has been well documented along both high (Sidhu & Chawla 2008; Ho et al. 2016; Lin et al. 2005; Arzt et al 1994; Telang et al. 2002; Telang et al. 2003; Rosenberg & Ohring 1971) and low angle (Telang, Bieler & Crimp 2006) boundaries. Sliding and decohesion along grain boundaries is caused by the anisotropic CTE properties of β-Sn, where CTE along the c-axis is approximately double that along the a- or b-axes (Ho et al. 2016; Telang et al. 2003). The c-axis orientations of the two grains that compose this solder joint are significantly different, as shown in the initial EBSD analysis in Figure 25 (b) and (c), so it is expected that grain boundary sliding or delamination would occur along this boundary. This type of deformation is a reliability concern as regions that have undergone grain boundary sliding may serve as crack initiation sites (Sidhu & Chawla 2008; Matin & Coenen 2005). Figure 27 (c) clearly shows the formation of a crack on the sample surface that began as grain boundary decohesion. Due to the uneven surface it was difficult to tell how far along the grain boundary length the crack penetrated and it was not resolvable in tomography. No grain boundary sliding or decohesion occurred along the slanted 62.8° twin boundaries, a phenomenon also noted by Telang et al. during their thermomechanical fatigue studies (Telang, Bieler & Crimp 2006).

Surface IMC coarsening, visible in Figure 27 (b), occurred both within the slow diffusion grain and along the grain boundary. High angle grain boundaries like the horizontal boundary in this joint are rapid diffusion pathways and often become

decorated with Cu_6Sn_5 IMC particles during EM testing (Shen & Chen 2017; Maruyama 1960; Bieler et al. 2012). In addition it has been shown that when the electron flow passes through a fast diffusion grain into a slow diffusion grain the grain boundary acts like a wall to Cu diffusion and the entire boundary becomes saturated with IMC (Huang et al. 2016). Once in the slow diffusion grain, Cu atoms will aggregate along subgrain boundaries and form IMC particles as well. The IMC particles visible along the horizontal boundary appeared sunken into the sample surface as opposed to protruding, a phenomena Tian et al (Tian et al. 2018) have suggested is caused a relationship between the c-axis, electron flow direction, and sample surface. If a grain is oriented such that an atom traveling along the c-axis in electron flow direction is deflected inwards towards the sample bulk, then surface IMC particles will appear sunken. If instead the atom gets deflected towards the sample surface, the IMC particles will appear raised. In the slow diffusion grain the diffusing Cu atoms were deflected inwards while in the fast diffusion grain the Cu atoms were deflected outwards. Particles on the slow diffusion grain side of the boundary appeared sunken and particles on the fast diffusion side appeared to be protruding.

While several surface deformations can be attributed to the thermal cycling component of the experiment, one feature of note is clearly caused by EM: the visible consumption of the electron-inflow solder/Cu interface. The interface began planar, as shown in the 12 h section of Figure 28, but over time several scoop-shaped hollows formed as the Cu atoms diffused away from the interface into the solder bulk. The uneven consumption of the interface was caused by interfacial voids within the sample that are very close to the sample surface. Interfacial voids reduced the local cross-sectional area

through which Cu atoms could diffuse which caused a spike in current density in the regions next to the voids. This spike caused Cu atoms to diffuse more rapidly in that region which created the uneven consumption of the Cu interface (Bieler et al. 2012; Han et al. 2012; Mertens, Kirubanandham & Chawla 2015; Subramanian & Lee 2006). The true extent of hollow formation was slightly obscured by bulging of the solder bulk which shadowed the interface.

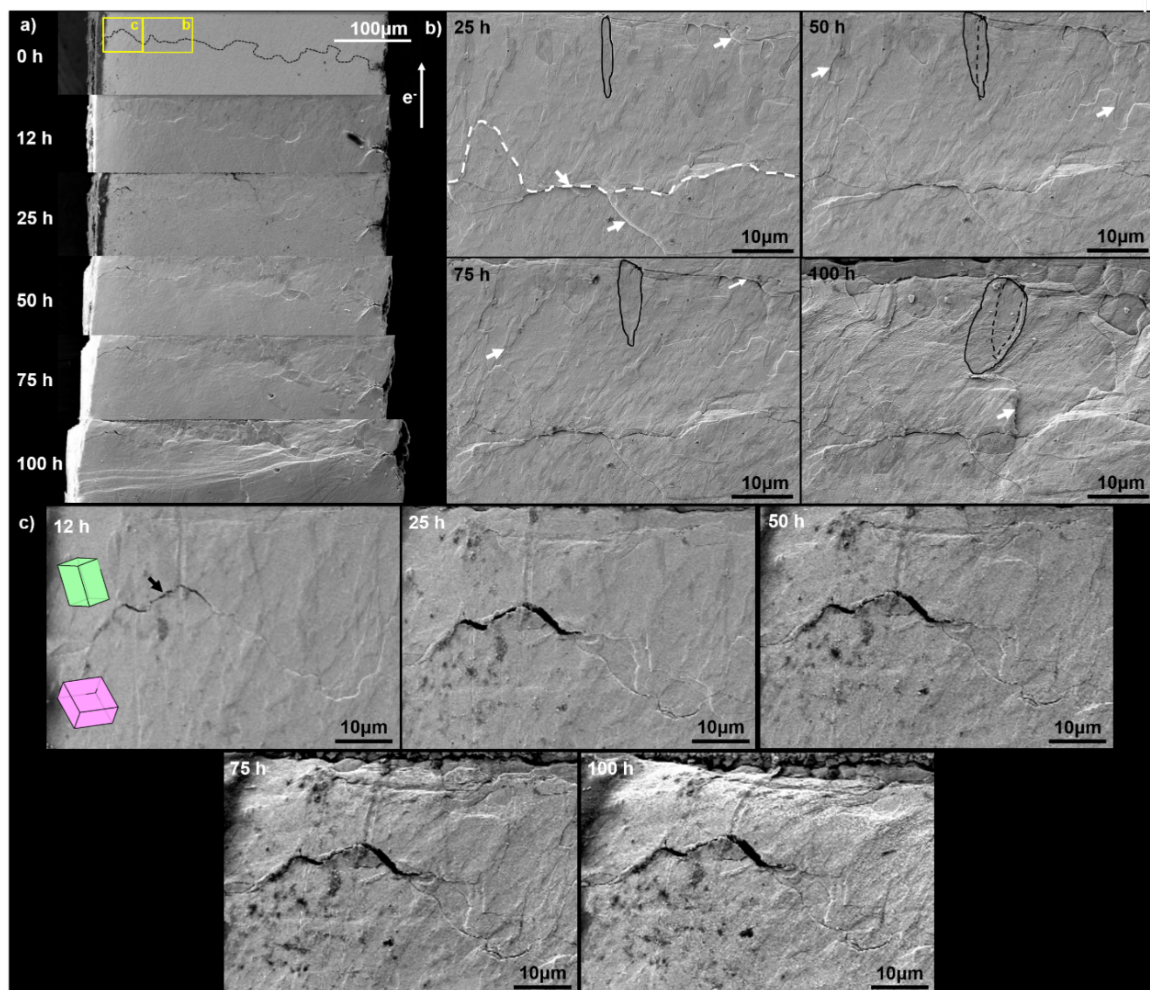

Figure 27. (a) SEM images of the horizontal grain boundary between the fast and slow diffusion grains. (b) Higher resolution SEM images of a section of the grain boundary,

indicated by the yellow box in (a), showing grain boundary sliding, surface ledge formation (white arrows), and surface evidence of IMC particle growth (black solid and dashed lines). (c) Evidence of fatigue crack (black arrow) growth along grain boundary with the slow diffusion Sn lattice shown in green and the fast diffusion Sn lattice shown in pink.

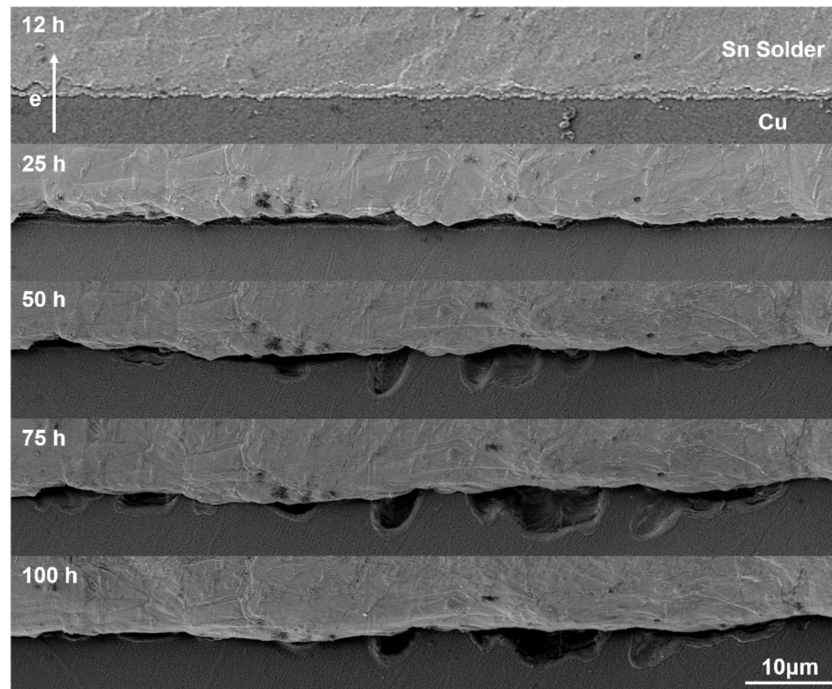

Figure 28. SEM images of a section of the Sn solder/Cu electron-inflow interface showing irregular consumption of the Cu substrate and solder surface bulging over the course of 100 hours of EM testing.

5.3.2 IMC Growth along High Angle and Twin Grain Boundaries

The combination of x-ray microtomography, SEM imaging, and EBSD analysis is uniquely powerful in the investigation of bulk IMC growth. In recent years Chawla and collaborators demonstrated how effective microtomography can be when characterizing

IMC growth (Xie et al. 2014; Kim & Lu 2006), void growth (Xie et al. 2014), and crack propagation (Regalado et al. 2019) in solder joints. In order to capture the evolution of the bulk IMC and elucidate its relationship to the solder grain structure, six tomography scans were conducted, one before testing and the rest over the course for the EM test. Surface reconstructions of the tomography scans are shown in Figure 29 with Sn solder matrix shown in transparent green, voids in blue, and IMC in pink and purple.

Initially the sample did not contain any IMC in the solder bulk and the only visible features were the interfacial voids. At the 12-hour timestep, IMC formed along the horizontal grain boundary and in slanted plates along the twin boundaries initially shown in Figure 25 (d). Figure 29 (a) shows the continued growth of IMC along the grain boundary and in the bulk. We visualized the IMC growth by plotting the total IMC, grain boundary IMC, and bulk IMC over time, shown in Figure 30 (left). The IMC growth at the grain boundary was rapid at first at ~ 2 μm^3/sec, not far behind the ~3.9 μm^3/sec growth rate of the bulk of the joint where the majority of IMC was developing. After 25 hours the grain boundary IMC growth decreased to ~0.4 μm^3/sec while the bulk IMC growth continued at ~3 μm^3/sec. Over the course of 100 hours IMC in the bulk grew 5.5 times faster than IMC along the high angle grain boundary. It is possible that Cu atoms were reacting in the bulk to form IMC before they reached the grain boundary and as more IMC developed in the bulk, the more barriers there were to Cu diffusion to the grain boundary, slowing its growth even further. In essence, the IMC network in the low θ angle grain was shadowing the boundary, making Cu diffusion to the horizontal grain boundary very difficult.

The rapid bulk IMC growth was particularly interesting as it appeared to change orientation over time. In order to investigate this further, the bulk IMC surface was rendered in two colors, pink for the initial orientation and purple for the secondary orientation that develops from the first. Figure 29 (b) and (c) show that while the initial IMC growth aligned with the slanted twins, a second set of plate-like IMC began to form at 25 hours with a different alignment. By plotting the growth of the primary and secondary IMCs in Figure 30 (right) it is clear that not only did the secondary IMC grow out of the primary IMC, it grew at the expense of the primary IMC. While the twins in the low θ angle grain were not high energy, disordered boundaries one would expect to become saturated with IMC, they did represent a significant deviation in diffusion from the rest of the grain. Instead of diffusing along a grain boundary, Cu atom flux from the low θ angle grain hit the slanted twin boundaries like walls. The c-axis orientation of the twin subgrains was 76° off from the electron flow, making the subgrains even slower diffusion than the slow diffusion grain at the top of the joint, with a θ angle of 71°. The twin boundaries were the only significant barrier to Cu diffusion in the low θ angle grain so IMC built up along them, which was why the IMC structures seen in tomography precisely match the twin structures. Around 25 hours into the EM testing, IMC along the twins visible in the initial sample EBSD map began to decay and the secondary IMC visible starting in the 25-hour tomography scan began to coarsen. The initial growth rate of each IMC was taken and compared, 0-hour to 12-hour growth for the primary IMC and 25-hour to 50-hour growth for the secondary IMC. Their initial growth rates were nearly identical, at ~7 μm^3/sec. In the second half of the EM test, the secondary IMC growth rate slowed to ~3.5 μm^3/sec, while the primary IMC began to shrink. The secondary IMC

also appeared to be forming on a specific orientation, similar to the primary IMC, but at a different angle. The similarity in initial growth rate and structure suggested that the secondary IMC was associated with a second twin orientation.

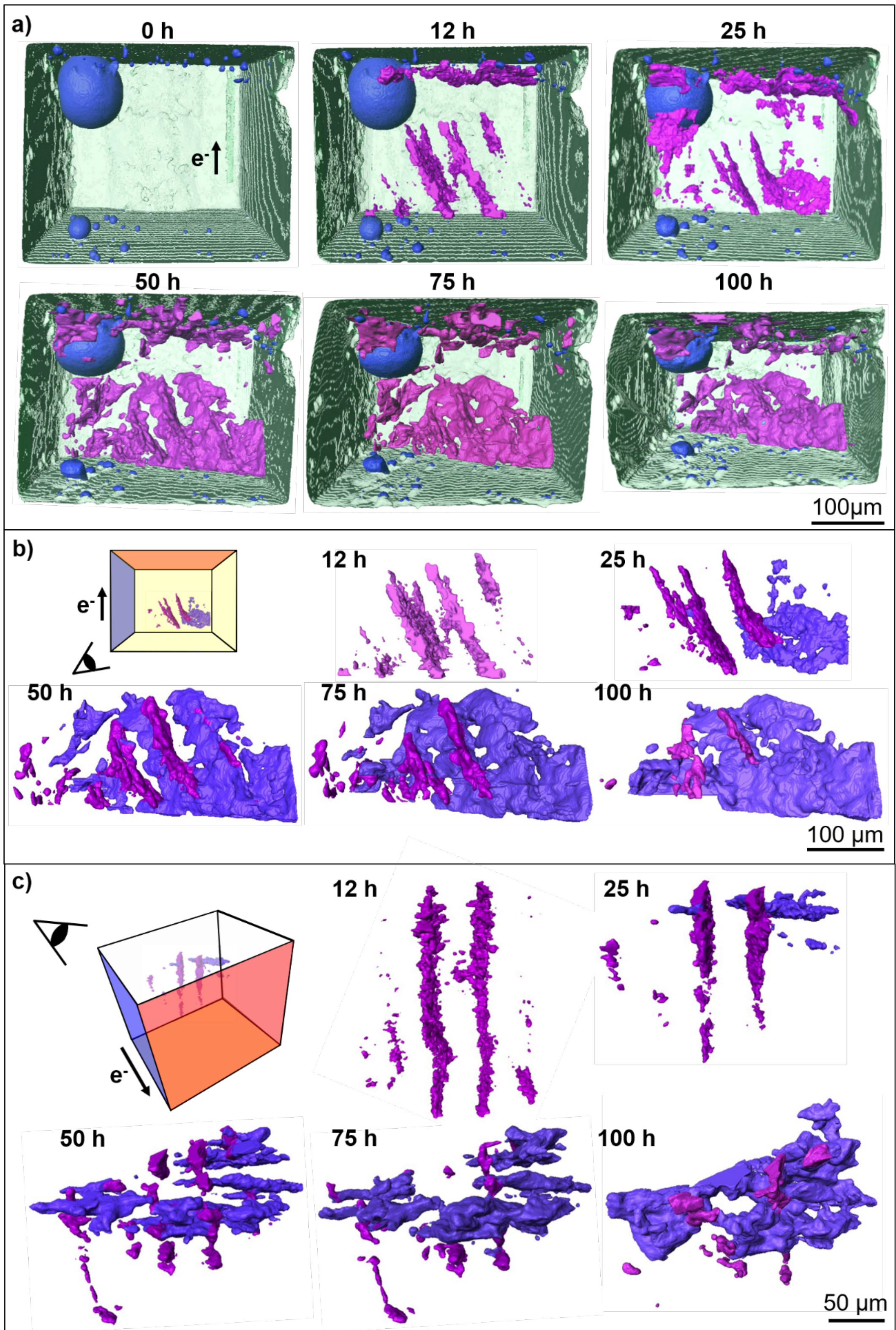
a)
0 h
12 h
25 h
e⁻
50 h
75 h
100 h
100μm
b)
e⁻
12 h
25 h
50 h
75 h
100 h
100 μm
c)
12 h
25 h
e⁻
50 h
75 h
100 h
50 μm

Figure 29. (a) X-ray microtomography surface reconstructions of sample at 0, 12, 25, 50, 75, and 100-hour timesteps, with Sn solder in transparent green, voids in blue, and IMC in pink. (b) Surface reconstructions of IMC not associated with the horizontal boundary, showing primary formation of IMC along slanted twin boundaries (pink), followed by secondary IMC growth (purple) and reduction of the primary IMC. (c) IMC from (b) viewed at a diagonal angle to show the difference in alignment between the primary and secondary IMC growth.

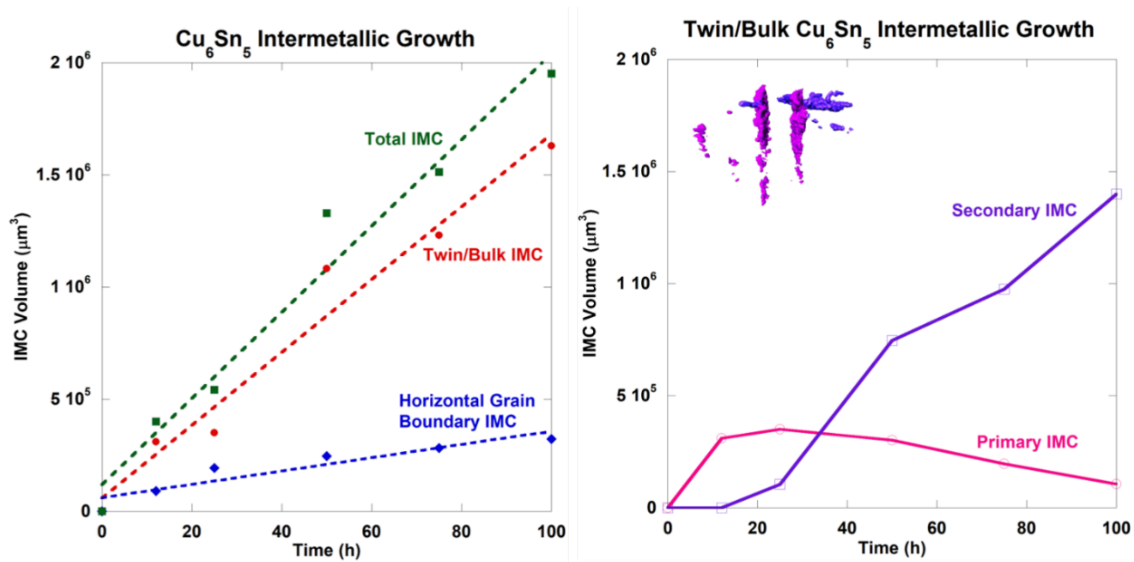

Figure 30. (left) Cu_6Sn_5 IMC growth over 100 hours of EM testing, with total IMC growth in green, IMC associated with horizontal grain boundary in blue, and twin/bulk IMC in red. The majority of IMC growth occurred in the twin/bulk region of the sample. (right) Separation of twin/bulk IMC growth into primary and secondary IMC types, shown in inset.

In order to determine the grain structure the secondary IMC was related to, the sample was repolished to reveal a cross section which contained the second IMC and EBSD mapped to characterize the surrounding grain structure. Figure 31 (a) shows the plane the sample was repolished to, confirming that it contains the secondary IMC network, and Figure 31 (b) shows the large IMC regions in the solder bulk as well as evidence of the uneven Cu interface consumption suggested in Figure 28. The initial IMC formed along the 62.8° twin boundaries, marked in black on the EBSD maps in Figure 31 (c), which gave the IMC its distinctive slanted-plate character. The EBSD map of the repolished section revealed that the sample recrystallized, maintaining only a few regions with grain orientations similar to the starting orientations. There was no evidence that the original twin structure had been preserved, however a new network of twins with the same 62.8° misorientation was discovered. This new twin network appeared to be at an angle, slanting through the sample cross section much like the secondary IMC. No other set of grains in the repolished cross section appeared to be connected or have a grain boundary structure that extended across the joint, as would be required for boundaries associated with the secondary IMC. It was hypothesized that the grain structure of the joint was maintained for the first 12-hour timestep of EM testing, but the joint recrystallized in later timesteps. Multiple thermal cycles deformed the bulk of the joint which caused it to recrystallize and form randomly oriented grains and a second set of twins. This type of 62.8° twinning is common in Sn and forms both during solidification (Lehman et al. 2010; Ma et al. 2018; Bieler et al. 2012) and thermomechanical fatigue (Sidhu & Chawla 2008; Chen et al. 2015; Terashima et al. 2009; Lee & Stone 1994; Matin, Vellinga & Geers 2006) so it is not unexpected. However, because the secondary

IMC formed with a distinct orientation it was suspected that the secondary twin network formed before the majority of the randomly oriented recrystallized grains formed, otherwise the other recrystallized grains would have disrupted the twin network and the secondary IMC would have formed more randomly.

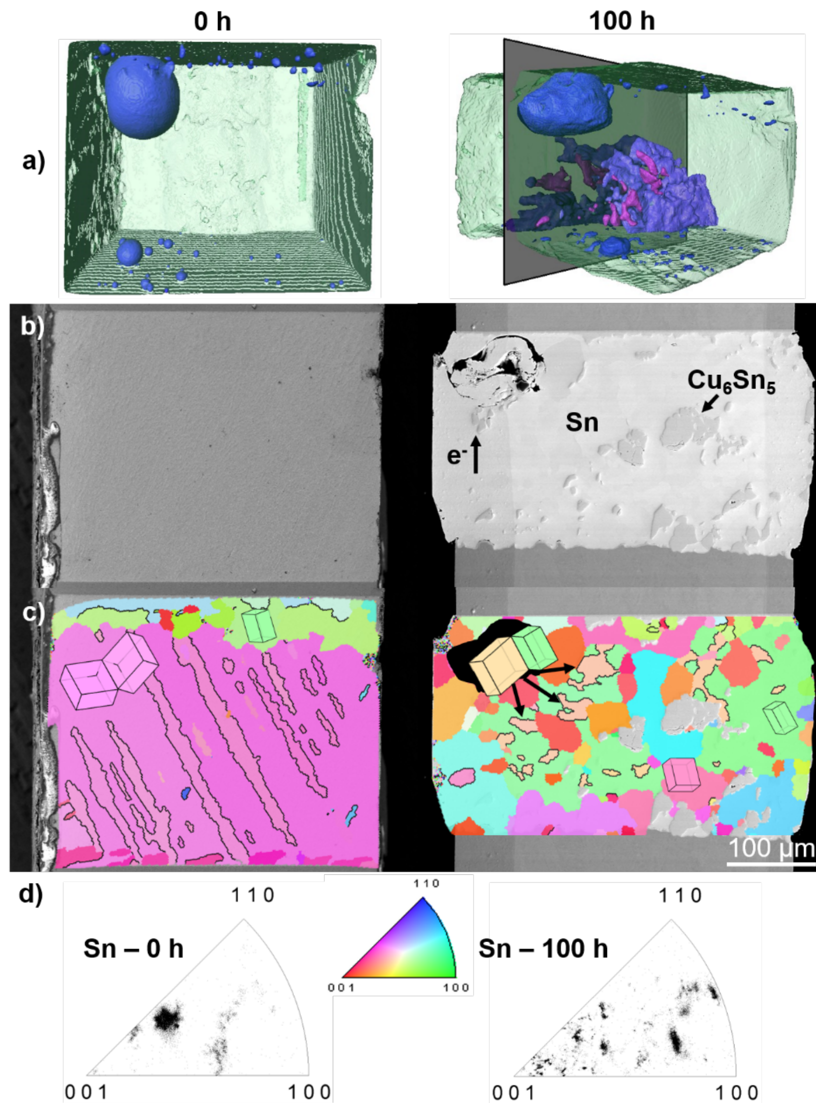

Figure 31. (a) Surface reconstructions of 0-hour and 100-hour timesteps with Sn (transparent green), voids (blue) and IMC (pink and purple). Grey rectangle on 100-hour reconstruction shows the location of post-testing polished sample surface. (b) SEM images of sample at (left) 0 hours and (right) after 100 hours of testing. 100-hour sample was repolished to show internal structure. (c) OIM maps of surfaces shown in (b) with {101) twin grain boundaries (misorientation of 62.8° about a common <100] axis) marked in black and β-Sn tetragonal crystal lattices of major orientations overlaid. The 0-hour map shows twins extending into sample depth while the 100-hour map shows a second set of {101) twin grain boundaries on a different orientation. (d) Inverse pole figures (IPFs) of OIM maps in (c).

5.3.3. Void Evolution

As mentioned in Section 4.3.2, x-ray microtomography has also been used to investigate void formation and growth during EM testing of various solder alloys (Xie et al. 2014; Bieler et al. 2012; Han et al. 2012; Matin, Vellinga & Geers 2007). Figure 32 (a) shows the surface reconstructions of the voids and sections (b) and (c) plot the total void volume and number of voids at each interface over time. The largest void was left out of the volume and number plots as it would drown out all the other voids and make trends difficult to visualize. Typically, a sample undergoing EM would experience an increase in void growth at the electron-inflow interface due to the migration of Sn and Cu atoms away from the interface and no voiding or void shrinkage at the electron-outflow interface. Our sample deviated from this expected behavior in that both interfaces experienced void shrinkage. One possible explanation for this was that thermal cycling

compressed the voids, collapsing voids that would otherwise have contributed to the total volume and void growth calculations. In order to test this theory, the largest and therefore easiest to visualize void was isolated and its height was measured over time, as shown in Figure 32 (d). The largest electron-outflow void decreased approximately 40 μm in height, matching the 40 μm compression of the solder bulk from section 4.3.1, and the largest electron-inflow void decrease approximately 20 μm in height. Another supporting feature was that neither void changed in width or depth, indicating that the force compressing the voids was uniaxial and acted along the length of the solder joint. This result suggested that thermal cycling effects may have obscured or limited void growth typically expected of EM tested samples.

In contrast to many papers discussing EM voiding, the voids in this sample did not propagate in a pancake-void (Bieler et al. 2012; Mertens, Kirubanandham & Chawla 2015; Borgesen et al. 2018; Chang et al. 2017; Lee et al. 2011) fashion, instead they remained mostly spherical or broke into smaller subvoids. The phenomena of a single void breaking into subvoids has been little discussed in EM literature, likely because without 3D nondestructive analysis techniques it is impossible to know how voids in the final structure related to the initial structure. Void splitting has been suggested in simulation literature with little experimental validation (Kim & Lu 2006; Averbuch, Israeli & Ravve 2003). With x-ray microtomography it was possible to track the evolution of a single void and therefore capture a void breaking into subvoids, as occurred at the electron-inflow interface. The following physical description of the void splitting process was suggested by the analysis of the void surface renderings and the repolished cross section of the sample after testing. First, a spherical void was present at

the planar Sn/Cu interface. Due to the current-crowding zone around the edge of the void, Cu diffusion occurred rapidly, consuming the Cu interface around the perimeter of the void. The void increased in size due to the accumulation of vacancies that resulted from the Sn and Cu diffusion, but it did not remain spherical due to the uneven consumption of the Cu interface. Instead, the base of the void grew into the divots left behind by the diffusing Cu. Viewed in cross section the void was now a hemisphere with lobes on each side. If this void were compressed along its vertical axis the main hemisphere would disappear and the void regions in the divots of the Cu interface would be pinched off from one another. This is evolution is shown schematically in Figure 33. The net result of this process would be a decrease in total void volume, but a dramatic increase in void number. This trend is shown in the plot in Figure 32 (c) where the number of voids doubled between the 75-hour and 100-hour timesteps and the total void volume decreased. In contrast, the opposite Sn/Cu interface remained planar and saw a linear decrease in void volume and void number as voids were filled in by interfacial IMC growth or collapsed by thermal cycling-induced compression.

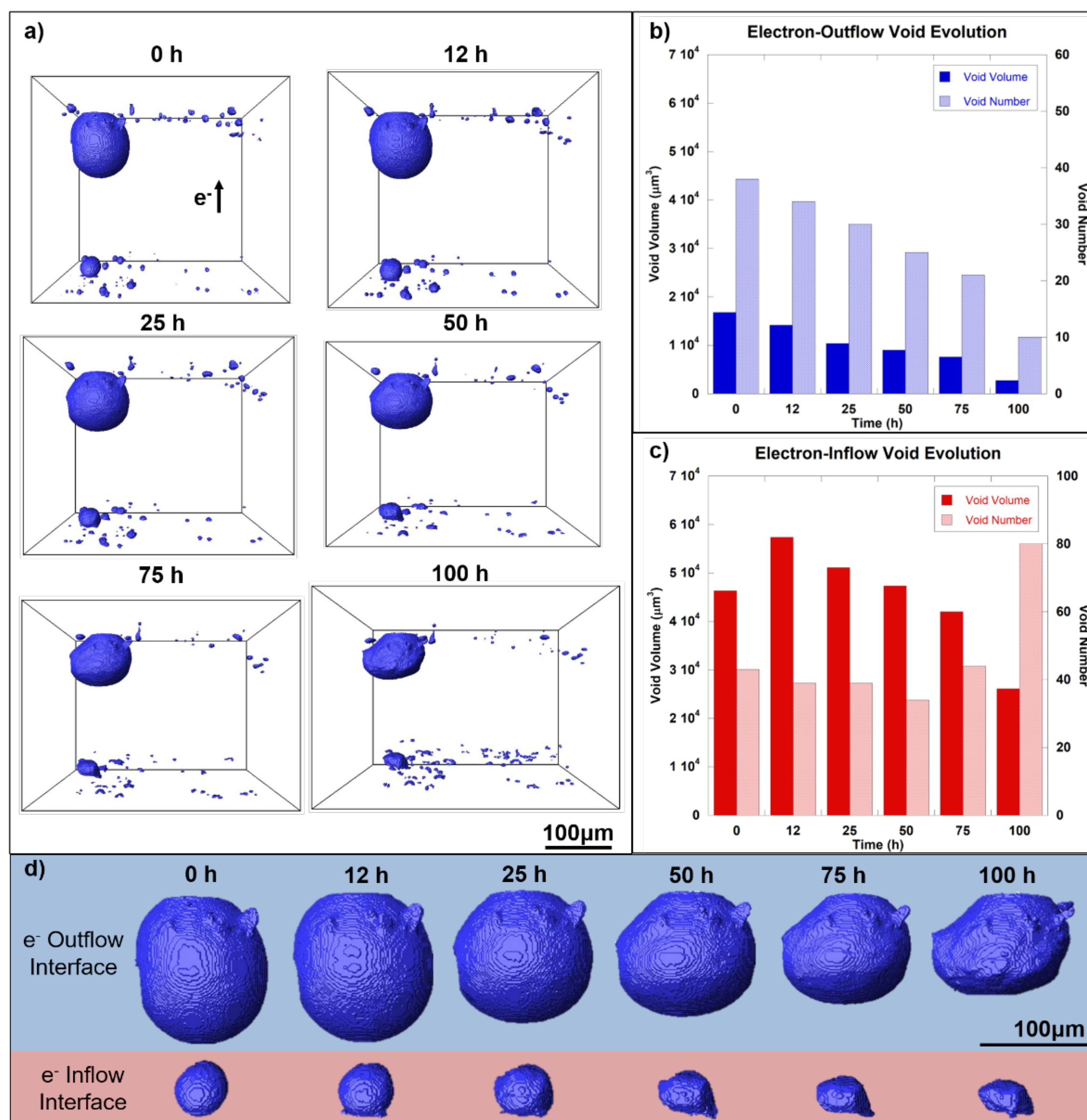

Figure 32. (a) Surface reconstructions of voids at 0, 12, 25, 50, 75, and 100-hour timesteps. (b) Void growth and void number change for voids along the electron-outflow interface, excluding the largest void. (c) Void growth and void number change for voids along the electron-inflow interface. (d) Surface reconstructions of the largest void at the interface, showing compression in the vertical dimension over time.

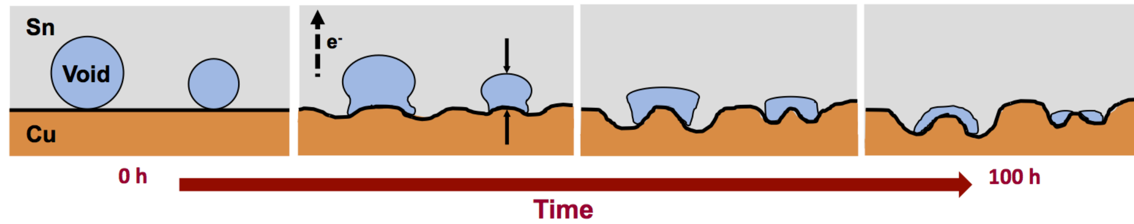

Figure 33. Schematic representation of void splitting over time as a result of uneven consumption of the electron outflow Cu interface and solder compression due to thermal expansion of Cu substrate bars. Electron flow is indicated with a dashed arrow and thermal compression along the length of the solder joint is indicated with solid black arrows.

5.4 Summary

In this study, the evolution of surface damage, IMC growth, and void growth driven by EM was characterized in the context of a bicrystal solder joint composed of a large fast diffusion grain with a preexisting twin network and a smaller slow diffusion grain. Interrupted testing created a second experimental component, thermal cycling, the effects of which were discussed. 3D x-ray microtomography was used to quantify and visualize the Sn solder matrix, grain boundary and bulk IMC, and voids. SEM and EBSD characterization linked grain orientation and structure to the evolution of surface damage, IMC growth, and void growth. The following conclusions were drawn.

1. The thermal cycling caused grain boundary sliding along the high angle horizontal grain boundary between the fast and slow diffusion grains due to the mismatch in c-axis orientation between the two grains. Evidence of fatigue crack formation resulting from grain boundary decohesion was found and a

compression of 40 μm was determined due to the repeated CTE of Cu bars connected to the solder.

2. Visible surface features resulting from EM included protrusion and sink-in of surface IMC particles in the slow diffusion grain and in the vicinity of the high angle grain boundary.
3. X-ray microtomography revealed IMC growth in two distinct regions in the solder joint: along the twin boundaries in the bulk of the fast diffusion grain and along the horizontal grain boundary. IMC growth along the horizontal grain boundary was initially close to that in the bulk region of the solder, ~2 μm^3/sec and ~3.9 μm^3/sec respectively, but after 25 hours the grain boundary IMC growth decreased to ~0.4 μm^3/sec while the bulk IMC growth continued at ~3 μm^3/sec. It is possible that as the IMC network forming in the bulk coarsened, it prevented Cu atoms from reaching the horizontal grain boundary, therefore limiting the growth of IMC in that location.
4. IMC growth in the bulk of the fast diffusion grain was shown to develop in two distinct orientations. The primary orientation resulted from IMC pile up at the slanted twin boundaries due to a large increase in the angle between the c-axis and electron flow. The IMC grew along the twins, but that structure began to decay and at 25 hours a secondary IMC structure was forming with a different orientation. The two IMC networks both initially grew at a rate of ~7 μm^3/sec with clearly defined linear orientations. EBSD analysis of a cross section within the solder revealed recrystallization and the formation of a second twin network in the same region as the secondary IMC. It is suspected

that both IMC structures took their orientations from the twin networks present in the joint.

5. Unlike most EM studies, voids at both electron-inflow and electron-outflow interfaces shrank. Void growth was likely suppressed and overshadowed by the compression resulting from thermal cycling of the joint, as the largest pores at both interfaces showed signs of compression along the length of the joint.
6. Uneven consumption of the electron-inflow Cu interface due to current-crowding around interfacial voids created divots in the interface that caused interfacial voids to develop irregular structures. Upon compression from thermal cycling the voids broke into many smaller subvoids, characterized by an overall decrease in void volume at an interface in conjunction with an increase in void number.

Although the sample selected for testing had a simple, bicrystal structure with two major grain orientations and two major types of grain boundaries, the IMC evolution revealed in this study is complex, with growth and decay of various orientations in the short testing time of 100 hours. Without x-ray microtomography, it would have been impossible to observe and track the microstructural changes this joint underwent. This work highlights the importance of 3D characterization in conjunction with 2D analysis techniques and its ability to link phase morphology with grain structure. Both grain orientation and grain boundary character were important in understanding how and where IMC growth occurred, in particular the unique plate-like patterning of IMC formed along the twin networks. The formation of large, regular IMC structures as opposed to random

IMC particles or needles will impact how solder joints deform and should be investigated further. The unusual void shrinkage noted at both interfaces could shed light on how compressive stresses could reduce void growth normally accelerated by EM.

CHAPTER 6

THERMAL AGING AND ELECTROMIGRATION EFFECTS IN INDIUM-CONTAINING TIN-RICH SOLDERS

6.1 Introduction

In-containing alloys have gained popularity as a possible replacement for conventional Sn-Ag-Cu solders because of their low melting temperatures (Shalaby 2015; Kanlayasiri, Mongkolwongrojn & Ariga 2009; Sommadossi & Fernandez Guillermet 2007; Tian et al. 2018; Li et al. 2014), high shear and bending strengths (Wang, Yuan & Luo 2012; Tian et al. 2017), greater hardness (Shalaby 2015; Kanlayasiri, Mongkolwongrojn & Ariga 2009), greater creep resistance (Shalaby 2015; Vianco et al. 2007), and interfacial IMC suppression (Tian et al. 2017; Kanlayasiri & Sukpimai 2016). Additions of In to Sn-Cu, Sn-Ag, and Sn-Ag-Bi solders showed the improved behaviors listed above, but the precise mechanism behind how In causes these changes is not well understood. It has been shown that in eutectic Sn-In, In segregates to the electron inflow interface under EM due to the back stress created by the Sn atoms migrating in the direction of the electron flow (Daghfal & Shang 2007; Li et al. 2016). However, at lower concentrations In no longer segregates, but instead forms IMC compounds such as $Cu_6(Sn, In)_5$ and $Cu_3(Sn, In)$ that are both at the solder/pad interfaces and throughout the bulk of the joint (Shalaby 2015; Wang, Yuan & Luo 2012; Tian et al. 2017; Lee, Kim & Suganuma 2011; Daghfal & Shang 2007). At the interfaces, In additions have been shown to suppress the formation of Cu_3Sn (Tian et al. 2017; Kanlayasiri & Sukpimai 2016) during thermal aging, while bulk IMC particles may impede Cu diffusion along grain boundaries (Lee, Kim & Suganuma 2011). In additions have also been seen to

cause grain refinement, which slows interstitial Cu diffusion because a randomized grain texture ensures that no large grains will dominate the diffusion behavior of the joint (Lee, Kim & Suganuma 2011). In additions have even been investigated as a possible solution to Sn whiskering by reducing the strength of the surface Sn oxide, reducing the hydrostatic pressure that drives whisker extrusion (Mahapatra et al. 2017). SnCuIn solder alloys are evidently attractive candidates for use in microelectronic devices, but their microstructure is not well understood. Simulations of SnCuIn alloys have presented the possibility of many binary phases and a ternary phase making characterization a complex task (Kao 1997; Liu et al. 2001; Bahari et al. 2003; Lin et al. 2009). A variety of fabrication techniques has also made In trends difficult to identify. For example, a 2015 study by Shalaby reported a refined IMC structure and high hardness and Youngs modulus values for a SnCu alloy modified with In, processed by melt spinning. The extremely rapid cooling rate of the fabrication procedure could also have produced a fine IMC structure and the effect of In is unclear. Studies vary in reflow time from 60 seconds (Lee, Kim & Suganuma 2011) to ten minutes (Tian et al. 2018), making comparisons in IMC formation impossible as a long reflow time will saturate Sn solder with Cu_6Sn_5 IMC particles. To further complicate matters, In is soluble in Cu_3Sn and Cu_6Sn_5 but difficult to detect using EDS due to the energy overlap between Sn and In so reports showing EDS results cannot be trusted. Finally, most In-containing solder studies focus on thermal aging or EM, not a combination although EM does have a thermal component. An in-depth understanding of how In impacts IMC formation and microstructure under both EM and thermal aging would be critical in refining these alloys for commercial application.

6.2 Materials and Experimental Procedures

Solder joints were fabricated by reflowing solder paste deposited between two Cu wires (5N purity, ESPI Metals) 250 μm in diameter. Joints were reflowed in pairs, one joint containing Sn-0.7wt%Cu solder paste (provided by collaborators from Intel Corporation) and the other containing Sn-0.7wt%Cu-<1.0wt%In (provided by collaborators from Intel Corporation), on a hot plate according to the profile shown in Figure 34.

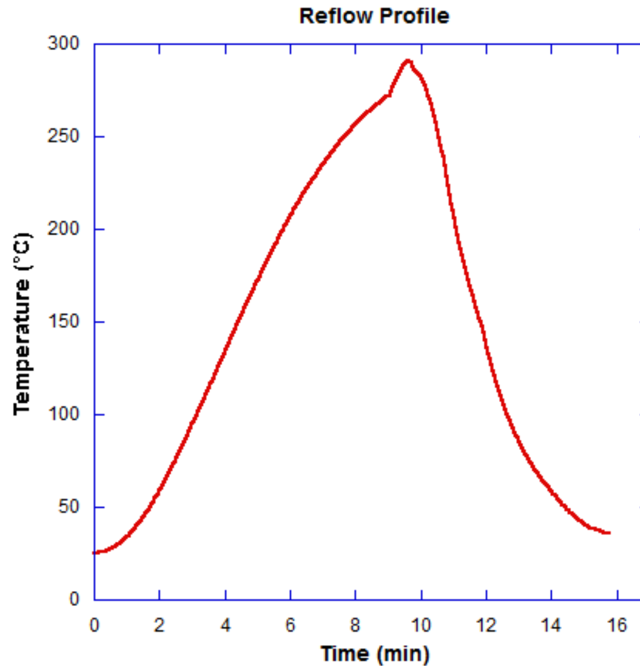

Figure 34. Reflow profile for SnCu and SnCuIn solder joint pairs.

Nine sets of solder joints were fabricated, three for each of the following experimental conditions: EM, thermal aging at 160°C, and thermal aging at 200°C. Each test was conducted for three time increments: 24, 96, and 200 hours. EM testing was done at a current density of $1x10^4$ A/cm^2 and both thermal aging conditions had a variation of 2°C. All three tests were conducted in an insulated box furnace to reduce temperature

fluctuations. The EM test temperature varied between 160°C and 200°C without application of a background temperature from the furnace, likely due to resistive heating from the testing set up.

After testing for 24, 96, and 200 hours the solder joints were removed from the testing fixture, mounted in epoxy and polished to an 0.05 μm colloidal silica finish for SEM analysis (Zeiss Auriga FIB-SEM). Interfacial IMC thickness was determined by selecting a 45 μm long section of IMC from the center of the Cu interface, calculating the area of IMC and dividing the area by the length of the region. Image analysis for IMC calculation was done in ImageJ (U.S. National Institutes of Health, Bethesda, Maryland, USA). Interfacial IMC thickness developed from EM and thermal aging of both solder alloys was quantified and compared. EDS was done to identify In-containing regions for further analysis, however the characteristic x-ray emission lines of Sn and In are very similar making a small concentration of In difficult to detect in a Sn matrix. A possible In-cluster was located in the 200-hour EM-tested joint and subjected to wave-dispersive x-ray spectroscopy (WDS) to confirm the presence of In. Once the region was confirmed to contain In, a transmission electron microscope (TEM) lamella was prepared from the site. The lamella was analyzed in TEM to determine the structure of the In-containing region and how it related to the solder matrix.

6.3 Results and Discussion

Polished cross sections of the nine SnCu and nine SnCuIn solder joints were compared after testing to determine if and how the In addition had affected the solder microstructure. Figure 35 shows the SnCu set and Figure 36 shows the SnCuIn set. Upon inspection the following trends become clear: the electron inflow interface or left side of

the joint has a thinner IMC layer, the electron outflow interface or right side of the joint has a thicker IMC layer with a very irregular scalloped surface, and finally the joint width varies between 150 µm and 90 µm. The thinner and thicker interfacial IMC layers at the left and right sides of the joint, respectively, are formed during reflow as evidenced by as fabricated joints and are not a result of testing. The method of preparation relied on alignment of two 250 µm Cu wires by hand and this led to the variability in joint width visible in the SEM images. The cross sections were analyzed using EBSD to determine grain size, grain orientation, and grain boundary density. There was no detectable difference in grain structure between the SnCu and SnCuIn joints, or across testing conditions. This is contrast to Lee et al's 2011 findings that In addition resulted in refinement in grain structure. However, at the low concentration used in this experiment (<1wt% In) it is possible that grain refinement would not occur, as Lee et al used alloys with 4wt% In and greater. Studies using solder alloys with lower In concentrations have not commented on grain size (Shalaby 2015; Kanlayasiri, Mongkolwongrojn & Ariga 2009; Kanlayasiri & Sukpimai 2016).

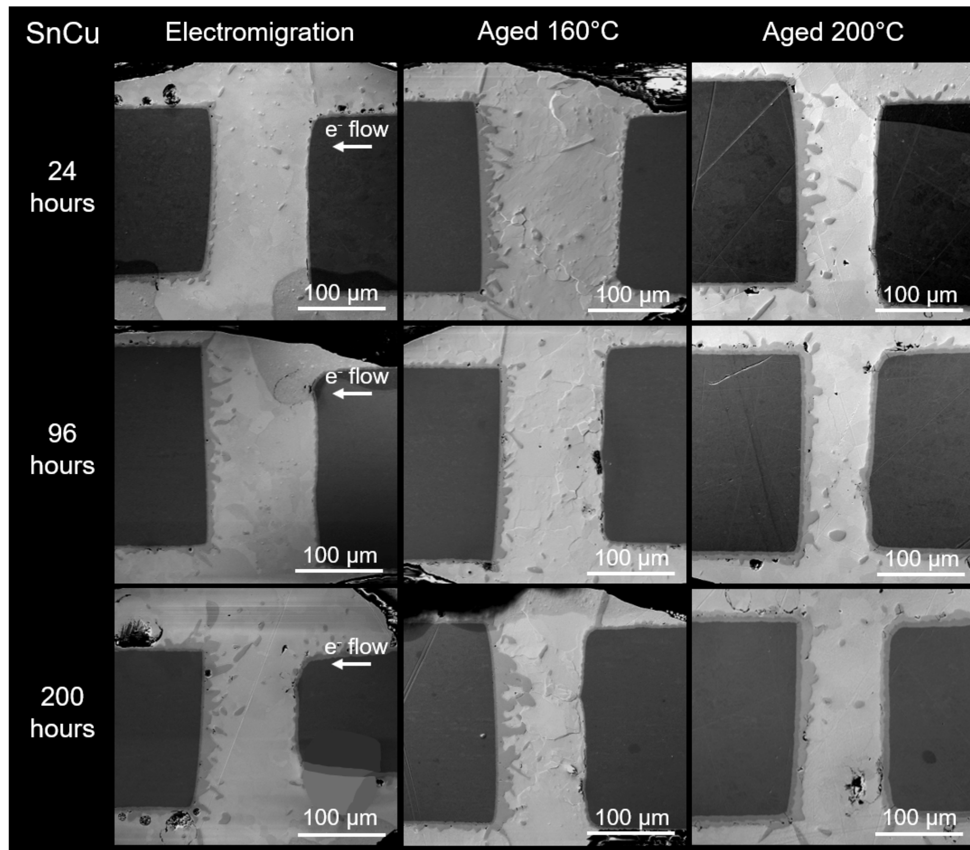

Figure 35. SEM images of SnCu solder joint cross sections, polished after testing.

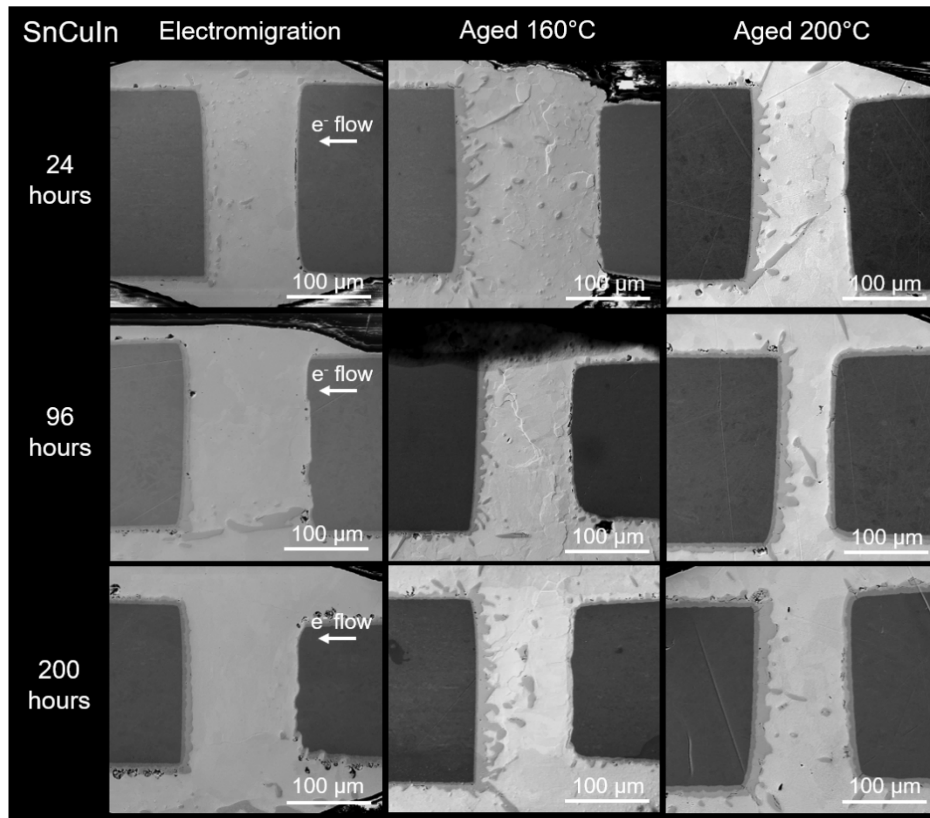

Figure 36. SEM images of SnCuIn solder joint cross sections, polished after testing.

The irregular Cu_6Sn_5 IMC layers formed upon reflow and testing of the majority of the joints were not present in the SnCuIn EM-tested samples, as shown by the interfacial SEM images in Figure 37. Visual inspection shows that after 200 hours, the In-containing sample had planar IMC layers at both electron inflow and outflow interfaces, while the SnCu sample still exhibited a scalloped morphology at both interfaces. The SnCuIn sample had a very thin electron inflow interface IMC compared to the SnCu sample, where significant Cu_3Sn growth was seen. In order to investigate the effect of the In addition on IMC growth, the total IMC thickness, Cu_6Sn_5 IMC thickness, and Cu_3Sn IMC thickness over time were plotted for each composition. The electron inflow IMC interface

growth is shown in Figure 38 and the outflow interface growth is shown in Figure 39. At the electron inflow interface, Sn and Cu atoms are driven away and initial interfacial IMC layers dissolve. If an interfacial IMC layer is present after EM-testing it is typically very thin. The SnCu sample had a thin IMC layer at the inflow interface, but the SnCuIn sample had a thinner IMC layer consistently across the three testing time steps. Figure 38 shows that both IMC phases decreased in thickness in the SnCuIn sample, while the SnCu sample exhibited consistent growth of both. This is in contrast with the electron outflow interface, where both solder alloys exhibited overall growth although the SnCuIn samples grew more slowly. Instead of the parallel Cu_6Sn_5 and Cu_3Sn growth seen in the electron inflow interface for both solder alloys, the IMC growth at the outflow interface differed between the two IMC compounds. In the SnCu solder, the Cu_6Sn_5 IMC grew more rapidly than the Cu_3Sn layer while in the SnCuIn the opposite occured. The Cu_3Sn growth in both alloys was similar at the outflow interface.

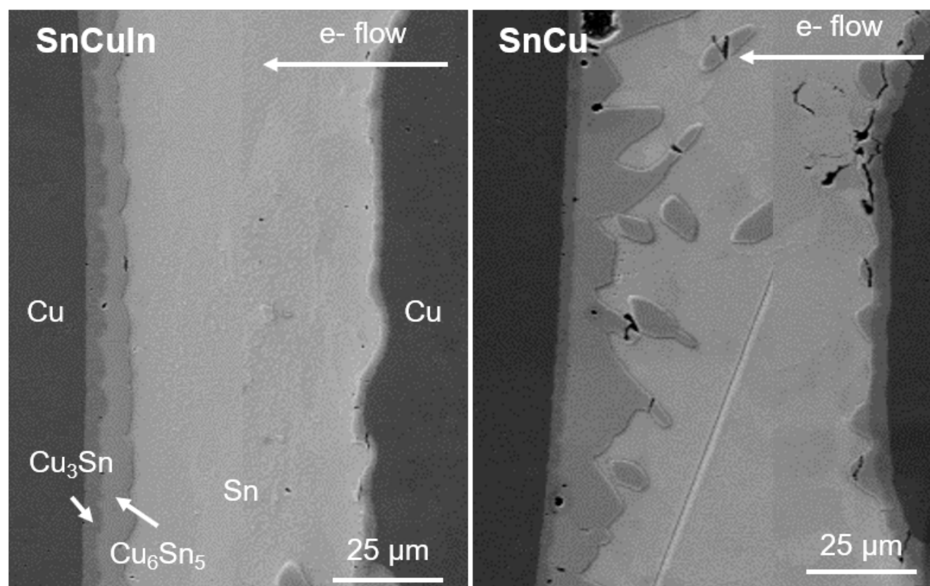

Figure 37. Higher magnification SEM images of the 200-hour EM-tested SnCuIn and SnCu solder joint interfaces, with phases and current flow direction marked.

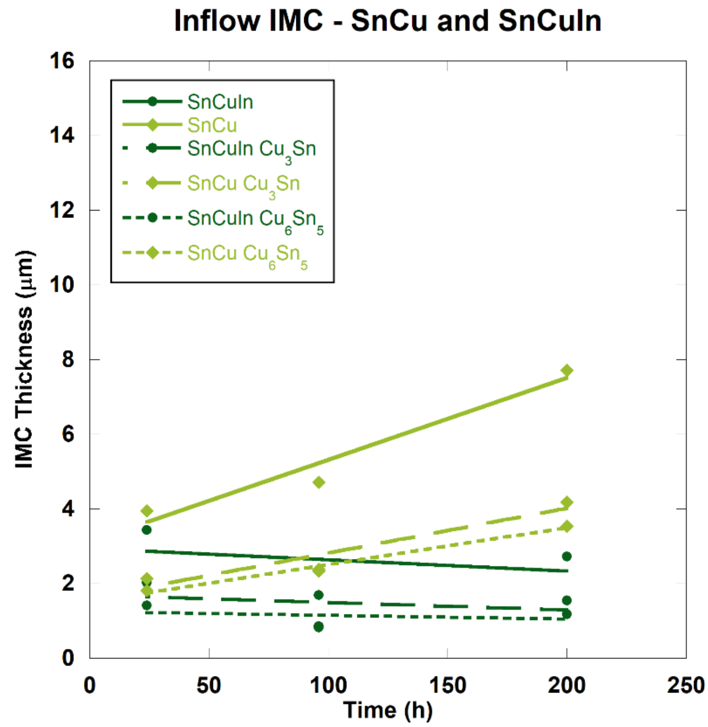

Figure 38. Electron-inflow interfacial IMC growth trends for total IMC thickness (solid lines), Cu_3Sn thickness (large dashed lines), and Cu_6Sn_5 IMC thickness (fine dashed lines). SnCu IMC growth is in light green and SnCuIn IMC growth is in dark green.

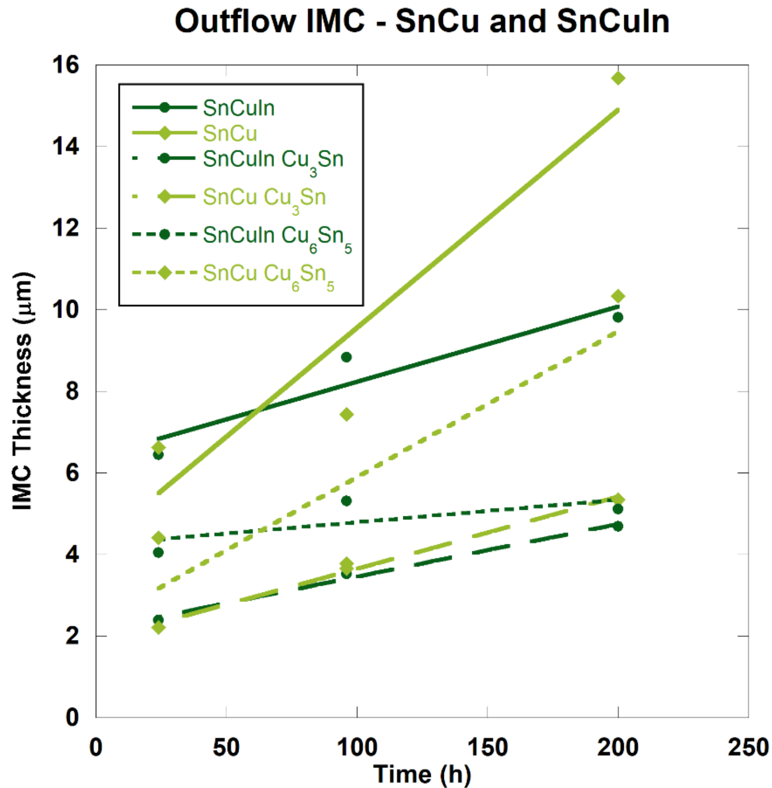

Figure 39. Electron-outflow interfacial IMC growth trends for total IMC thickness (solid lines), Cu_3Sn IMC thickness (large dashed lines), and Cu_6Sn_5 IMC thickness (fine dashed lines). SnCu IMC growth is in light green and SnCuIn IMC growth is in dark green.

In a 2016 study Kanlayasiri and Sukpimai suggested that addition of In to a low Ag SAC alloy reduced the growth of Cu_3Sn due to the incorporation of In into the interfacial IMC layers, stabilizing them and making the transformation from Cu_6Sn_5 to Cu_3Sn difficult (Kanlayasiri & Sukpimai 2016). This result was based on SEM and EDS analysis of solder samples aged for 1000 hours at 135°C and 170°C and SAC alloys with 0.5 – 3 wt% In. Our study does not show suppression of the Cu_3Sn layer, instead the most notable difference between the SnCu and SnCuIn alloys is the suppression of Cu_6Sn_5 visible in Figure 39. The argument that In could thermodynamically stabilize IMC

phases in the Sn-Cu system is plausible, as researchers have shown that In is highly soluble in multiple Sn-Cu IMCs (Ramos de Debiaggi et al. 2012; Liu et al. 2001; Lin et al. 2009), however detection of accurate In concentrations in Cu_3Sn and Cu_6Sn_5 phases via conventional EDS techniques is doubtful. The Sn Lα peak is separated from the In Lα peak by 0.157 keV or 157 eV (Jeol, EDS analysis energy table), very close to the approximate 130 eV energy resolution of EDS (Schwandt 2014). Therefore it would be very difficult to separate In signals from Sn and in most cases the EDS results for In in solder appear to simply mimic the Sn distribution with a lower intensity (Kanlayasiri & Sukpimai 2016; Tian et al. 2018). That noted, studies have reported In segregation at the electron inflow interface due to a back stress created by diffusing Sn (Sommadossi & Fernandez Guillermet 2007; Li et al. 2016) so EDS mapping of the electron inflow interface was done to investigate this effect. EDS mapping did not reveal a concentration of In near the electron inflow interface, although it is possible at the low concentration such segregation would not occur as this effect was only seen in In - 48wt% Sn alloys.

The IMC growth analysis suggested that the In addition effected Cu_6Sn_5 growth at the electron outflow interface so this region was selected for wavelength-dispersive x-ray spectroscopy (WDS) analysis as WDS has an energy resolution of 10 eV and would be able to distinguish between Sn and In (Schwandt 2014). The results of the WDS analysis are summarized in Figure 40 with Cu, Sn, and In maps in an interfacial region containing a grain boundary, Sn matrix, Cu substrate, and both IMC phases. A pure In standard was not available so the WDS results are qualitative and not quantitative. There was no detectable In concentration along the grain boundary, although Lee et al (Lee, Kim & Suganuma 2011) suggests this could be possible at higher In concentrations. A small dark

cluster in the Sn matrix adjacent to the Cu_6Sn_5 layer showed the only In concentration in the sample. Once the cluster was identified, the 24, 96, and 200-hour EM-tested SnCuIn samples were reanalyzed used EDS and a total of 15 In-containing clusters were identified. The cluster location within the sample was plotted versus EM-testing time as shown in Figure 41. The clusters formed or migrated closer to the electron outflow interface with increasing EM-testing time, suggesting that In diffusion occurred in the electron flow direction, the same as Cu and Sn diffusion. No clusters were seen in the thermally aged samples at either temperature.

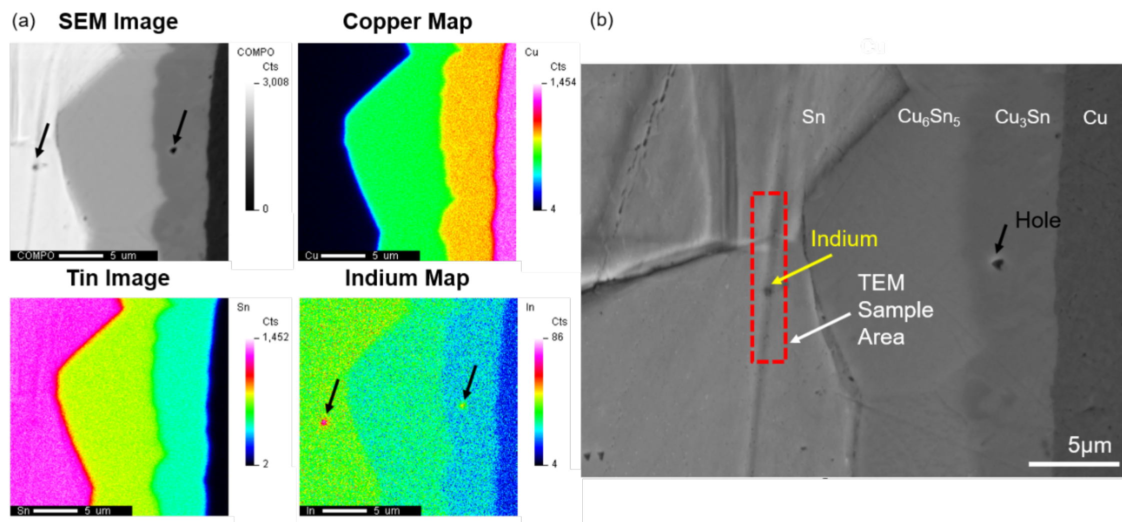

Figure 40. (a) WDS elemental maps for Cu, Sn, and In, showing In concentration in one region in Sn matrix. (b) SEM image of 200-hour EM-tested SnCuIn sample with In-containing region marked in yellow. Area for TEM lamella extraction is boxed in red and indicated.

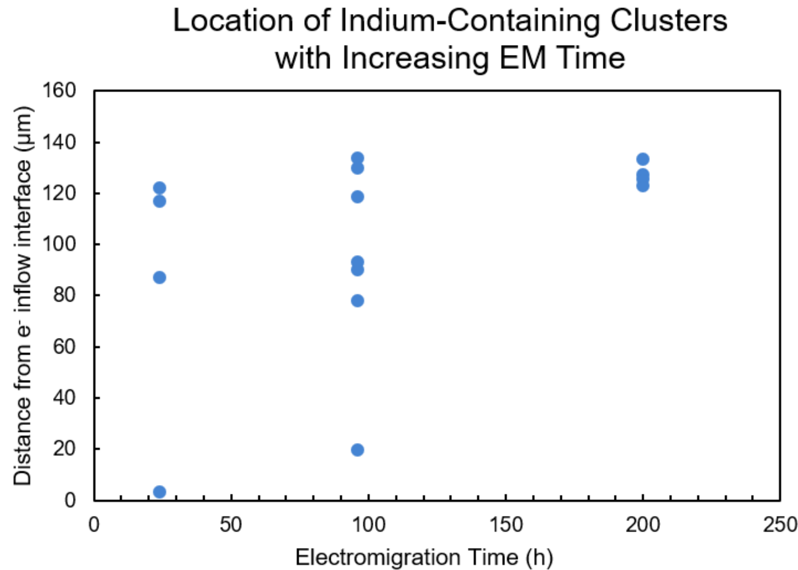

Figure 41. In-containing cluster location within the SnCuIn solder joints, showing cluster concentration at the electron outflow interface with increasing EM-testing time.

Once an In-containing cluster had been identified, a TEM lamella was prepared by focused ion beam (FIB) milling and lift out from the region indicated in red in Figure 40 (b). The lamella was meant to contain a grain boundary and the In cluster visible on the sample surface, however SEM and TEM analysis, shown in Figure 42, show that the surface cluster was not visible. It could have been destroyed in the process of sample thinning or simply not be visible using the tilt angles available in the TEM sample stage. Ion-thinning also posed an issue at the grain boundary, as a void was present at the boundary and rapidly grew during sample preparation. The uneven thinning around the boundary caused by the void made TEM analysis of the grain boundary difficult, but no second phase particles were seen. However, a spherical phase particle approximately 50 nm in diameter was detected, shown in Figure 42 (c-e). The particle was distinct in that it displayed two darker edges indicating strain caused by incoherency with the Sn matrix

and two lighter edges indicating coherency with the matrix. Fast fourier transform (FFT) analysis of the particle and surrounding material revealed that it was a triclinic Cu_7In_3 particle in pure Sn matrix, shown in Figure 43. To investigate its coherency relationship with the matrix, FFTs were taken in a line from the center of the particle, across the particle-matrix boundary, and into the bulk. The progression of FFTs shown in Figure 44 (b) demonstrate the transition from the (-122) plane of the Cu_7In_3 particle to the (001) plane of the Sn matrix. The atomic spacing of the planes was calculated to be 3.21Å and 3.18Å, respectively, a 0.3Å difference that was easily accommodated. This analysis confirmed the semicoherent nature of the Cu_7In_3 particle with the Sn matrix, a relationship that has not been described before. No other In-containing IMCs were identified. It is possible that the trace amount of In migrated to the electron outflow interface and then reacted with Cu in the solder bulk to form Cu_7In_3. A high density of semicoherent secondary IMC particles could form a strain field adjacent to the electron outflow interface, limiting Cu diffusion to the interface and therefore slowing the growth of Cu_6Sn_5. The growth of Cu_3Sn would not be affected, as it forms by consuming the Cu_6Sn_5 layer already present at the interface in the as-fabricated condition.

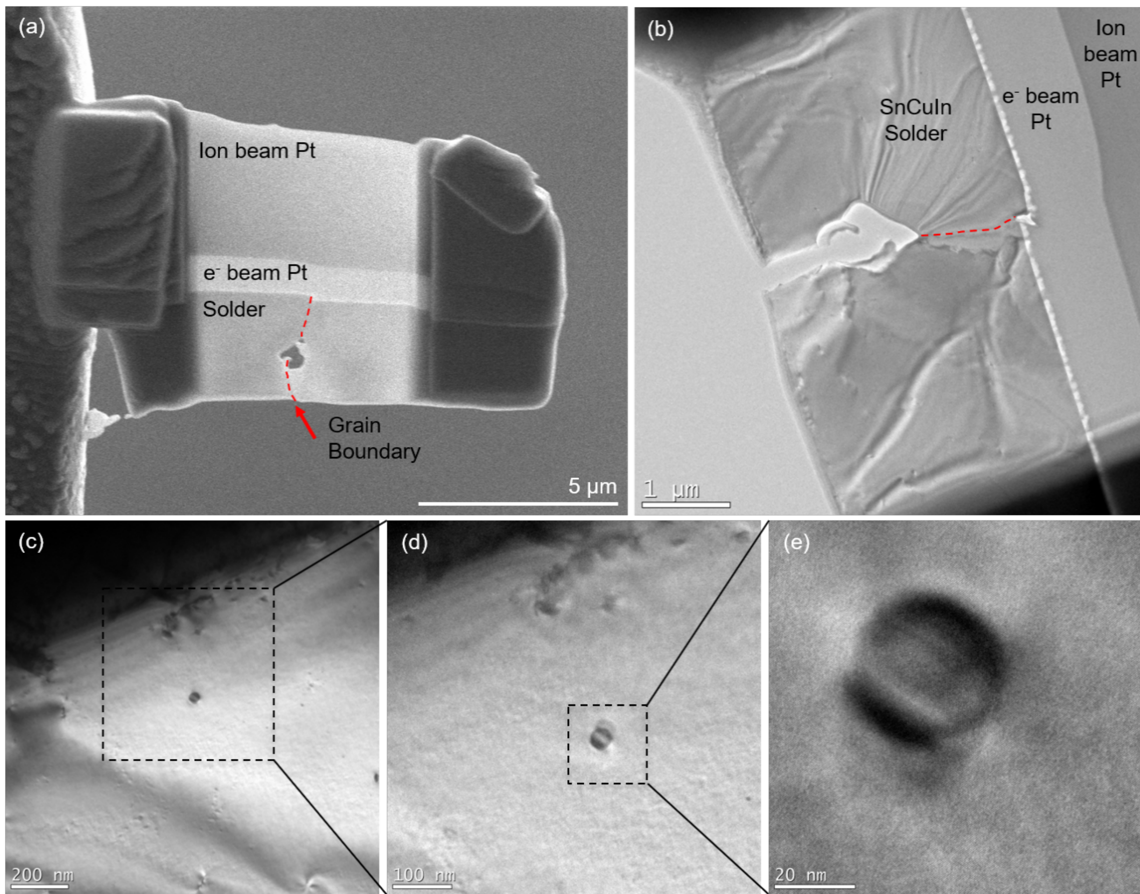

Figure 42. (a) SEM image of TEM lamella at intermediate thinning stage, with a hole that has formed along the grain boundary. (b) TEM image of lamella, with grain boundary marked. (c-e) TEM images of large spherical particle in the Sn matrix.

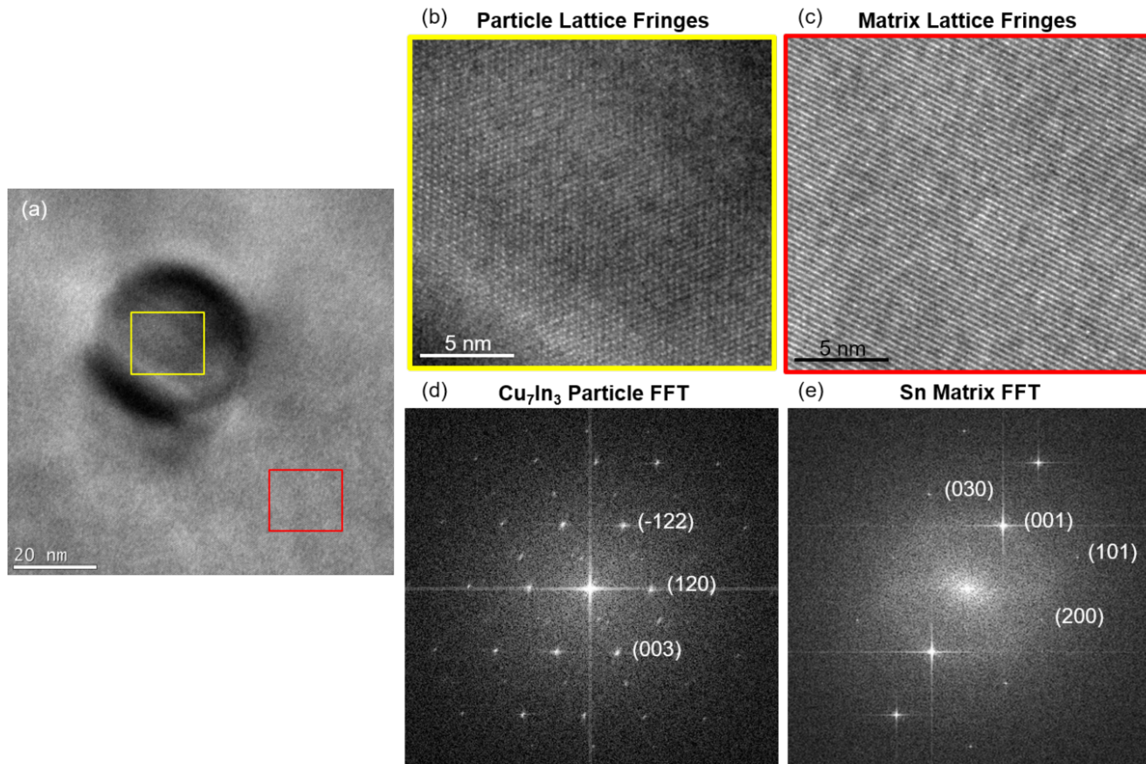

Figure 43. (a) TEM image of spherical particle in the Sn matrix. (b-c) Higher resolution TEM images of regions indicated in (a). (d-e) FFT analysis of marked regions the particle to be Cu_7In_3 and the matrix to be pure Sn.

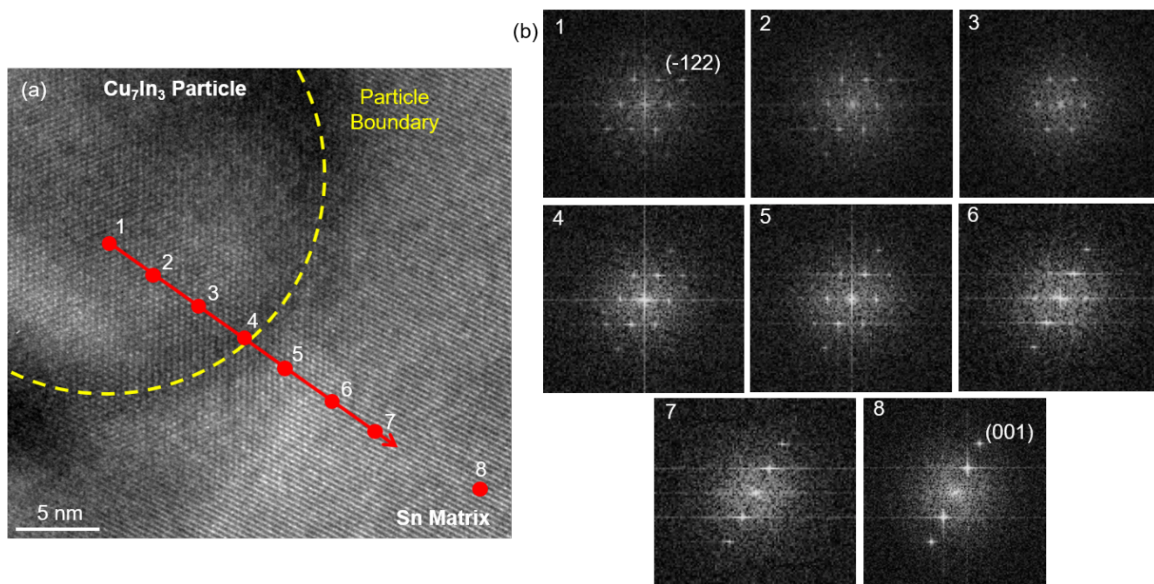

Figure 44. (a) TEM image of spherical Cu_7In_3 particle in the Sn matrix, with particle boundary indicated. (b) FFT's taken along the red line indicated in (a), progressing from 1, inside the particle to 8, in the Sn matrix. FTT's show coherency between the (-122) plane of Cu_7In_3 and the (001) plane Sn.

6.4 Summary

The goal of this study was to determine how the addition of a trace amount of In (<1 wt%) would affect the microstructure and evolution of solder joints subjected to EM and thermal aging. EM testing was done at a current density of $1x10^4$ A/cm^2 and thermal aging was done at 160°C and 200°C. The tests were run for 24, 96, and 200 hours with a sample fabricated at each condition for both a SnCu and SnCuIn alloy, resulting in a total of 18 solder joints. The polished joint cross sections were analyzed using SEM, EBSD, and EDS. The 200-hour EM-tested SnCuIn joint also underwent WDS characterization and a TEM lamella was prepared from an interfacial region shown to contain In. The following results were discovered.

1. There was no microstructural difference between the SnCu and SnCuIn samples that underwent thermal aging.
2. No grain refinement or In segregation to grain boundaries was seen in any testing condition.
3. In the EM-tested samples, the SnCuIn solder experienced suppression of Cu_6Sn_5 growth at the electron outflow interface, instead of Cu_3Sn suppression reported by other researchers (Kanlayasiri & Sukpimai 2016).
4. WDS analysis of an interfacial region of the 200-hour EM-testing SnCuIn sample revealed a cluster of In adjacent to the electron outflow interface.

Further EDS analysis of In-containing clusters in showed progressive movement of the clusters toward the electron outflow interface with increasing EM-time. This suggests that at low concentrations In diffuses in the same direction as other alloy elements, instead of the back diffusion seen in solders with high In concentrations (Li et al. 2016).

5. TEM analysis confirmed that In was present in the form of a Cu_7In_3 particle. FFT analysis demonstrated that the particle had a semicoherent relationship with the Sn matrix.

This study confirmed that In addition to a SnCu alloy might help reduce EM-induced damage by suppressing the formation of Cu_6Sn_5. It also highlights the difficulty in characterizing samples with trace additions of alloying elements, especially if they are close to the majority constituent on the periodic table. In-containing solder alloys exhibit a wide variety of behaviors, highly influenced by sample fabrication technique and In-concentration, making comparison between studies difficult. While In has been reported to be soluble in interfacial Sn-Cu IMC layers (Ramos de Debiaggi et al. 2012; Liu et al. 2001; Lin et al. 2009), this is believed to be the first reporting of a semicoherent relationship between a Cu_7In_3 particle and Sn matrix. The effect of a high density of semicoherent particles on EM-driven diffusion is interesting and should be studied further.

CHAPTER 7

CONCLUSIONS

7.1 Summary of Research Findings

- Single crystal and bicrystal pure Sn solder joints were isolated from a larger sample through a two-step fabrication technique. Multiple joints with a variety of grain orientations and structures were created with nearly identical void and IMC distributions. Samples were selected for EM-testing and thermal aging based on their θ angle orientations and grain boundary character so grain orientation and grain boundary effects on EM damage could be studied and compared. Lab-based x-ray microtomography allowed for the quantification and visualization of microstructural phases in 3D and the calculation of bulk IMC and void growth rates that were previously not possible.
- Single crystal and bicrystal samples with similar θ angles were thermally aged and compared to EM-tested samples. Thermally aged samples experienced little surface deformation and showed IMC growth in the form of particle coarsening along grain boundaries. EM-tested samples displayed an enormous difference in IMC growth between low θ angle, high θ angle, and bicrystal samples composed of both high and low θ angle grains, highlighting the importance of grain orientation in EM-damage.
- Solder grain orientation and structure were found to strongly influence the structure and orientation of Cu_6Sn_5 IMC grown during EM in the low θ angle and bicrystal samples. Rapid diffusion of Cu to the electron outflow interface, without impedance in the solder bulk, resulted in the growth of coarse columnar Cu_6Sn_5

grains with a basal plane alignment parallel to the solder-Cu interface. The IMC columns consumed nearly the entire solder matrix. The bicrystal sample displayed a complex network of rod-like Cu_6Sn_5 IMC particles that nucleated at grain boundaries in the sample bulk and therefore had random orientations.

- The formation of Cu_6Sn_5 IMC particles at grain boundaries was linked to extensive sample recrystallization by PSN recrystallization where particle growth at grain boundaries causes recrystallization of the matrix surrounding the particle and therefore increased grain boundary density for particle formation. The combination of 3D IMC structure provided by x-ray microtomography, orientation and structure provided by EBSD analysis, and cross section characterization in the SEM was critical for this discovery.
- Void growth in EM tested samples was shown to take two distinct forms: void faceting, previously unreported in solders, and void burrowing. Void faceting formed as a result of anisotropic atomic diffusivity on void surfaces, characteristic of Sn. Void burrowing occurred due to rapid diffusion of Cu into the solder bulk and a local increase in current density surrounding interfacial voids. In high θ angle grains, spherical voids developed flat facets and pointed corners, while in low θ angle grains voids remained spherical while the Cu interface evolved around them.
- The relationship between grain boundaries and Cu_6Sn_5 IMC structure was further probed with interrupted EM testing of a bicrystal solder joint containing a high angle boundary perpendicular to the electron flow and a series of parallel 62.8° twins. X-ray microtomography revealed that while IMC growth along the twin

boundaries and horizontal boundary were both rapid initially, the coarsening of IMC in the solder bulk created a shadowing effect and slowed growth of IMC along the horizontal grain boundary. The bulk IMC initially formed in parallel plates, aligned with the twin boundaries, but upon further testing a secondary bulk IMC formed. The secondary IMC also formed in plates, but on a different orientation, and consumed the primary IMC. Through EBSD and SEM analysis of post-testing cross sections, a secondary network of twins was identified and related to the secondary IMC network. Cyclic removal of the solder joint for tomography resulted in cyclic thermal expansion and compression of the solder bulk, which formed the secondary twin network.

- Thermal cycling appeared to mitigate void growth in the interrupted EM bicrystal sample. Voids at both interfaces showed shrinkage in line with the compression experienced by the solder region as a whole. Cu diffusion along the electron flow direction created an uneven Cu interface due to current crowding around interfacial voids. Upon compression the voids were collapsed against the uneven Cu interface and broke into many small voids in a process termed void splitting.
- The effect of trace addition of In (<1 wt%) on the behavior of SnCu solder undergoing thermal aging and EM was studied at three time steps. Interfacial IMC characterization detected no microstructural difference between thermally aged samples of SnCu or SnCuIn. EM-tested SnCuIn samples displayed lower IMC growth at the electron inflow interface and suppressed Cu_6Sn_5 growth at the outflow interface when compared to SnCu counterparts. This finding contrasts

with the reported Cu_3Sn suppression found during thermal aging of In-containing solders.

- In-containing clusters, identified through WDS and EDS, were found to migrate in the direction of the electron flow and accumulate at the electron outflow interface. TEM analysis of a lamella prepared from an In-containing region found a triclinic Cu_7In_3 particle in the Sn matrix. The particle had a semicoherent relationship with the Sn matrix, suggesting that a high density of such particles could affect the lattice strain adjacent to the electron outflow boundary and the diffusion of Cu atoms to the interface, causing the suppression of interfacial Cu_6Sn_5 growth.

7.2 Future Work

This work has demonstrated the complex, interconnect nature of grain structure, alloy composition, and EM-damage concerns of IMC and void growth, but much remains to be done. An avenue of future research could be the relationship between IMC formed at various grain boundary types and joint failure through mechanical loading. Hexagonal Cu_6Sn_5 is weakest along its basal plane, making transgranular fracture through particles aligned in the same direction easy. Conversely, disconnected, randomly oriented IMC particles would fracture at a variety of stresses and require a crack to progress through the Sn matrix before connecting to another particle, leading to the slowing of crack growth. Void faceting is another potential reliability concern, due to the formation of corners that could become stress concentration sites. As single crystal, slow diffusion solder joints are attractive for mitigating IMC growth, the degree of faceting and its relationship with mechanical loading and joint fracture should be characterized to better understand their

reliability. The finding that thermally induced compression halted void growth could be carried further as an investigation into the reduction of EM-caused void growth by inducing compressive stress in the solder matrix through the addition of second phase particles or alloying elements. To the same aim, further studies into the effect of In on solders should probe a variety of compositions and study EM in the context of single crystal and bicrystal joints in order to isolate structural effects. Instead of constant temperature holds, as were done for the thermal aging studies, the effect of thermal cycling on electromigration damage should also be further explored. Samples could be thermally cycled from a selected low temperature to a selected high temperature, based on the application desired for that solder composition, for example -55°C to 95°C for solder in an automotive context. Thermal cycling should be done with and without current application to elucidate the differences between pure electromigration and the combination of thermal and electromigration effects. Finally, this research could be further expanded upon by modifying sample geometry to better mimic solder joints created in industry by adding silicon dies, PCB connections, and underfill. All of these components experience thermal expansion and resistive heating. Their inclusion would add an additional layer of complexity and realism to thermal and electromigration studies.

REFERENCES

(Arzt et al 1994) E. Arzt, O. Kraft, W. Nix and J. S. Jr., "Electromigration failure by shape change of voids in bamboo lines," J. App. Phys., vol. 76, no. 3, 1994.

(Averbuch, Israeli & Ravve 2003) A. Averbuch, M. Israeli and I. Ravve, "Electromigration of intergranular voids in metal films for microelectronic interconnects," J. Comp. Phys., vol. 186, pp. 481-502, 2003.

(Bahari et al. 2003) Z. Bahari, E. Dichi, B. Legendre, and J. Dugue, “The equilibrium phase diagram of the copper–indium system: a new investigation,” Thermo. Acta, vol. 401, pp. 313-138, 2003.

(Basaran et al. 2002) C. Basaran, S. Li, D. C. Hopkins, D. Veychard, J. Appl. Phys., vol. 106, 013707, 2009.

(Belyakov & Atkinson 2010) S. Belyakov, H.V. Atkinson, S.P.A. Gill, Crystallographically Faceted Void Formation in the Matrix of Lead-Free Solder Joints, J. Electron. Mater. vol. 39, 2010. https://doi.org/10.1007/s11664-010-1184-6

(Bieler et al. 2006) T. R. Bieler, H. Jiang, L. P. Lehman, T. Kirkpatrick, E. J. Cotts, “Influence of Sn Grain Size and Orientation on the Thermomechanical Response and Reliability of Pb-free Solder Joints,” Electron. Comp. Tech. Conference, pp.1462-1467, 2006.

(Bieler et al. 2012) T. Bieler, B. Zhou, L. Blair, A. Zamiri, P. Darbandi, F. Pourboghrat, T.-K. Lee and K.-C. Liu, "The Role of Elastic and Plastic Anisotropy of Sn in Recrystallization and Damage Evolution During Thermal Cycling in SAC305 Solder Joint," J. Electron. Mater., vol. 41, no. 2, 2012.

(Blakely 1973) J.M. Blakely, “Introduction to the Properties of Crystal Surfaces,” Pergamon Press (1973)

(Borgesen et al. 2018) P. Borgesen, L. Wentlent, S. Hamasha, S. Khasawneh, S. Shirazi, D. Schmitz, T. Alghoul, C. Greene and L. Yin, "A Mechanistic Thermal Fatigue Model for SnAgCu Solder Joints," J. Electron. Mater., vol. 47, no. 5, 2018.

(Chalmers 1935) B. Chalmers, "The twinning of single crystals of tin," Proc. Phys. Soc., vol. 47, pp. 733-746, 1935.

(Chang et al. 2017) Y.-W. Chang, Y. Cheng, L. Helfen, F. Xu, T. Tian, M. Scheel, M. D. Michiel, C. Chen, K. Tu and T. Baumbach, "Electromigration Mechanisms of Failure in Flip-Chip Solder Joints Based on Discrete Void Formation," Nature Sci. Reports, 2017.

(Chang, Chiang & Chen 2007) Y.W. Chang, T.H. Chiang, C. Chen, “Effect of void propagation on bump resistance due to electromigration in flipchip solder joints using

Kelvin structure," Appl. Phys. Lett., vol. 91, 132113, 2007. https://doi.org/10.1063/1.2790376

(Chang, Liang & Chen 2006) Y.W. Chang, S.W. Liang, C. Chen, "Study of void formation due to electromigration in flip-chip solder joints using Kelvin bump probes," Appl. Phys. Lett., vol. 89, 032103, 2006. https://doi.org/10.1063/1.2226989

(Chen & Liang 2007) C. Chen, S.W. Liang, J. Mat. Sci.: Mater. Electron., vol. 18, pp. 259-268, 2007.

(Chen et al. 2012) C. Chen, H.-Y. Hsiao, Y.-W. Chang, F. Ouyang, K.N. Tu, Mater. Sci. Engin. R., vol. 73, pp. 85-100, 2012.

(Chen et al. 2013) J.-Q. Chen, J.-D. Guo, K.-L. Liu and J.-K. Shang, "Dependence of electromigration damage on Sn grain orientation in Sn–Ag–Cu solder joints," J. App. Phys., vol. 114, p. 153509, 2013.

(Chen et al. 2015) H. Chen, C. Hang, X. Fu, M. Li, "Microstructure and Grain Orientation Evolution in Sn-3.0Ag0.5Cu Solder Interconnects Under Electrical Current Stressing," J. Electron, Mater., vol. 44, pp. 3880-3887, 2015. https://doi.org/10.1007/s11664-015-3922-2

(Chen, Guo, et al 2015) J.-Q. Chen, J.-D. Guo, H.-C. Ma, K.-L. Liu, Q.-S. Zhu, J. Mater. Re., vol. 30, no. 8, pp. 1065-1071, 2015.

(Chen, Wang et al. 2012) H. Chen, L. Wang, J. Han, M. Li and H. Liu, "Microstructure, orientation and damage evolution in SnPb, SnAgCu, and mixed solder interconnects under thermomechanical stress," Microelectron. Eng., vol. 96, pp. 82-91, 2012.

(Daghfal & Shang 2007) J.P. Daghfal and J. K. Shang, "Current-Induced Phase Partitioning in Eutectic Indium-Tin Pb-Free Solder Interconnect," J. Electron. Mater., vol. 36, no. 10, 2007.

(Decker, Candland & Vanfleet 1975) D. L. Decker, C. T. Candland and H. B. Vanfleet, "Diffusion of Pd in Pb at high pressures," Phys. Rev. B, vol. 11, no. 12, pp. 4885-4890, 1975.

(Deng et al. 2005) X. Deng, R. Sidhu, P. Johnson and N. Chawla, "Influence of Reflow and Thermal Aging on the Shear Strength and Fracture Behavior of Sn-3.5Ag Solder/Cu Joints," Metal. Mater. Trans. A, vol. 36A, pp. 55-64, 2005.

(Doherty et al. 1997) R. D. Doherty, D.A. Hughes, F.J. Humphreys, J.J. Jonas, D. Juul Jensen, M.E. Kassner, W.E. King, T.R. McNelley, H.J. McQueen, A.D. Rollett, Current issues in recrystallization: a review, J. Mater. Sci. Eng. A, vol. 238, pp. 219-274, 1997. 0921-5093/97

(Dyson, Anthony & Turnbull 1967) B. Dyson, T. Anthony and D. Turnbull, "Intersistial Diffusion of Copper in Tin," J. Appl. Phys., vol. 38, p. 3408, 1967.

(Eckhold et al. 2015) P. Eckhold, M.S. Sellers, R. Niewa, W. Hugel, “The surface energies of β-Sn — A new concept for corrosion and whisker mitigation,” Microelectron. Reliab., vol. 55, pp. 2799-2807, 2015. https://doi.org/10.1016/j.microrel.2015.08.018

(Fridline & Bower 1999) D.R. Fridline, A.F. Bower, “Influence of anisotropic surface diffusivity on electromigration induced void migration and evolution,” J. Appl. Phys., vol. 85, 3168, 1999. https://doi.org/10.1063/1.369656

(Gan & Tu 2002) H. Gan, K.N. Tu, Proceedings of IEEE Electronic Components and Technology Conference, pp.1206-1212, 2002.

(Gan & Tu 2005) H. Gan and K. N. Tu, “Polarity effect of electromigration on kinetics of intermetallic compound formation in Pb-free solder V-groove samples,” J. Appl. Phys., vol. 97, 2005. https://doi.org/10.1063/1.1861151

(Han et al. 2012) J. Han, D. Choi, M. Fujiyoshi, N. Chiwata and K. Tu, "Current density redistribution from no current crowding to current crowding in Pb-free solder joints with an extremely thick Cu layer," Acta Mater., vol. 60, pp. 102-111, 2012.

(Ho et al. 2016) C.E. Ho, C.H. Yang, P.T. Lee, C.T. Chen, “Real-time X-ray microscopy study of electromigration in microelectronic solder joints,” Scripta Mater., vol. 114, pp. 79-83, 2016. https://doi.org/10.1016/j.scriptamat.2015.12.001

(Hu et al. 2003) Y.C. Hu, Y.H. Lin, C.R. Kao, K.N. Tu, “Electromigration failure in flip chip solder joints due to rapid dissolution of copper,” J. Mater. Res., vol.18, 2003. https://doi.org/10.1557/JMR.2003.0355

(Huang et al. 2015) M. Huang, J. Zhao, Z. Zhang and N. Zhao, "Role of diffusion anisotropy in beta-Sn in microstructural evolution of Sn-3.0Ag-0.5Cu flip chip bumps undergoing electromigration," Acta Mater., vol. 100, pp. 98-106, 2015.

(Huang et al. 2016) M. L. Huang, J. F. Zhao, Z. J. Zhang, N. Zhao, “Dominant effect of high anisotropy in β-Sn grain on electromigration-induced failure mechanism in Sn-3.0Ag-0.5Cu interconnect,” J. Alloy. Compd., vol. 678, pp. 370-374, 2016. https://doi.org/10.1016/j.jallcom.2016.04.024

(Huntington & Grone 1961) H.B. Huntigton, A.R. Grone, J. Phys.: Chem. Solids, vol. 20, no. 76, 1961.

(Ishii 1959) K. Ishii, "Deformation Twinning of Tin Single Crystals under Impact Loading," J. Phys. Soc. Japan, vol. 14, no. 10, 1959.

(Jiang & Chawla 2010) L. Jiang and N. Chawla, "Mechanical properties of Cu6Sn5 intermetallic by micropillar compression testing," Scripta Mater., vol. 63, pp. 480-483, 2010.

(Jiang, Jiang & Chawla 2012) L. Jiang, H. Jiang and N. Chawla, "The Effect of Crystallographic Orientation on the Mechanical Behavior of Cu6Sn5 by Micropillar Compression Testing," J. Electron. Mater., vol. 41, no. 8, 2012.

(Kanlayasiri & Sukpimai 2016) K. Kanlayasiri and K. Sukpimai, “Effects of indium on the intermetallic layer between low-Ag SAC0307- xIn lead-free solders and Cu substrate,” J. Alloy. Compd., vol. 668, pp. 169-175, 2016.

(Kanlayasiri, Mongkolwongrojn & Ariga 2009) K. Kanlayasiri, M. Mongkolwongrojn, and T. Ariga, “Influence of indium addition on characteristics of Sn-0.3Ag-0.7Cu solder alloy,” J. Alloy. Compd., vol. 485, pp. 225-230, 2009.

(Kao 1997) C. R. Kao, “Microstructures developed in solid-liquid reactions: using Cu-Sn reaction, Ni-Bi reaction, and Cu-In reaction as examples,” Mater. Sci. Eng. A,, vol. 238, pp. 196-201, 1997.

(Ke et al. 2011) J.H. Ke at al. Acta Mater., vol. 59, pp. 2462-2468, 2011.

(Kerr & Chawla 2004) M. Kerr and N. Chawla, "Creep deformation behavior of Sn-3.5Ag solder/Cu couple at small length scales," Acta Mater., vol. 52, pp. 4527-4535, 2004.

(Khosa & Huntington 1975) A. Khosla, H. B. Huntington, Electromigration in Tin Single Crystals, J. Phys. Chem. Solids, vol. 36, pp. 395-399, 1975.

(Kim & Lu 2006) D. Kim and W. Lu, "Creep flow, diffusion, and electromigration in small scale interconnects," J. Mech. Phys. Solids, vol. 54, pp. 2554-2568, 2006.

(Kraft & Artz 1997) O. Kraft, E. Artz, “Electromigration Mechanisms in Conductor Lines: Void Shape Changes and Slit-like Failure,” Acta Mater., vol. 47, pp. 1599-1611, 1997. 1359-6454/97

(Lee & Stone 1994) S.-M. Lee and D. Stone, "Grain Boundary Sliding in As-Cast Pb-Sn Eutectic," Scripta Metal. Mater., vol. 40, no. 9, 1994.

(Lee et al. 2010) T.K. Lee, B. Zhou, L. Blair, K.C. Liu, T.R. Bieler, “Sn-Ag-Cu Solder Joint Microstructure and Orientation Evolution as a Function of Position and Thermal Cycles in Ball Grid Arrays Using Orientation Imaging Microscopy,” J. Electron. Mater., vol. 39, pp. 2588-2597, 2010. https://doi.org/10.1007/s11664-010-1348-4

(Lee et al. 2011) K. Lee, K.-S. Kim, Y. Tsukada, K. Suganuma, K. Yamanaka, S. Kuritani and M. Ueshima, "Influence of crystallographic orientation of Sn-Ag-Cu on electromigration in flip-chip joint," Microelectron. Reliab., vol. 51, pp. 2209-2297, 2011.

(Lee, Kim & Suganuma 2011) K. Lee, K.-S. Kim, and K. Suganuma, “Influence of indium addition on electromigration behavior of solder joint,” J. Mater. Res., vol. 26, no. 20, 2011.

(Lehman et al. 2010) L. Lehman, Y. Xing, T. Bieler and E. Cotts, "Cyclic twin nucleation in tin-based solder alloys," Acta Mater., vol. 58, pp. 3546-3556, 2010.

(Li & Basaran 2009) S. Li, C. Basaran, Comp. Mater. Sci., vol. 47, pp. 71-78, 2009.

(Li et al. 2012) Y. Li, J.S. Moor, B. Pathangey, R.C. Dias, D. Goyal, "Lead-Free Solder Joint Void Evolution During Multiple Subsequent High-Temperature Reflow," IEEE Trans. Dev. Mater. Reliab., vol. 12, 2012. https://doi.org/10.1109/TDMR.2012.2190736

(Li et al. 2014) L. F. Li, Y. K. Cheng, G. L. Xu, E. Z. Wang, Z. H. Zhang, and H. Wang, "Effects of indium addition on properties and wettability of Sn-0.7Cu-0.2Ni lead-free solders," Mater. Design, vol. 64, pp.15-20, 2014.

(Li et al. 2016) Y. Li, A. B. Y. Lim, K. Luo, Z. Chen, F. Wu, and Y. C. Chan, "Phase segregation, interfacial intermetallic growth and electromigration-induced failure in Cu/Ine48Sn/Cu solder interconnects under current stressing," J. Alloy. Compd., vol. 673, pp. 372-382, 2016.

(Li, Yang & Kim 2012) M. Li, M. Yang, J. Kim, "Textured growth of Cu6Sn5 grains formed at a Sn3.5Ag/Cu interface," Mater. Lett., vol. 66, pp.135-137, 2012. https://doi.org/10.1016/j.matlet.2011.08.014

(Lin et al. 2005) Y.H. Lin, Y.C. Hu, C.M. Tsai, C.R. Kao, K.N. Tu, "In situ observation of the void formation-and-propagation mechanism in solder joints under current-stressing," Acta Mater., vol. 53, pp. 2029-2035, 2005. https://doi.org/10.1016/j.actamat.2005.01.014

(Lin et al. 2006) Y. Lin, C. Tsai, Y. Hu, Y. Lin and C. Kao, "Electromigration-Induced Failure in Flip-Chip Solder Joints," J. Electron. Mater., vol. 34, no. 1, 2006.

(Lin et al. 2009) S.-K. Lin, T.-Y. Chung, S.-W. Chen, and C.-H. Chang, "250°C isothermal section of ternary Sn-In-Cu phase equilibria," J. Mater. Res., vol. 24, no. 8, 2009.

(Lin, Lin & Chuang 2009) H.-J. Lin, J.-S. Lin, T.-H. Chuang, J. Alloy. Compd., vol. 487, pp. 458-465, 2009.

(Liu et al. 2001) X.J. Liu, H.S. Liu, I. Ohnuma, R. Kainuma, K. Ishida, S. Itabashi, K. Kameda, and K. Yamaguchi, "Experimental Determination and Thermodynamic Calculation of the Phase Equilibria in the Cu-In-Sn System," J. Electron. Mater., vol. 30, no. 9. 2001.

(Liu et al. 2016) P. Liu, S. Wang, D. Li, Y. Li and X.-Q. Chen, "Fast and Huge Anisotropic Diffusion of Cu (Ag) and Its Resistance on the Sn Self-diffusivity in Solid β-Sn," J. Mat. Sci. Tech., vol. 32, pp. 121-128, 2016.

(Lloyd, Tu & Jaspal 2004) J.R. Lloyd, K.N. Tu and J. Jaspal, "The Physics and Materials Science of Electromigration and Thermomigration in Solders", Chapter 20 of "Handbook of Lead-Free Solder Technology", edited by K. J. Puttlitz and K. A. Stalter, Marcel Dekker Inc., New York, New York, 2004.

(Lu et al. 2008) M. Lu, D. Y. Shih, P. Lauro, C. Goldsmith, D. W. Henderson, "Effect of Sn grain orientation on electromigration degradation mechanism in high Sn-based Pb-free solders," Appl. Phys. Lett., vol. 92, 211909, 2008. https://doi.org/10.1063/1.2936996

(Lu et al. 2010) Y.-D. Lu et al., Proceedings of 11th IEEE International Conference on Electronic Packaging Technology and High Density Packaging, pp. 824-827, 2010.

(Ma et al. 2018) Z. Ma, J. Xian, S. Belyakov and C. Gourlay, "Nucleation and twinning in tin droplet solidification on single crystal intermetallic compounds," Acta Mater., vol. 150, pp. 281-294, 2018.

(Mahapatra et al. 2017) S. Das Mahapatra, B. S. Majumdar, I. Dutta, and S. Bhassyvasantha, "Eliminating Whisker Growth by Indium Addition in Electroplated Sn on Copper Substrate," J. Electron. Mater., vol. 46, no. 7, 2017.

(Maruyama 1960) S. Maruyama, "Dynamic Behavior of Twinning in Tin Crystals at Various Temperatures and Strain Rates," J. Phys. Soc. Japan, vol. 15, no. 7, 1960.

(Matilla & Kivilahti 2012) T. Matilla, J. K. Kivilahti, "The Failure Mechanism of Recrystallization-Assisted Cracking of Solder Interconnections" Krzysztof Sztwiertnia, IntechOpen, 2012. https://doi.org/10.5772/37899

(Matin & Coenen 2005) M. Matin, E. Coenen, W. Vellinga and M. Geers, "Correlation between thermal fatigue and thermal anisotropy in a Pb-free solder alloy," Scripta Mater., vol. 53, pp. 927-932, 2005.

(Matin, Vellinga & Geers 2006) M. Matin, W. Vellinga and M. Geers, "Microstructure evolution in a Pb-free solder alloy during mechanical fatigue," Mater. Sci. Eng. A, vol. 431, pp. 166-174, 2006.

(Matin, Vellinga & Geers 2007) M. Matin, W. Vellinga and M. Geers, "Thermomechanical fatigue damage evolution in SAC solder joints," Mater. Sci. Eng. A, Vols. 445-446, pp. 73-85, 2007.

(Meakin & Klokholm 1960) J. D. Meakin and E. Klokholm: Trans. Metal. Soc. AIME, vol. 218, 1960.

(Mehrer 2007) H. Mehrer, "Diffusion in Solids: Fundamentals, Methods, Materials, Diffusion-Controlled Processes," Chapters 19 and 25, Springer, New York, 2007.

(Mehrer & Divinski 2009) H. Mehrer and S. Divinski, "Diffusion in Metallic Elements and Intermetallics," Def. Diff. Forum, pp.15-38, 2009.

(Mertens, Kirubanandham & Chawla 2015) J. Mertens, A. Kirubanandham and N. Chawla, "In situ fixture for multi-modal characterization during electromigration and thermal testing of wire-like microscale specimens," Microelectron. Reliab., vol. 55, pp. 2345-2353, 2015.

(Mertens, Kirubanandham & Chawla 2016) J.C.E. Mertens, A. Kirubanandhan, N. Chawla, "Electromigration mechanisms in Sn-0.7Cu/Cu couples by four dimensional (4D) X-ray microtomography and electron backscatter diffraction (EBSD)," Acta Mater., vol. 102, pp. 220-230, 2016. https://doi.org/10.1016/j.actamat.2015.08.073

(Nakajima & Huntington 1981) H. Nakajima and H. B. Huntington, "Electromigration of Cadmium in Lead," J. Phys. Chem. Solids, vol. 42, pp. 171-184, 1981.

(Nicholas 1955) J. F. Nicholas, "The Mechanisms of Self-Diffusion in Tin," Acta Metall. vol. 3, pp. 178-181, 1955

(Orgutani & Oren 2004) T.O. Orgutani, E.E. Oren, "Electromigration-induced void grain-boundary interactions: The mean time to failure for copper interconnects with bamboo and near-bamboo structures," J. Appl. Phys., vol. 96, 7246, 2004. https://doi.org/10.1063/1.1815389

(Ouyang, Tu & Lai 2012) F. Y. Ouyang, K.N. Tu, T.S. Lai, "Effect of electromigration induced joule heating and strain on microstructural recrystallization in eutectic SnPb flip chip solder joints," J. Mater. Chem. Phys., vol. 136, pp. 210-218, 2012. https://doi.org/10.1016/j.matchemphys.2012.06.054

(Pete et al. 2012) D.J. Pete, J.B. Helonde, A.V. Vairagar, S.G. Mhaisalkar, "A Model for Understanding Electromigration-Induced Void Evolution in Dual-Inlaid Cu Interconnect Structure," J. Electron. Mater., vol. 41, pp. 586-572, 2012. https://doi.org/10.1007/s11664-011-1855-y

(Pollock 1993) D. D. Pollock, "Physical properties of materials for engineers", 2nd ed. Boca Raton, Fla.: CRC Press, 1993.

(Qian et al. 2005) H.X. Qian, W. Zhou, Y.Q. Fu, B.K.A. Ngoi, G.C. Lim, "Crystallographically-dependent ripple formation on Sn surface irradiated with focused ion beam," Appl. Surf. Sci., vol. 240, pp. 140-145, 2005. https://doi.org/10.1016/j.apsusc.2004.06.101

(Qu et al. 2014) L. Qu, H.T. Ma, H.J. Zhao, A. Kunwar, N. Zhao, "In situ study on growth behavior of interfacial bubbled and its effect on interfacial reaction during a soldering process," Appl. Surf. Sci., vol. 305, pp. 133-138, 2014. https://doi.org/10.1016/j.apsusc.2014.03.003

(Ramos de Debiaggi et al. 2012) S. Ramos de Debiaggi, C. Deluque Toro, G. F. Cabeza, and A. Fernandez Guillermet, "Ab initio comparative study of the Cu–In and Cu–Sn

intermetallic phases in Cu–In–Sn alloys," J. Alloy. Compd., vol. 542, pp. 280-292, 2012.

(Regalado et al. 2019) I.L. Regalado, J.J. Williams, S. Joshi, E.M. Dede, Y. Liu, N. Chawla, "X-Ray Microtomography of Thermal Cycling Damage in Sintered Nano-Silver Solder Joints," Adv. Eng. Mater., vol. 21, 2019. https://doi.org/10.1002/adem.201801029

(Ren et al. 2006) F. Ren et al., Appl. Phys. Lett., vol. 89, 141914, 2006.

(Rosenberg & Ohring 1971) R. Rosenberg and M. Ohring, "Void Formation and Growth During Electromigration in Thin Films," J. Appl. Phys., vol. 42, 1971.

(Schneider, Rasband & Eliceiri 2012) C. Schneider, W. Rasband and K. Eliceiri, "NIH Image to ImageJ: 25 years of image analysis," Nature Methods, vol. 9, pp. 671-675, 2012.

(Schwandt 2014) C. S. Schwandt, "Low Energy Microanalysis by EDS or WDS? Comparisons and Concerns from an Analytical Services Laboratory Perspective," Microsc. Microanal., vol. 20, (suppl. 3), 2014.

(Sellers et al. 2010) M.S. Sellers, A.J. Schultz, C. Bararan, D.A. Kofke, "Atomistic modeling of β-sn surface energies and adatom diffusivity," Appl. Surf. Sci., vol. 256, pp. 4402-4407, 2010. https://doi.org/10.1016/j.apsusc.2012.02.038

(Shalaby 2015) R. M. Shalaby, "Indium, chromium and nickel-modified eutectic Sn–0.7 wt% Cu lead-free solder rapidly solidified from molten state," J. Mater. Sci.: Mater. Electron., vol. 26, pp. 6625-6623, 2015.

(Shen & Chen 2017) Y.A. Shen, C. Chen, "Effect of Sn grain orientation on formation of Cu_6Sn_5 intermetallic compounds during electromigration," Scripta Mater., vol. 128, pp. 6-9, 2017. https://doi.org/10.1016/j.scriptamat.2016.09.028

(Shi & Huntington 1987) J. Shi and H. B. Huntington, "Electromigration of Gold and Silver in Single Crystal Tin," J. Phys. Chem. Solids, vol. 48, no. 8, pp. 693-696, 1987.

(Sidhu & Chawla 2008) R. Sidhu and N. Chawla, "Thermal Fatigue Behavior of Sn-Rich (Pb-Free) Solders," Metal. Mater. Trans. A, vol. 39A, 2008.

(Singh & Ohring 1984) P. Singh, M. Ohring, J. Appl. Phys., vol. 56, no. 4, pp. 899-907, 1984.

(Sommadossi & Fernandez Guillermet 2007) S. Sommadossi and A. Fernandez Guillermet, "Interface reaction systematics in the Cu/In-48Sn/Cu system bonded by diffusion soldering," Intermetallics, vol. 15, pp. 912-917, 2007.

(Song et al. 2012) J. M. Song, B. R. Huang, C. Y. Liu, Y. S. Lai, Y. T. Chiu, T. W. Huang, "Nanomechanical responses of intermetallic phase at the solder joint interface – Crystal orientation and metallurgical effects," J. Mater. Sci. Eng., vol. 534, pp. 53-59, 2012. https://doi.org/10.1016/j.msea.2011.11.037

(Subramanian & Lee 2006) K. Subramanian and J. Lee, "Effects of internal stresses on the thermomechanical behavior of Sn-based solder joints," Mater. Sci. Eng. A, vol. 421, pp. 46-56, 2006.

(Subramanian, Sofronis & Ponte Castaneda 2005) S.J. Subramanian, P. Sofronis, P. Ponte Castaneda, "Void growth in power-law creeping solids: Effect of surface diffusion and surface energy," Int. J. Solids. Struct., vol. 42, pp. 6202-6225, 2005. https://doi.org/10.1016/j.ijsolstr.2005.06.048

(Suh, Tu & Tamara 2007) J. O. Suh, K. N. Tu, and N. Tamura, "Dramatic morphological change of scallop-type Cu6Sn5 formed on (001) single crystal copper in reaction between molten SnPb solder and Cu," Appl. Phys. Lett., vol. 91, 2007. https://doi.org/10.1063/1.2761840

(Sun, Suo & Yang 1997) B. Sun, Z. Suo, W. Yang, "A Finite Element Method for Simulating Interface Motion – I. Migration of Phase and Grain Boundaries," Acta Mater., vol. 45, pp. 1907-1915, 1997. 1359-6454/97

(Sundelin, Nurmi & Lepisto 2008) J.J. Sundelin, S.T. Nurmi, T.K. Lepisto, "Recrystallization behaviour of SnAgCu solder joints," J. Mat. Sci. Eng. A, vol. 474, pp. 201-207, 2008. https://doi.org/10.1016/j.msea.2007.04.013

(Tasooji, Lara & Lee 2014) A. Tasooji, L. Lara, K. Lee, "Effect of Grain Boundary Misorientation on Electromigration in Lead-FreeSolder Joint," J. Electron. Mater., vol. 43, 2014. https://doi.org/10.1007/s11664-014-3321-0

(Telang et al. 2002) A. U. Telang, T. R. Bieler, S. Choi, K. N. Subramanian, "Orientation imaging studies of Sn-based electronic solder joints," J. Mater. Res., vol. 17, 2002. https://doi.org/10.1557/JMR.2002.0337

(Telang et al. 2003) A. U. Telang, T. R. Bieler, D. E. Mason, and K. N. Subramanian, "Comparisons of Experimental and Computed Crystal Rotations Caused by Slip in Crept and Thermomechanically Fatigued Dual-Shear Eutectic Sn-Ag Solder Joints," J. Electron. Mater., vol. 32, 2003.

(Telang, Bieler & Crimp 2006) A. Telang, T. Bieler and M. Crimp, "Grain boundary sliding on near-7, 14, 22 degree special boundaries during thermomechanical cycling in surace-mount lead-free solder joint specimens," Mater. Sci. Eng. A, vol. 421, pp. 22-34, 2006.

(Terashima et al. 2009) S. Terashima, T. Kohno, A. Mizusawa, K. Arai, O. Okada, T. Wakabayashi, M. Tanaka and K. Tatusmi, J. Electron. Mater., vol. 38, no. 1, 2009.

(Tian et al. 2011) T. Tian, K. Chen, A.A. MacDowell, D. Parkinson, Y.S. Lai, K.N. Tu, "Quantitative X-ray microtomography study of 3-D void growth induced by electromigration in eutectic SnPb flip-chip solder joints," Scripta Mater., vol. 65, pp. 646-649, 2011. https://doi.org/10.1016/j.scriptamat.2011.07.002

(Tian et al. 2017) S. Tian, S. Li, J. Zhou, F. Xue, R. Cao, and F. Wang, "Effect of indium addition on interfacial IMC growth and bending properties of eutectic Sn–0.7Cu solder joints," J. Mater. Sci.: Mater. Electron., vol. 28, pp. 16120-16132, 2017

(Tian et al. 2018) S. Tian, S. Li, J. Zhou, and F. Xue, "Thermodynamic characteristics, microstructure and mechanical properties of Sn-0.7Cu-xIn lead-free solder alloy," J. Alloy. Compd., vol. 742, pp. 835-843, 2018.

(Tian et al. 2018) Y. Tian, J. Han, L. Ma, F. Guo, "The dominant e ect of c-axis orientation in tin on the electromigration behaviors in tricrystal Sn-3.0Ag-0.5Cu solder joints," Microelectron. Reliab., vol. 80, pp. 7-13, 2018. https://doi.org/10.1016/j.microrel.2017.11.005

(Tu & Turnbull 1970) K. Tu and D. Turnbull, "Direct Observation of Twinning in Tin Lamellae," Acta Metal., vol. 18, pp. 915-929, 1970.

(Tu 2003) K. N. Tu, "Recent advances on electromigration in very-large-scale-integration of interconnects," J. Appl. Phys, vol. 94, no. 5451, 2003.

(Vianco et al. 2007) P. T. Vianco, J. A. Rejent, A. F. Fossum, and M. K. Neilsen, "Compression stress–strain and creep properties of the 52In–48Sn and 97In–3Ag low-temperature Pb-free solders," J. Mater. Sci.: Mater. Electron., vol. 18, pp. 93-119, 2007.

(Wang, Gan & Hsieh 2010) K. K. Wang, D. Gan, K. C. Hsieh, "Orientation relationships, interfaces, and microstructure of η-Cu6Sn5 formed in the early-stage reaction between Cu and molten Sn," Thin Solid Films, vol. 519, 2010. https://doi.org/10.1016/j.tsf.2012.09.045

(Wang, Yao & Keer 2017) W. Wang, Y. Yao, L.M. Keer, "A statistical mechanics model to predict electromigration induced damage and void growth in solder interconnects," Physica A, vol. 468, pp. 195-204, 2017. https://doi.org/10.1016/j.physa.2016.11.016

(Wang, Yuan & Luo 2012) D. L. Wang, Y. Yuan, and L. Luo, "Preparation of Sn–Ag–In Solder Bumps by Electroplating of Sn–Ag and Indium in Sequence and the Effect of Indium Addition on Microstructure and Shear Strength," IEEE Transactions on Components, Packaging, and Manufacturing Technology, vol. 2, no. 8, 2012.

(Wilde 2014) G. Wilde, "Chapter 26: Physical Metallurgy of Nanocrystalline Materials," in Physical Metallurgy, 5th Ed., 2014, pp. 2707-2805.

(Xie et al. 2014) H.X. Xie, D. Friedman, K. Mirpuri, N. Chawla, "Electromigration Damage Characterization in Sn-3.9Ag-0.7Cu and Sn-3.9Ag-0.7Cu-0.5Ce Solder Joints by Three-Dimensional X-ray Tomography and Scanning Electron Microscopy," J. Electron. Mater., vol. 43, 2014. https://doi.org/10.1007/s11664-013-2667-z

(Yamanaka & Ooyoshi 2010) K. Yamanaka, T. Ooyoshi, J. Mater. Sci., vol 21, pp. 53-57, 2010.

(Yang, Chen & Wu 2007) D. Yang, Y.C. Chen, B.Y. Wu, J. Mater. Res., vol. 23, no. 9, pp. 2333-2339, 2007.

(Yeh & Huntington 1984) D. C. Yeh and H. B. Huntington, "Extreme Fast-Diffusion System: Nickel in Single-Crystal Tin," Phys. Rev. Lett., vol. 53, no. 15, 1984.

(Yeh et al. 2002) E.C.C. Yeh, W.J. Choi, K.N. Tu, P. Elenius, H. Balkan, "Current-crowding-induced electromigration failure in flip chip solder joints," Appl. Phys. Lett., vol. 80, no. 580, 2002. https://doi.org/10.1063/1.1432443

(Yeh, Choi & Tu 2002) E.C.C. Yeh, W.J. Choi, K.N. Tu, Appl. Phys. Lett., vol. 80, no. 4, pp. 580-582, 2002.

(Yin et al. 2012) L. Yin, L. Wentlent, L. Yang, B. Arfaei, A. Oasaimeh, P. Borgesen, "Recrystallization and Precipitate Coarsening in Pb-Free Solder Joints During Thermomechanical Fatigue," J. Electron. Mater., vol. 41, pp. 241-252, 2012. https:/doi.org/10.1007/s11664-011-1762-2

(Zhang et al. 2006) L. Zhang, S. Ou, J. Huang, K.N. Tu, S. Gee, L. Nguyen, "Effect of current crowding on void propagation at the interface between intermetallic compound and solder in flip chip solder joints," Appl. Phys. Lett., vol. 88, 012106, 2006. https://doi.org/10.1063/1.2158702

(Zhang et al. 2016) Z. Zhang, H. Cao, M. Li, Y. Yu, H. Yang, S. Yang, "Three-dimensional placement rules of Cu6Sn5 textures formed on the (111) Cu and (001) Cu surfaces using electron backscattered diffraction," J. Mat. Des., vol. 94, pp. 280-285, 2016. http://doi.org/10.1016/j.matdes.2016.01.037

(Zhang, Li, et al 2016) Z.H. Zhang, M.Y. Li, Z.Q. Liu, S.H. Yang, "Growth characteristics and formation mechanisms of Cu6Sn5 phase at the liquid-Sn0.7Cu/(111)Cu and liquid-Sn0.7Cu/(001)Cu joint interfaces," Acta Mater., vol. 104, pp. 1-8, 2016. https://doi.org/10.1016/j.actamat.2015.11.034